ISSN 2149-2123

JOURNAL OF SCIENCE & ENGINEERING

HITTITE

HJSE Official Journal of Hitit University Volume 3, Issue 2, 2017 www.hjse.hitit.edu.tr

Volume 3, Issue 2, 2017

www.hjse.hitit.edu.tr

CONTENT

JOURNAL OF SCIENCE & ENGINEERING
HITTITE

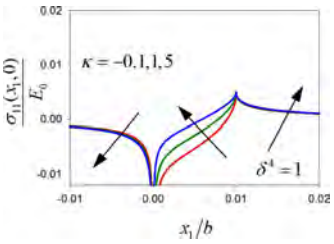

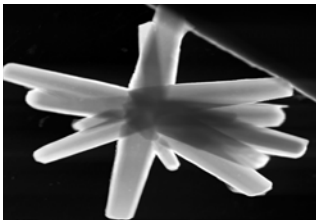

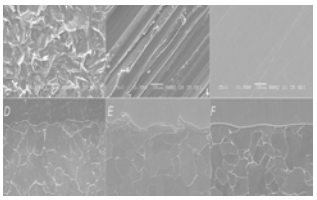

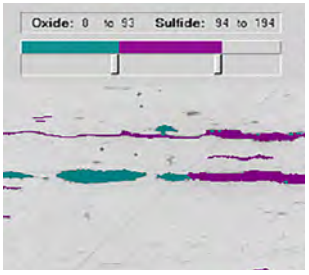

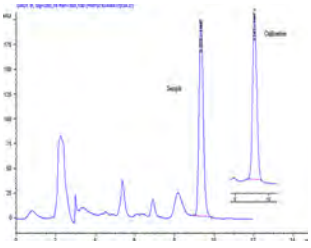

JOURNAL OF SCIENCE & ENGINEERING
HITTITE

CONTENT

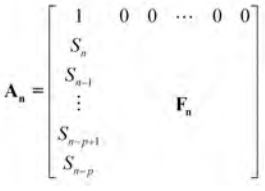

Compounds	RT(min)	Area %
Terpene or terpene related		
Limonene	13.086	0.75
α-Terpinolene	16.138	0.46
(E)- ß-Damascenone	28.979	0.30
Dehydro-ß-ionone	30.219	0.16
Geranyl acetone	31.745	0.40
α-Ionone	33.206	0.49
Aromadendrene	33.349	0.21
6.10.14-Trimethyl-2-pentadecanone	46.433	7.33

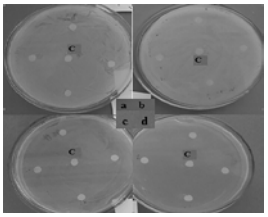

Owner
Prof. Dr. Reha Metin ALKAN
on behalf of Hitit University

Editor-in-chief
Prof. Dr. Ali Kılıçarslan

Associate Editors
Assoc. Prof. Dr. D. Ali Köse
Asst. Prof. Dr. Öncü Akyıldız

Production
Dr. Kazım Köse
Mustafa Güzel

Proofreading
Dr. Aytekin Uzunoğlu

Editor's Office
Tel: +90 364 227 45 33 / 12 36
Fax: +90 364 227 45 35
Email: alikilicarslan@hitit.edu.tr

Subscription Service:
Tel: +90 364 227 45 33 / 12 82
Fax: +90 364 227 45 35
Email: hjse@hitit.edu.tr

EDITORIAL BOARD

Journal Name	: HITTITE JOURNAL OF SCIENCE AND ENGINEERING
Year	: 2016
Managing Editor	: Prof. Dr. Ali KILIÇARSLAN
Managing Office	: Hitit University Faculty of Engineering
Managing Office Tel	: +90 364 227 45 33 / 12 36
Publication Language	: English
Publication Type	: Peer Reviewed, Open Access, International Journal
Delivery Format	: 2 times a year (semi-annually)
Print ISSN	: 2149-2123
Publisher	: Bir Medya
Publisher Address	: Yeniyol Mah. Gazi 12. Sok. No:9/13 ÇORUM
Publisher Tel	: +90 364 225 66 64

I am excited to announce that our Journal has been accepted to be abstracted and indexed in Turkey's most important citation index, TR Dizin Engineering and Basic Sciences Database. I would like to express my gratitude to all our authors and contributing reviewers, without whom we could not succeed.

Almost four years ago, we have begun the efforts to make HJSE. In every stage of making HJSE from the beginning to now an extensive work including the structure, format, scope and legal procedures has been performed by our Editorial Office with devotion. Today, HJSE is an international open access journal which publishes quality peer-reviewed papers twice a year in English.

Meantime, we become an official partner of Publons in order declare we care about Peer Review. Expert peer review helps improve the work of others and protects the world from harmful science that can set back advances in human understanding by decades. Publons is a free service for academics that lets you effortlessly track, verify and showcase your peer review activity across the world's journals. I invite all our reviewers to use Publons.

This new issue of Hittite Journal of Science and Engineering contains eight manuscripts from the disciplines of chemistry, biology, mathematics, food science and technology, materials science and engineering, mechanical engineering. These manuscripts was first screened by Section Editors using plagiarism prevention software and then reviewed and corrected according to the reviewer's comments. I would like to express my gratitude to all our authors and contributing reviewers of this issue.

I would like to thank to the President of Hitit University, Prof. Dr. Reha Metin Alkan, for supporting and motivating HJSE in all respects. I would also like to thank to the Associate Editors of HJSE, namely Assoc. Prof. Dr. Dursun Ali Kose, and Asst. Prof. Dr. Oncu Akyildiz. Special thanks is due to our Production Team, Dr. Kazim Kose and Mustafa Guzel; to our Proofreader Dr. Aytekin Uzunoglu. I also would like to thank to the Editorial Board from national and international universities.

Prof. Dr. Ali Kilicarslan

Editor-in-Chief

Hittite Journal of Science and Engineering, 2016, 3 (1) 61-72
ISSN NUMBER: 2149-2123
DOI: 10.17350/HJSE19030000033

Analytical Solution of the Frictional Contact Problem of a Semi-circular Punch Sliding Over a Homogeneous Orthotropic Half-plane

A. Kucuksucu and M. A. Guler[1]
[1]Department of Mechanical Engineering, TOBB University of Economics and Technology Ankara 06560, Turkey

ABSTRACT

An analytical solution to the frictional sliding contact problem for homogeneous orthotropic materials indented by a semi-circular punch is developed.The principal axes of orthotropy are assumed to be parallel and perpendicular to the contact. Coulomb friction assumption is used to model the friction between the punch and the orthotropic medium. The mixed boundary value problem is reduced into a Fredholm integral equation of the second kind by using Fourier transform technique. The singular integral equation is solved analytically using Jacobi Polynomials for the unknown surface contact stresses. Numerical results show the effect of the orthotropic material parameters, coefficient of friction on the contact stress distribution and load vs. contact length behavior.

Keywords: Contact mechanics; Friction; Orthotropic materials; Singular integral equation; Semi-circular punch.

Article History:
Received: 2016/06/07
Accepted: 2016/11/30
Online:2016/12/31

***Correspondence to**: M. A. Guler, Department of Mechanical Engineering, TOBB University of Economics and Technology Ankara 06560, Turkey.*
Tel: +90 312 292 4088
Fax: +90 312 292 4091
E-Mail: mguler@etu.edu.tr

INTRODUCTION

Contact mechanics problems in isotropic materials gained a great deal of interest and commonly investigated throughout the twentieth century. Orthotropic materials have been utilized both in structural design and engineering applications such as ceramic matrix composites [1]. These materials gained popularity in the last two decades and mainly projected to be used in the aerospace industry as fiber metal laminates in the structure of aircrafts and in the components of gas turbine engines [2]. For example, Tyrannohex is a high strength ceramic material containing properties of other orthotropic materials and it is utilized in the gas turbine components [3].

The studies in the theory of contact mechanics dates back to Lord Kelvin [4] who solved the problem of a force applied at a point in an isotropic infinite medium using Green's functions [5]. Then Lamé [6] further improved Lord Kelvin 's solution with superimposed stresses in a spherical container. Boussinesq [7], provided the solution of a normal force applied to the boundary of an isotropic semi-infinite solid using Green's functions and Kelvin's method. Almost at the same time Hertz [8] solved the problem involving contact between two elastic bodies with curved surfaces and postulated his famous assumptions about contact mechanics. Cerruti [9] inquired on a problem of a force applied tangentially at the plane boundary of a semi-infinite solid also by using Kelvin's solution. In Soutwells' solution, [10] a spherical cavity in an unlimited solid under simple tension was given. Then, Mindlin [11] derived the Green's functions for the half-space by adding a supplementary part of the solution to the Kelvin's infinite space functions.

The literature on contact mechanics, especially with isotropic material assumption has been reviewed by many researchers (see for example Barber and Ciavarella, [12]). Muskhelishvili, England and Johnson [13,14,15] displayed details of the theoretical and numerical methods developed in contact mechanics. Contact problems are mixed boundary value problems due to the boundary conditions given in terms of the displacements and stresses at the same time. The formulation of these problems usually ends up with the singular integral equations (see for example Erdogan [16,17]).

In a contact problem, material selection plays a fundamental role since material properties have crucial effects on the contact stresses. Although, most of the materials contain some local heterogeneity and faults because of their manufacturing techniques, they are usually modeled as isotropic materials. Contact mec-

hanics of anisotropic materials have also been analyzed in the literature. Stroh [18,19] and Lekhnitskii [20] reported solutions using transform methods for a concentrated point force in an infinite body or on the surface of a half-space for anisotropic materials. Sveklo, [21] used integral transformation to the stress equilibrium equations and he also used the Cauchy integral for describing the boundary stress condition to solve contact problem of anisotropic material. Also, Willis [22], proposed a solution method of contact mechanics of anisotropic materials by using Fourier transform. Sveklo' s method for indentation of the orthotropic half-space was analyzed by Shi et al. [23]. Kahya et.al. investigated frictionless contact problem between two orthotropic elastic layers by solving the singular integral equations [24]. Batra and Jiang's provided the parametric analysis of a punch problem for a linear elastic anisotropic layer bonded to a rigid substrate by using Stroh formalism [25]. Bagault et. al. [26] developed a semi-analytical method for the contact problem of anisotropic materials by utilizing Boussinesq and Cerruti solutions. Ashrafi et. al. [27] discussed an analytical and computational solution of the contact problem of a semi-infinite orthotropic material indented by a rigid spherical punch where a numerical analysis was presented using a finite element model. Dong et. al. [28] provided various expressions for the stresses and displacements of orthotropic materials indented by two collinear punches with flat or cylindrical profile. In addition, frictionless contact problems on arbitrarily multilayered piezoelectric half-planes modeled as orthotropic medium and solved using matrix formulation [29,30]. Recently, Zhou and Lee [31] also modeled piezoelectric half space as an orthotropic medium. They conducted a parametric analysis of two-dimensional frictionless sliding contact problem by means of the Galilean transformation [31] and they further studied a frictional contact of anisotropic piezoelectric materials indented by several stamp profiles [32].

Normally, nine independent material parameters are needed to define stress-strain behavior of an orthotropic material. Krenk [33] redefined these parameters so that the number of elastic parameters decrease to four for plane strain and generalized stress conditions. Cinar and Erdogan [34] and Ozturk and Erdogan [35,36] applied this approach to the mixed-mode crack problems in an inhomogeneous orthotropic medium.

Recently, Guler [37] developed a solution method for the sliding frictional contact problem for an orthotropic semi-infinite half space indented by a flat and a circular punch by combining Krenk' s parameters and the method that he used to solve isotropic half space problems indented by various types of punch profiles [38-40]. Then, Kucuksucu et al. [41] postulated wedge-shaped indenter problem of orthotropic materials by using the same method.

The primary aim of the present study is to look into the effect of the material parameters of the contact stress distributions at the surface of the isotropic half plane indented by a rigid semi-circular punch. The problem is reduced to a Fredholm integral equation of the second type which is solved using of Jacobi Polynomials. Relationships between the applied load versus the contact length and stress intensity factors at the sharp end of the punch are also found.

Formulation of the problem

Consider the contact problem described in Fig. 1 where a rigid semi-circular punch is under sliding contact with a semi-infinite homogeneous orthotropic medium. The sliding contact is defined between $x_1 = 0$ to $x_1 = b$ at the surface of the orthotropic medium ($x_2 = 0$) where (x_1, x_2), are the principal axes of orthotropy which are parallel and perpendicular to the boundary [42,43]. It is assumed that the coefficient of static friction is constant within the contact area. P and Q are the resultant normal and shear forces, respectively, and they are proportional $Q = \eta P$, according to the Coulomb's law.

In usual notation, u_i and σ_{ij} $(i, j = 1,2)$ specify the displacement and stress components, and E_{ii}, G_{ij} and ν_{ij} $(i, j = 1,2,3)$ specify engineering elastic parameters. Orthotropic constitutive equations are composed of 9 elastic constants (3 Young's moduli, E_{11}, E_{22}, E_{33}, 3 shear moduli, G_{12}, G_{13}, G_{23} and 3 Poison's ratios, $\nu_{12}, \nu_{13}, \nu_{23}$). To simplify the solution, engineering parameters are replaced by four independent material parameters, namely effective stiffness parameter E, the effective Poisson' s ratio ν, the shear parameter κ, and stiffness ratio δ, defined by [33].

$$E = \sqrt{E_{11}E_{22}}, \quad \nu = \sqrt{\nu_{12}\nu_{21}}, \quad \delta^4 = \frac{E_{11}}{E_{22}} = \frac{\nu_{12}}{\nu_{21}}, \quad \kappa = \frac{E}{2G_{12}} - \nu, \tag{1a-d}$$

for generalized plane stress conditions and

$$E = \sqrt{\frac{E_{11}E_{22}}{(1-\nu_{13}\nu_{31})(1-\nu_{23}\nu_{32})}}, \quad \nu = \sqrt{\frac{(\nu_{12}+\nu_{13}\nu_{32})(\nu_{21}+\nu_{23}\nu_{31})}{(1-\nu_{13}\nu_{31})(1-\nu_{23}\nu_{32})}}, \tag{2a,b}$$

$$\delta^4 = \frac{E_{11}}{E_{22}}\frac{1-\nu_{23}\nu_{32}}{1-\nu_{13}\nu_{31}}, \quad \kappa = \frac{E}{2G_{12}} - \nu, \tag{2c,d}$$

for plane strain conditions. In addition, we scale the independent and dependent variables by using stiffness or scaling ratio as

$$x=\frac{x_1}{\sqrt{\delta}},\quad y=x_2\sqrt{\delta},\quad u(x,y)=\sqrt{\delta}u_1(x_1,x_2),\quad v(x,y)=\frac{1}{\sqrt{\delta}}u_2(x_1,x_2),$$

(3a-d)

$$\sigma_{xx}(x,y)=\sigma_{11}(x_1,x_2)/\delta,\quad \sigma_{yy}(x,y)=\delta\sigma_{22}(x_1,x_2),\quad \sigma_{xy}(x,y)=\sigma_{12}(x_1,x_2).$$

(3e-g)

In this study, the spatial variation of Poisson's ratio is assumed to be negligible, so it is taken as constant [40]. Note that the special case of $\delta=\kappa=1$ corresponds to an isotropic material. Also, in a homogeneous orthotropic medium the range of κ can be defined as $-1<\kappa<\infty$ and it can be shown that for $\kappa\le -1$the elasticity problem has no applicable solution [35,36,44].

Integral equation of the problem

The singular integral equation of the sliding contact problem can be written as [37,43],

$$-\omega_1\sigma_{xy}(x,0)+\frac{1}{\pi}\int_0^{b/\sqrt{\delta}}\frac{\sigma_{yy}(t,0)}{t-x}dt=\lambda_1E_0f(x),\qquad 0<x<\frac{b}{\sqrt{\delta}},$$

(4a)

$$\omega_2\sigma_{yy}(x,0)+\frac{1}{\pi}\int_0^{b/\sqrt{\delta}}\frac{\sigma_{xy}(t,0)}{t-x}dt=\lambda_2E_0g(x),\qquad 0<x<\frac{b}{\sqrt{\delta}},$$

(4b)

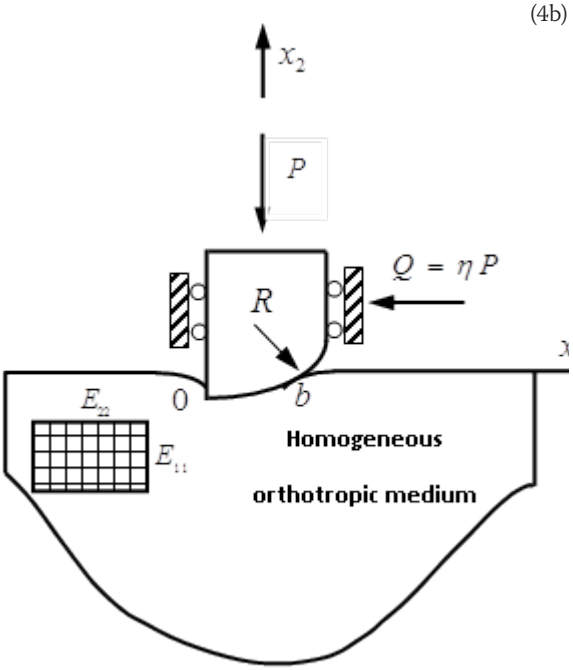

Figure 1. Geometry of sliding frictional contact problem of orthotropic medium indented by the semi-circular punch.

where

$$f(x)=\frac{\partial}{\partial x}v(x,0),\qquad g(x)=\frac{\partial}{\partial x}u(x,0)$$

(5a,b)

$$\lambda_1=\frac{\Delta_0}{(1-\nu^2)(r_2r_4r_7-r_1r_3r_8)},\qquad \omega_1=\frac{2(\kappa+\nu)(r_1r_3r_6-r_2r_4r_5)}{(1-\nu^2)(r_2r_4r_7-r_1r_3r_8)},\qquad (6a,b)$$

$$\lambda_2=\frac{\Delta_0}{2(\kappa+\nu)(r_5-r_6)},\qquad \omega_2=\frac{(1-\nu^2)}{2(\kappa+\nu)}\frac{(r_8-r_7)}{(r_5-r_6)}.\qquad (7a,b)$$

In the physical domain (x_1,x_2), the integral equation (4) becomes

$$-\omega_1\tau(x_1)+\frac{\delta}{\pi}\int_0^b\frac{\sigma(t_1)}{t_1-x_1}dt_1=\lambda_1E_0f(x_1),\qquad 0<x_1<b,\qquad (8a)$$

$$\omega_2\delta\sigma(x_1)+\frac{1}{\pi}\int_0^b\frac{\tau(t_1)}{t_1-x_1}dt_1=\lambda_2E_0g(x_1),\qquad 0<x_1<b,\qquad (8b)$$

where

$$f(x_1)=\frac{\partial}{\partial x_1}u_2(x_1,0),\qquad g(x_1)=\delta\frac{\partial}{\partial x_1}u_1(x_1,0).\qquad (9a,b)$$

Eq. (8) constitute a pair of integral equations in terms of the unknown contact stresses σ and τ. In the contact region, we have

$$\sigma_{22}(x_1,0)=\sigma(x_1)=-p(x_1),\qquad 0<x_1<b,\qquad (10a)$$

$$\sigma_{12}(x_1,0)=\tau(x_1)=-\eta\,p(x_1),\qquad 0<x_1<b,\qquad (10b)$$

where the contact pressure, $p(x_1)$, $0<x_1<b$, is only unknown quantity. The relation between the applied load and the contact length, b can be found by applying equilibrium condition [46]. Thus, using Eq. (10), Eq. (8) become:

$$\omega_1\eta\,p(x_1)-\frac{\delta}{\pi}\int_0^b\frac{p(t_1)}{t_1-x_1}dt_1=\lambda_1E_0f(x_1),\qquad 0<x_1<b,\qquad (11a)$$

$$-\omega_2\delta\,p(x_1)-\frac{\eta}{\pi}\int_0^b\frac{p(t_1)}{t_1-x_1}dt_1=\lambda_2E_0g(x_1),\qquad 0<x_1<b.\qquad (11b)$$

and contact pressure must satisfy the following equilibrium equation:

$$\int_0^b p(t_1)dt_1=P,$$

(12)

where P is the resultant compressive force. The amplitude of the applied load may be given in terms of either the load P or stamp displacement in the x_2 axis.

In order to solve the integral equation, the limits of integration must be normalized. Now setting:

$$x_1 = x_1^* R, \qquad t_1 = t_1^* R, \qquad b = b^* R, \qquad p(t_1) = p^*(t_1^*), \qquad 0 < x_1^*, t_1^* < b^*. \tag{13}$$

The integral equation (11a) and the equilibrium equation (12) can be written as:

$$Ap^*\left(x_1^*\right) + \frac{B}{\pi}\int_0^{b^*} \frac{p^*(t_1^*)}{t_1^* - x_1^*} dt_1^* = \lambda_1 E_0 x_1^* \tag{14}$$

$$\int_0^{b^*} p^*(t_1^*) dt_1^* = \frac{P}{R} \tag{15}$$

where

$$A = \omega_1 \eta, \qquad B = -\delta. \tag{16a-b}$$

The integration limit is normalized from $(0, b^*)$ to $(-1,1)$ by the following change of variables:

$$t_1^* = \frac{b^*}{2}(s+1), \qquad x_1^* = \frac{b^*}{2}(r+1), \qquad p^*\left(t_1^*\right) = \lambda_1 E_0 \frac{b^*}{2}\phi(s), \qquad -1 < r, s < 1. \tag{17a-c}$$

Since the stamp profile is given as $u_2(x_1, 0) = -v_0 + \frac{x_1^2}{2R}$, the function, $f\left(x_1\right)$ becomes

$$f(x_1) = \frac{\partial}{\partial x_1} u_2(x_1, 0) = \frac{x_1}{R}. \tag{18}$$

The integral equation (14) can then be expressed in a normalized form by using Eqs. (17) as

$$A\phi(r) + \frac{B}{\pi}\int_{-1}^{1} \frac{\phi(s)}{s-r} ds = r + 1. \tag{19}$$

On the solution of integral equations

For an accurate and efficient solution of the integral equation the corresponding weight function $w(s)$ needs to be determined. By defining the complex potential [13,45,46]:

$$\Phi(z) = \frac{1}{2\pi i}\int_{-1}^{1} \frac{\phi(s)}{s-z} ds. \tag{20}$$

From Muskhelishvili [13] and by using the complex function theory, the dominant part of the integral equation can be written as

$$A\phi(r) + \frac{B}{\pi}\int_{-1}^{1} \frac{\phi(s)}{s-r} ds = r + 1. \tag{21}$$

The index of the integral equation for the semi-circular punch is defined by:

$$\chi = -(\alpha + \beta) = -(N_0 + M_0) = 0, \tag{22}$$

where $N_0, M_0 = -1, 0, 1$ are arbitrary integers and can be determined from the physics of the problem. Since the semi circular stamp has a sharp corner at $x_1 = 0$ and a smooth contact at $x_1 = b$, from the physics of the problem, we must require that α be positive and β be negative. α and β is found to be

$$\begin{aligned} &\omega_1\eta > 0: \quad \alpha = \frac{\theta}{\pi}, \quad \beta = -\frac{\theta}{\pi}, \\ &\omega_1\eta = 0: \quad \alpha = 0.5, \quad \beta = -0.5, \\ &\omega_1\eta < 0: \quad \alpha = 1 - \frac{\theta}{\pi}, \quad \beta = \frac{\theta}{\pi} - 1, \end{aligned} \tag{23a-d}$$

$$\theta = \arctan\left|\frac{\delta}{\omega_1\eta}\right| > 0, \qquad 0 < \theta < \frac{\pi}{2}.$$

Now, one can assume a solution in terms of Jacobi Polynomials as:

$$\phi(s) = \sum_{n=0}^{\infty} c_n w(s) P_n^{(\alpha,\beta)}(s), \quad w(s) = (1-s)^{\alpha}(1+s)^{\beta}, \qquad -1 < s < 1, \tag{24}$$

where c_n, $(n = 0, 1, \ldots)$ are undetermined constants and $P_n^{(\alpha,\beta)}(s)$ are Jacobi polynomials. Substituting Eq. (24) into Eq. (21) results in

$$\sum_0^{\infty} c_n \left[Aw(r) P_n^{(\alpha,\beta)}(r) + \frac{B}{\pi}\int_{-1}^{1} \frac{w(s) P_n^{(\alpha,\beta)}(s) ds}{s-r} \right] = r + 1. \tag{25}$$

Using the following property of Jacobi polynomials:

$$AP_n^{(\alpha,\beta)}(r)w(r)+\frac{B}{\pi}\int_{-1}^{1}\frac{P_n^{(\alpha,\beta)}(s)w(s)}{s-r}ds=-2^{-\chi}\frac{B}{\sin\pi\alpha}P_{n-\chi}^{(-\alpha,-\beta)}(r),$$
$$-1<r<1,\qquad \Re(\alpha)>1,\qquad \Re(\beta)>1,\qquad \Re(\alpha)\neq(0,1,\ldots,) \tag{26}$$

Eq. (25) can be expressed as

$$\sum_0^n c_n\left[\frac{\delta}{\sin\pi\alpha}P_n^{(-\alpha,-\beta)}(r)\right]=r+1,\qquad -1<r<1. \tag{27}$$

In this problem, after the application of a given load, one end of the contact length (i.e., b^*) is unknown. However, for a given value of the contact length (b^*) Eq. (27) gives $n+1$ equations for $n+1$ the unknowns. Expanding right hand side of Eq. (27) into a series of Jacobi polynomials $P_n^{(-\alpha,-\beta)}$ and observing that, we find:

$$r+1=P_1^{(-\alpha,-\beta)}(r)+(1+\alpha)P_0^{(-\alpha,-\beta)}(r) \tag{28}$$

where

$$P_1^{(-\alpha,-\beta)}(r)=-\alpha+r,\qquad P_0^{(-\alpha,-\beta)}(r)=1 \tag{29a,b}$$

Therefore Eq. (27) can be written as:

$$\frac{\delta}{\sin\pi\alpha}\sum_0^n c_nP_n^{(-\alpha,-\beta)}(r)=P_1^{(-\alpha,-\beta)}(r)+(1+\alpha)P_0^{(-\alpha,-\beta)}(r), \tag{30}$$

Comparing right hand side and left hand side of Eq. (30), we have only two non-zero coefficients:

$$c_0=\frac{(1+\alpha)\sin\pi\alpha}{\delta},\qquad c_1=\frac{\sin\pi\alpha}{\delta}. \tag{31a,b}$$

Therefore, the solution becomes;

$$\phi(s)=w(s)\sum_{n=0}^{1}c_nP_n^{(\alpha,\beta)}(s)=w(s)\left[c_0+c_1(\alpha+s)\right],$$
$$=w(s)\frac{\sin\pi\alpha}{\delta}\left[1+2\alpha+s\right]. \tag{32}$$

Using Eq. (15) the equilibrium equation (17c) may be expressed as:

$$\int_{-1}^{1}\phi(s)ds=\frac{4}{\lambda_1E_0b^{*2}}\frac{P}{R}. \tag{33}$$

Orthogonality condition of Jacobi Polynomials can be written as:

$$\int_{-1}^{1}P_n^{(\alpha,\beta)}(t)P_j^{(\alpha,\beta)}(t)w(t)dt=\begin{cases}0 & n\neq j\\ \theta_j^{(\alpha,\beta)} & n=j\end{cases}\qquad j=0,1,2,\ldots \tag{34}$$

where

$$\theta_0^{(\alpha,\beta)}=\int_{-1}^{1}w(t)dt=\frac{2^{\alpha+\beta+1}\Gamma(\alpha+1)\Gamma(\beta+1)}{\Gamma(\alpha+\beta+2)}, \tag{35}$$

$$\theta_j^{(\alpha,\beta)}=\frac{2^{\alpha+\beta+1}\Gamma(j+\alpha+1)\Gamma(j+\beta+1)}{(2j+\alpha+\beta+1)j!\Gamma(j+\alpha+\beta+1)},\quad j=1,2,\ldots \tag{36}$$

Using the orthogonality condition of the Jacobi Polynomials, the relation between applied load P and the contact length b can be found from Eq. (33) as:

$$c_0\theta_0=\frac{4}{\lambda_1E_0b^{*2}}\frac{P}{R}. \tag{37}$$

θ_0 can be given as:

$$\theta_0^{(\alpha,\beta)}=\frac{2\pi\alpha}{\sin\pi\alpha}. \tag{38}$$

The load versus contact length relation may be obtained by substituting c_0 from Eq. (31a) and θ_0 from Eq. (38) into Eq. (37)

$$P^*=\frac{P}{E_0R}=\frac{(1+\alpha)\pi\alpha\lambda_1}{2\delta}b^{*2}. \tag{39}$$

Then the contact pressure distribution $p^*(t_1^*)$ becomes:

$$p^*(t_1^*)=\lambda_1E_0\frac{b^*}{2}\phi(t_1^*),$$
$$=\lambda_1E_0\frac{b^*}{2}\left(\frac{b^*-t_1^*}{t_1^*}\right)^{\alpha}\sum_{n=0}^{1}c_nP_n^{(\alpha,\beta)}\left(\frac{2t_1^*}{b^*}-1\right),$$
$$=\lambda_1E_0b^*\left(\frac{b^*-t_1^*}{t_1^*}\right)^{\alpha}\frac{\sin\pi\alpha}{\delta}\left[\alpha+\frac{t_1^*}{b^*}\right]. \tag{40}$$

Using Eq. (10) and Eq. (13) the non-dimensional pressure distribution pressure becomes:

$$\frac{\sigma_{22}(x_1^*,0)}{E_0} = -\lambda_1 b^* \left(\frac{b^* - x_1^*}{x_1^*}\right)^{\alpha} \frac{\sin\pi\alpha}{\delta}\left[\alpha + \frac{x_1^*}{b^*}\right]. \quad (41)$$

The stress component $\sigma_{11}(x_1^*,0)$ can be found by using

$$\sigma_{11}\left(x_1^*,0\right) = \begin{cases} C\sigma_{22}\left(x_1^*,0\right) + \dfrac{D}{\pi}\displaystyle\int_0^{b^*} \frac{\sigma_{22}\left(t_1^*,0\right)}{t_1^* - x_1^*} dt_1^*, & 0 < x_1^* < b^*, \\ \dfrac{D}{\pi}\displaystyle\int_0^{b^*} \frac{\sigma_{22}\left(t_1^*,0\right)}{t_1^* - x_1^*} dt_1^*, & x_1^* \notin \left[0, b^*\right], \end{cases}$$

(42)

where

$$C = \left(\frac{\omega_2}{\lambda_2} + \nu\right)\delta^2, \quad D = \frac{\eta\delta}{\lambda_2}. \quad (43)$$

Therefore

$$\sigma_{11}(x_1^*,0) = -q\left(x_1^*\right) = -\lambda_1 E_0 \frac{b^*}{2}\psi\left(x_1^*\right) \quad (44)$$

$$\psi(r,0) = \begin{cases} Cw(r)c_0 P_0^{(\alpha,\beta)}(r) + Cw(r)c_1 P_1^{(\alpha,\beta)}(r) \\ \quad + \dfrac{D}{\pi}\{c_0 L_0 + c_1 L_1\}, & -1 < r < 1, \\ \dfrac{D}{\pi}\{c_0 L_0 + c_1 L_1\}, & |r| > 1. \end{cases}$$

(45)

where

$$L_0(r) = \int_{-1}^{1} \frac{w(r)}{s-r} dr = \frac{\pi}{\sin\pi\alpha} \begin{cases} (-r+1)^{\alpha}(-r-1)^{\beta} - 1, & -\infty < r < -1, \\ (1-r)^{\alpha}(1+r)^{\beta}\cos\pi\alpha - 1, & -1 < r < 1, \\ (r-1)^{\alpha}(r+1)^{\beta} - 1, & 1 < r < \infty, \end{cases}$$

(46)

$$L_1(r) = P_1^{(\alpha,\beta)}(r)L_0(r) + \frac{2\pi\alpha}{\sin\pi\alpha}. \quad (47)$$

Mode I stress intensity factors at the ends of the stamp for a homogeneous medium can be defined as:

$$\begin{aligned} k_p(0) &= \lim_{x_1\to 0} x_1^{\alpha} p(x_1) \\ &= \lambda_1 E_0 b^* b^{\alpha} \sum_{n=0}^{1} c_n P_n^{(\alpha,\beta)}(-1) \\ &= \lambda_1 E_0 b^* b^{\alpha} \alpha \frac{\sin\pi\alpha}{\delta} \end{aligned} \quad (48a)$$

Defining the non-dimensional stress intensity factors as

$$\begin{aligned} k_p^*(0) &= \frac{k_p(0)}{E_0 b^{\alpha}} \\ &= \lambda_1 b^* \sum_{n=0}^{1} c_n P_n^{(\alpha,\beta)}(-1) \\ &= \lambda_1 b^* \alpha \frac{\sin\pi\alpha}{\delta} \end{aligned} \quad (48b)$$

Stress intensity factor in terms of the in-plane stress component can be defined as

$$\begin{aligned} k_q(0^+) &= \lim_{x_1\to 0^+} x_1^{\alpha} q(x_1) \\ &= \lambda_1 E_0 b^* b^{\alpha} \alpha \left\{ C\frac{\sin\pi\alpha}{\delta} + D\frac{\cos\pi\alpha}{\delta} \right\} \end{aligned} \quad (49a)$$

In non-dimensional form Eq. (49a) can be expressed as

$$\begin{aligned} k_q^*(0^+) &= \frac{k_q(0^+)}{E b^{\alpha}} \\ &= \lambda_1 b^* \alpha \left\{ C\frac{\sin\pi\alpha}{\delta} + D\frac{\cos\pi\alpha}{\delta} \right\} \end{aligned} \quad (49b)$$

$$\begin{aligned} k_q(0^-) &= \lim_{x_1\to 0^-} \left(-x_1\right)^{\alpha} q(x_1) \\ &= E_0 b^* \left(b\right)^{\alpha} \frac{\lambda_1\eta}{\lambda_2}\alpha \end{aligned} \quad (50a)$$

Similarly, in non-dimensional form Eq. (50a) can be expressed as:

$$\begin{aligned} k_q^*(0^-) &= \frac{k_q(0^-)}{\left(b\right)^{\alpha} E_0} \\ &= \frac{\lambda_1\eta}{\lambda_2} b^* \alpha \end{aligned} \quad (50b)$$

RESULTS AND DISCUSSION

Contact problem described in Fig. 1 is solved analytically to obtain results for the contact stresses and in-plane

stress distributions beneath semi-circular punch profile under various restrictions. In the results, the contact stresses are normalized by E_0. Results are given for the following range of parameters ($-0.1 \le \kappa \le 5$, $0.2 \le \delta^4 \le 5$, $\nu = 3/7$ and $0 \le \eta \le 0.9$). There are certain limitations on the material parameters of orthotropic materials. These restrictions require that $\kappa + \nu > 0$, (see Eq.(1) and (2), $0 < \nu < 1$ and $\kappa > -1$.

Fig. 2-4 illustrate the contact pressure, $\sigma_{22}(x_1,0)$ under semi-circular punch. Note that the contact pressure is bounded and zero at the smooth end of semi-circular punch $(x_1 = b)$. However, at the leading or another words sharp end, the contact stress is singular. In-plane stresses, $\sigma_{11}(x_1,0)$ are bounded and discontinuous at the leading edge $(x_1 = 0)$. In the distribution of $\sigma_{11}(x_1,0)$ as $(x_1 \to b)$ near leading edge needle-like spikes distribution is observed.

This case, obviously results in crack nucleation and as a result component total service life may be reduced because of contact fracture [47]. It is interesting that neither the stiffness ratio, δ, nor the shear parameter, κ, has effect on the distribution of in-plane stress, $\sigma_{11}(x_1,0)$, at the leading edge $(x_1 \to b)$ because of the formulation as

$$\frac{\sigma_{11}(b,0)}{E_0} = -\lambda_1 \frac{b^*}{2} \psi(1) = b^* \eta \tag{51}$$

Fig. 6a shows the dependence of various material parameters δ and the κ on the powers of stress singularities, α and β for fixed value of the coefficient of friction,

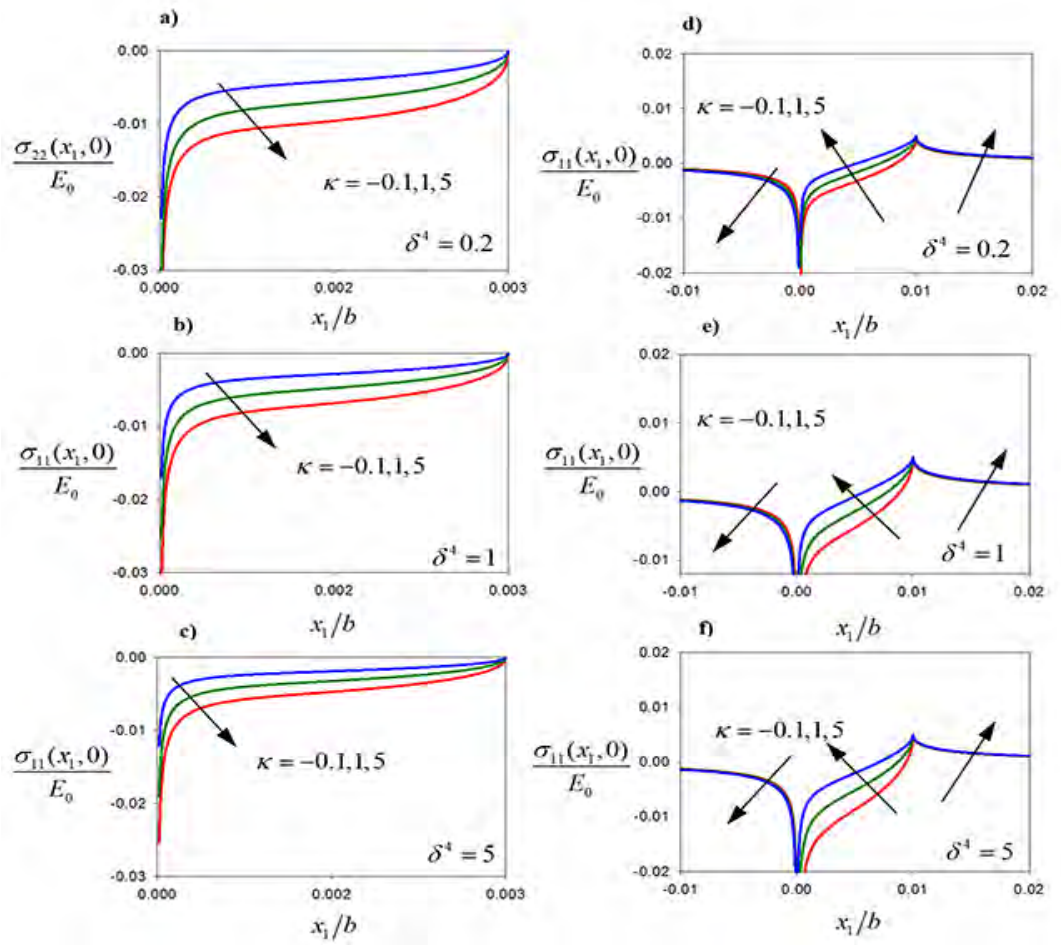

Figure 2. Contact pressure, $\sigma_{22}(x_1,0)$, and in-plane stress, $\sigma_{11}(x_1,0)$ distributions at the contact surface under semi-circular punch for various values of the parameters $\kappa = \frac{E}{2G_{12}} - \nu$ with $\eta = 0.5$, $\nu = 3/7$, $b/R = 0.01$, $\delta^4 = \frac{E_{11}}{E_{22}} = \frac{\nu_{12}}{\nu_{21}}$ where E and ν are given in equations (1) and (2) a) $\sigma_{22}(x_1,0)$ for $\delta^4 = 0.2$; b) $\sigma_{22}(x_1,0)$ for $\delta^4 = 1$; c) $\sigma_{22}(x_1,0)$ for $\delta^4 = 5$; d) $\sigma_{11}(x_1,0)$ for $\delta^4 = 0.2$; e) $\sigma_{11}(x_1,0)$ for $\delta^4 = 1$; f) $\sigma_{11}(x_1,0)$ for $\delta^4 = 5$.

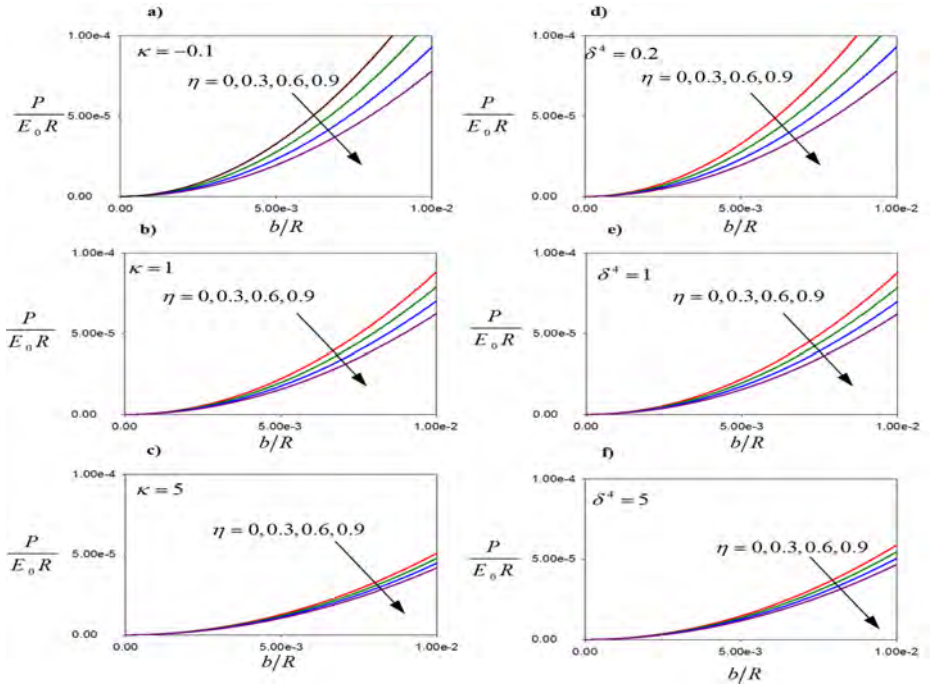

Figure 3. Contact pressure, $\sigma_{22}(x_1,0)$, and in-plane stress, $\sigma_{11}(x_1,0)$ distributions at the contact surface under semi-circular punch for various values of the parameters $\kappa=\frac{E}{2G_{12}}-\nu$ with $\eta=0.5$, $\nu=3/7$, $b/R=0.01$, $\delta^4=\frac{E_{11}}{E_{22}}=\frac{\nu_{12}}{\nu_{21}}$ where E and ν are given in equations (1) and (2) a) $\sigma_{22}(x_1,0)$ for $\kappa=-0.1$; b) $\sigma_{22}(x_1,0)$ for $\kappa=1$; c) $\sigma_{22}(x_1,0)$ for $\kappa=5$; d) $\sigma_{11}(x_1,0)$ for $\kappa=-0.1$; e) $\sigma_{11}(x_1,0)$ for $\kappa=1$; f) $\sigma_{11}(x_1,0)$ for $\kappa=5$.

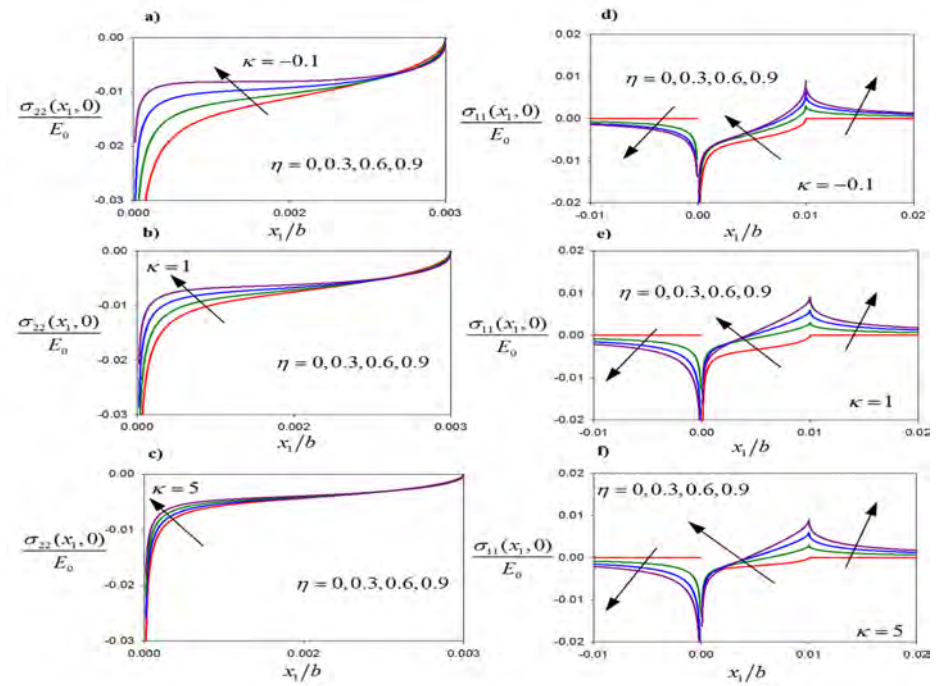

Figure 4. Contact pressure, $\sigma_{22}(x_1,0)$ and in-plane stress $\sigma_{11}(x_1,0)$ distributions at the contact surface under semi-circular punch for various values of the friction coefficients parameters η, with $\kappa=\frac{E}{2G_{12}}-\nu$, $\nu=3/7$, $b/R=0.01$, $\delta^4=\frac{E_{11}}{E_{22}}=\frac{\nu_{12}}{\nu_{21}}=0.2$ where E and ν are given equations (1) and (2) a) $\sigma_{22}(x_1,0)$ for $\kappa=-0.;\kappa=1$; c) $\sigma_{22}(x_1,0)$ for $\kappa=5$; d) $\sigma_{11}(x_1,0)$ for $\kappa=-0.1$; e) $\sigma_{11}(x_1,0)$ for $\kappa=1$; f) $\sigma_{11}(x_1,0)$ for $\kappa=5$.

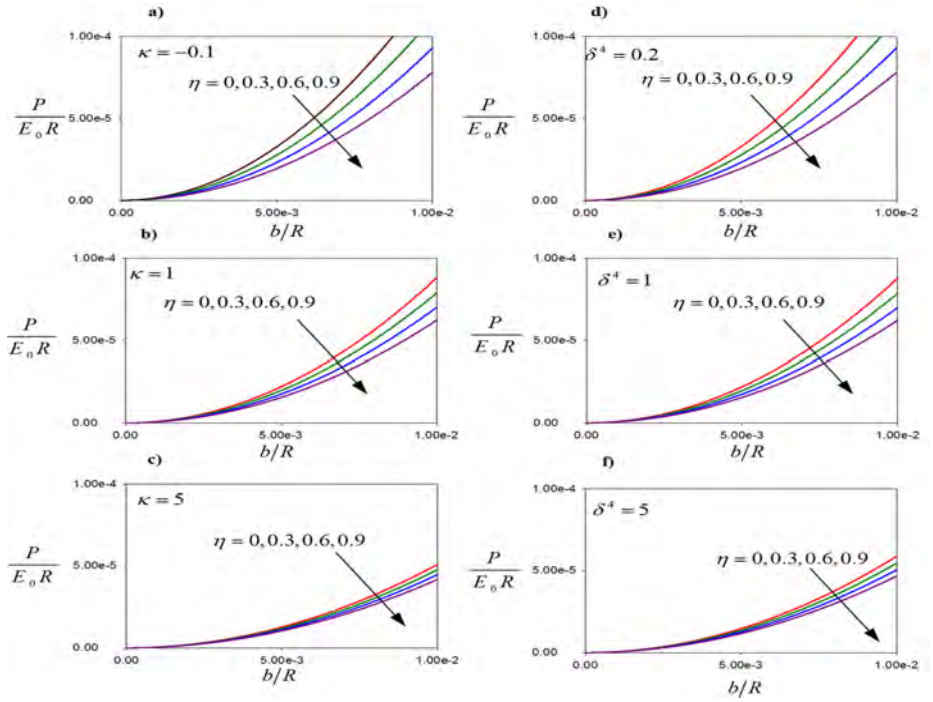

Figure 5. The load, $\frac{P}{E_0R}$ and the contact length b, an orthotropic homogeneous medium under semi-circular punch for various values of the friction coefficients η, with $\kappa=\frac{E}{2G_{12}}-\nu$, $\nu=3/7$, $b/R=0.01$, $\delta^4=\frac{E_{11}}{E_{22}}=\frac{\nu_{12}}{\nu_{21}}$ where E and ν are given equations (1) and (2) a) $\kappa=-0.1$, $\delta^4=0.2$;b) $\kappa=1$, $\delta^4=0.2$ c) $\kappa=5$, $\delta^4=0.2$; $\kappa=-0.1$;f) $\delta^4=5$, $\kappa=-0.1$.

$\eta=0.5$, and effective Poisson's ratio, $\nu=3/7$. As the shear parameter, κ, increases, $|\alpha|$ increases for fixed values of the stiffness ratio parameter, δ. Note that, for $\kappa>3$ the change of the δ has no effect on the curves. Fig. 6b depicts the dependence of κ and δ on the powers of stress singularities, α and β for fixed value of the coefficient of friction, $\eta=0.5$, and effective Poisson's ratio, $\nu=3/7$. As the stiffness ratio parameter, δ, increases, $|\alpha|$ increases for fixed values of the shear parameter, κ. Note that, for $\delta>3$ the curves do not sensitive to the change of the κ.

Table 1 shows some examples of the stress intensity factors obtained for a semi-circular stamp. The values of stress intensity factors increase both shear parameter and stiffness ratio decreases.

Table 1.The normalized stress intensity factors for a homogeneous orthotropic medium under contact stresses for the semi-circular punch, $\nu=3/7$.

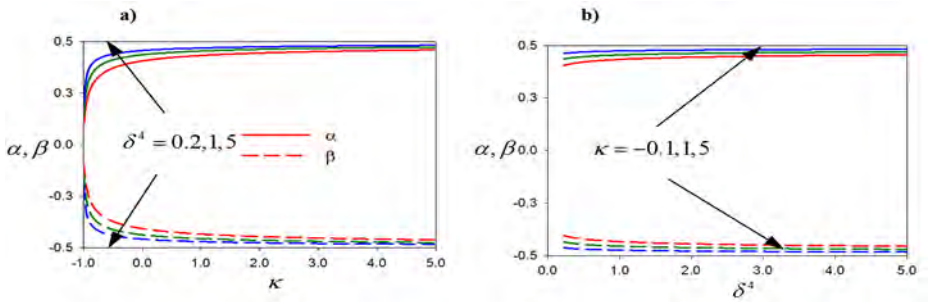

Figure 6. Strength of stress singularity at $x_1=b$, α and $x_1=0$, β with $\eta=0.5$, , $\nu=3/7$ for various values of a) , $\delta^4=\frac{E_{11}}{E_{22}}=\frac{\nu_{12}}{\nu_{21}}$ b) $\kappa=\frac{E}{2G_{12}}-\nu$ where E and ν are given in equations (2) and (3) for semi-circular punch where $\chi=-(\alpha+\beta)=0$.

Table 1. The normalized stress intensity factors for a homogeneous orthotropic medium under contact stresses for the semi-circular punch, $\nu = 3/7$ ..

Stiffness ratio	$\eta = 0.5$			$\eta = 0.9$		
	$\kappa = -0.1$	$\kappa = 1$	$\kappa = 5$	$\kappa = -0.1$	$\kappa = 1$	$\kappa = 5$
$\delta^4 = 0.2$	0.00426	0.00316	0.00197	0.003232	0.00267	0.00181
$\delta^4 = 1$	0.00315	0.00225	0.00136	0.002668	0.00203	0.00129
$\delta^4 = 5$	0.00224	0.00156	0.00092	0.002028	0.00146	0.00090

Stiffness ratio	$\eta = 0.5$			$\eta = 0.9$		
	$\kappa = -0.1$	$\kappa = 1$	$\kappa = 5$	$\kappa = -0.1$	$\kappa = 1$	$\kappa = 5$
$\delta^4 = 0.2$	0.00251	0.00186	0.00116	0.002941	0.002433	0.001650
$\delta^4 = 1$	0.00360	0.00257	0.00155	0.003904	0.002974	0.001892
$\delta^4 = 5$	0.00534	0.00371	0.00221	0.005474	0.003964	0.002429

Stiffness ratio	$\eta = 0.5$			$\eta = 0.9$		
	$\kappa = -0.1$	$\kappa = 1$	$\kappa = 5$	$\kappa = -0.1$	$\kappa = 1$	$\kappa = 5$
$\delta^4 = 0.2$	0.002009	0.00216	0.00230	0.00300	0.00344	0.00387
$\delta^4 = 1$	0.002166	0.00227	0.00236	0.00345	0.00377	0.00407
$\delta^4 = 5$	0.002274	0.00234	0.00241	0.00378	0.00401	0.00421

CONCLUSION

In this paper, an analytical solution to the plane contact problem is given on orthotropic homogeneous medium is intended by a sliding rigid semi-circular stamp. The given problem is reduced to a second kind singular integral equation, which is solved using of Jacobi Polynomials. The effect of orthotropic material parameters and friction coefficient on the contact stress are presented. The following conclusions can be drawn from the results found in this study:

- In sliding contact problems orthotropic homogeneous materials the weight functions $w(x)$ describing the asymptotic behavior of the contact stresses are dependent, as in the isotropic homogeneous materials, on the coefficient of friction η and the surface value of the Poisson's ratio ν (or the shear parameter κ) only, and are independent of all other material constants and length parameters.
- In-plane stress tensile spike occurs on the surface at the trailing end of the contact region. The magnitude of the tensile spike increases with the increasing coefficient of friction, η stiffness ratio, δ and shear parameter κ.
- In all cases the resultant force P increases with increasing contact area in a parabolic manner.
- The shear parameter κ, and the stiffness ratio δ. do not affect the length of the contact zone.
- The Poisson ratio ν has only negligible influence on the $\sigma_{22}(x_1,0)$ contact pressure distribution for $\kappa \le -0.1$
- Results have relevance to surface crack initiation and propagation in load transfer components.

ACKNOWLEDGEMENT

The main idea of the paper stemmed from the work by author (A.K.) at TOBB University of Economics and Technology during her postgraduate research fellowship from the Scientific and Technological Research Council of Turkey (TUBITAK) through the program BIDEB – 2218 between the years 2012 and 2014.

REFERENCES

1. Baroumes L, Bouillon E, Christin F. An improved long life duration ceramic matrix composite material for jet aircraft engine applications. 24th International Congress of the Aeronautical Sciences (2004).
2. Esfandiar H, Daneshmand S, Mondali M. Analysis of elastic–plastic behavior of fiber metal laminates subjected to in–plane tensile loading. Int. J. Advanced Design and Manufacturing Technology 5(1), (2011).
3. Itou S. Thermal stress intensity factors of an infinite orthotropic layer with a crack. International Journal of Fracture 103(3), (2000) 279–291.
4. Thompson W. (Lord Kelvin), Note on the integration of the equations of equilibrium of an elastic solid. Cambridge and Dublin Math. J 3, (1848) 87–89.
5. Green G. An essay on the application of mathematical analysis to the theories of electricity and magnetism, Nottingham, England, T. Wheelhouse, (1828) 10–12.
6. Lamé G. Leçons sur la théorie mathématique de l'élasticité des corps solides, (1852).
7. Boussinesq J. Application des potentiels a l'e´tude de l'e´quilibre et du mouvement des solides e´lastiques, Gauthier–Villars, (1885).
8. Hertz H. Vber die beruhrung fester elastischer korper (On the contact of elastic solids). J. Reine Angew. Math. 92, (1882) 156-171 (in German).
9. Cerruti V. A Treatise on the mathematical theory of elasticity in: A.E.H. Love (ed.), Fourth edition, Dover Publications, New York, (1882) 16.
10 Southwell RV. On the concentration of stress in the neighborhood of a small spherical flow. Phil. Mag., Ser. 7,1, (1926) 71.
11. Mindlin RD. Force at a point in the interior of a semi–infinite half space, Journal of Applied Physics 79, (1936) 195-202.
12. Barber JR, Ciavarella M. Contact mechanics in research trends in solid mechanics, (ed. G. Dvorak), International Journal of Solids and Structures, 37, (2000) 29–43.
13. Muskhelishvili NL. Singular integral equations, P. Noordhoff Ltd., Groningen, The Netherlands, 1953. (based on the second Russian edition published in 1946).
14. England AH. Complex variable methods in elasticity, Wiley Interscience, London, 1971.
15. Johnson KL. Contact Mechanics, Cambridge University Press, 1987.
16. Erdogan F. Mixed boundary value problems in mechanics. in: Nemat–Nasser, S. (ed.), Mechanics Today 4, Pergamon Press, (1978) 1-86.
17. Erdogan F. Approximate solutions of systems of singular integral equations, SIAM J. Appl. Math. 17 (1969) 1041-59.
18. Stroh A. Dislocations and cracks in anisotropic elasticity, Philos. Mag. 3(30) (1958) 625-646.
19. Stroh A. Steady state problems in anisotropic elasticity, J. Math. Phys., 41(2) (1962) 77-103.
20. Lekhnitskii SG. Theory of elasticity of an anisotropic elastic body, Holden–Day, San Francisco 1963.
21. Sveklo VA. Boussinesq type problems for the anisotropic half–space, J. Appl. Math. Mech. 28 (1964) 1099-1105.
22. Willis JR. Hertzian contact of anisotropic bodies, J. Mech. Phys. Solids 14 (1966) 163-176.
23. Shi AA, Lin Y, Ovaert TC. Indentation of an orthotropic half–space by a rigid ellipsoidal indenter, J. Tribol. 125 (2003) 223-231.
24. Kahya V, Birinci A, Erdol R. Frictionless contact problem between two orthotropic elastic layer, International Journal of Computational and Mathematical Sciences 1 (2007) 121-127.
25. Batra R, Jian W, Analytical solution of the contact problem of a rigid indenter and an anisotropic linear elastic layer, Int. J. Solids Struct 45(22) (2008) 5814-5830.
26. Bagault C, Nelias D, Baietto MC, Contact analyses for anisotropic half space: effect of the anisotropy on the pressure distribution and contact area. Journal of Tribology 134 (3) (2012).
27. Ashrafi H, Mahzoon M, Shariyat M. A new mathematical

modeling of contact treatment between an orthotropic material and a rigid indenter, Iranian Journal of Materials Science and Engineering 9(1) (2012) 29–41.
28. Dong X–Q, Zhou Y–T, Wang L–M, Ding S–H, Park J–B. Stress state of two collinear stamps over the surface of orthotropic materials, Arch Appl. Mech (2014)
29. Ramirez G, Heyliger P. Frictionless contact in a layered piezoelectric half–space, Smart Mater. Struct 12 (2003) 612–625.
30. Ramirez G. Frictionless contact in a layered piezoelectric medium characterized by complex eigenvalues, Journal of Smart Materials and Structures, 15(5) (2006) 1287–1295.
31. Zhou YT , Lee, KY. Exact solutions of a new, 2D frictionless contact model for orthotropic piezoelectric materials indented by a rigid sliding punch, Philosophical Magazine 92(15) (2012) 1937–1965.
32. Zhou YT, Lee KY, Frictional contact of anisotropic piezoelectric materials indented by flat and semi–parabolic stamps, Arch Appl. Mech. 83 (2013) 73–95.
33. Krenk S. On the elastic constants of plane orthotropic elasticity, Journal of Composite Materials 13 (1979) 108–116.
34. Cinar A, Erdogan F. The crack and wedging problem for an orthotropic strip, International Journal of Fracture (1982) 83–102.
35. Ozturk M, Erdogan F. Mode I crack problem in an inhomogeneous orthotropic medium, International Journal of Engineering, Sci. 35(9) (1997) 869–883.
36. Ozturk M, Erdogan F. The mixed mode crack problem in an inhomogeneous orthotropic medium, International Journal of Fracture 98, (1999) 243–261.
37. Guler MA. Contact stresses in an orthotropic medium: a closed–form solution, International Journal of Mechanical Sciences 87 (2014) 72–88
38. Guler MA, Erdogan F. Contact mechanics of graded coatings, International Journal of Solids and Structures 41, (2004) 3865–3889.
39. Guler MA, Erdogan F. Contact mechanics of two deformable elastic solids with graded coatings, Mechanics of Materials, 38(2006) 633–647.
40. Guler MA, Erdogan F. The frictional sliding contact problems of rigid parabolic and cylindrical stamps on graded coatings, International Journal of Mechanical Sciences49(2) (2007) 161–182.
41. Kucuksucu A, Guler MA, Avci A. Closed–form solution of a frictional sliding contact problem for an orthotropic elastic half–plane indented by a wedge–shaped punch, Key Engineering Materials 618 (2014) 203–225.
42. Bakırta I. The contact problem of an orthotropic non–homogeneous elastic half space, International Journal of Engineering Science, 22 (1984) 347–359.
43. Erdogan F. Fracture materials and contact problems in materials involving graded coatings and interfacial zones, Final Technical Reports, Lehigh University, (2001).
44 Chou YT. Interaction of parallel dislocations in a hexagonal crystal, Journal of Applied Physics 33 (1962) 2747–2751.
45. Erdogan F, Gupta GD, Cook TS. Numerical solution of singular integral equations, method of analysis and solution of crack problems, G.C. Sixth (ed.), Noordhoff, Int. Publ. Leyden, (1973) 368–425.
46. Erdogan F, Gupta GD. On the numerical solution of singular integral equations, Quarterly of Applied Mathematics 29 (1972) 525–534.
47. Conner BP. Contact fatigue: Life prediction and palliatives, Ph.D Thesis, Massachusetts Institute of Technology (2002).

Hittite Journal of Science and Engineering, 2016, 3 (2) 73-80
ISSN NUMBER: 2149-2123
DOI: 10.17350/HJSE19030000034

Effect of Precursor Type on Zinc Oxide Formation and Morphology Development during Hydrothermal Synthesis

Emel Özel, İkbal Gözde Tuncolu, Cem Açıksarı, Ender Suvacı
Anadolu University, Department of Materials Science and Engineering, Eskisehir, TURKEY

ABSTRACT

Semiconducting metal oxide sensors have been widely studied due to their small dimensions, low cost and low power consumption. ZnO is a potential material for gas sensor applications because of its high piezoelectric coefficient, great stability of its hexagonal phase and its pyroelectric property. Hydrothermal synthesis is one of the most useful methods to produce homogeneous, nanosized ZnO powders with high purity, controlled particle size and morphology. The research objectives of this study were to understand formation and growth process of ZnO particles with various morphologies and to investigate role of starting materials, (i.e., zinc chloride ($ZnCl_2$) and zinc nitrate hexahydrate ($Zn(NO_3)_2.6H_2O$) on the particle morphology. ZnO particles with various morphologies were synthesized via an unstirred hydrothermal method. When using $ZnCl_2$ as a precursor, the final morphology was rod like with a taped tip (length of the rod 0.5-1 µm) after 12 h at 100 °C. On the other hand, final morphology of the produced ZnO particles was branch rod like (5-10 µm) when using $Zn(NO_3)_2.6H_2O$ as precursor under the same synthesis conditions. Accordingly, a proposed growth mechanism has been suggested.

Article History:
Received:2016/08/02
Accepted:2016/10/31
Online: 2016/12/31

***Correspondence to**: Emel Ozel, Anadolu University, Department of Materials Science and Engineering, Eskisehir, TURKEY*
Tel: +90 222 3213550/6347
Fax: +90 (222) 3239501
E-Mail: eozel@anadolu.edu.tr

Keywords: ZnO; Hydrothermal synthesis; Phase development; Morphology; Growth mechanism

INTRODUCTION

Zinc oxide is an important technological material due to its wide band gap (3.37 eV), high electron mobility and large exciton binding energy at room temperature [1]. Because of these unique characteristic, zinc oxide (ZnO) is a very attractive materials for various applications such as conductive oxide, antistatic coating, sensors, band gap optoelectronic devices, pigments and an UV filters in sunscreens. Depending upon the different synthesis methods, it can be synthesised with various type of morphology such as rod like, sphere like, flower like or urchinlike morphologies [1-3]. The crystal structure, particle size and morphology of ZnO particles are important parameters which affect the properties of the powder and hence determine application areas. For example, ZnO particles with large surface area can be utilised for enhancing gas sensing applications [4] where the amount of absorbed oxygen is strongly depending on morphology, surface area and grain size of the sensing material [5].

The morphology of ZnO crystals strongly depends on the type of precursor and mineralizers in the form of different zinc salts in alkaline solution such as Zn-nitrate, Zn-acetate and Zn-chloride with alkaline KOH, NaOH or NH_4OH. The solubility of ZnO in these solutions varies with the pH and concentration, and depending on the OH^- concentration and temperature, various Zn^{2+} -hydroxo complexes are formed. From these complexes, the ZnO precipitates through condensation reaction [6]. Particle size and morphology are also dependent on powder synthesis method and parameters (temperature, time, concentration etc.). Zang et al. reported the controlling of ZnO morphology by using different precursor ($Zn(OH)_4^{2-}$ and $Zn(NH_3)_4^{2-}$) and simple solution route. They founded that ZnO particles had a prismlike morphology after reaction process where NH_3 was formed as a by-product from $Zn(NH_3)_4^{2-}$ whereas ZnO particles had a rod like or the flower like morphology depending on the concentration of OH^- in the $Zn(OH)_4^{2-}$ solution [2].

Sing et al. studied the effect of the different precursor solutions (zinc chloride, zinc nitrate and zinc acetate) on the morphology of ZnO and its sensing behaviour by co-precipitation method. They found out that among

all the precursor solution, zinc acetate yielded most suitable morphology of zinc oxide with small length rods (about 400-800 nm) which exhibited enhanced sensing response towards alcohols [4]. Rai et al. have also studied the synthesis of ZnO nanostructures from different precursors (zinc chloride, zinc nitrate and zinc acetate) via solvothermal method and established the relationship between morphology and gas sensing behaviour by comparing their response. They found that the shape and size of ZnO nanostructures greatly affected the gas sensing property and the response of ZnO nanorods synthesised from zinc nitrate or zinc acetate was higher than ZnO particles synthesised from zinc chloride for NO_2 and CO gases [3].

Hydrothermal synthesis is one of the most useful method among the other solution based synthesis methods such as direct strike and homogeneous precipitation, microemulsion, sol-gel, gel combustion etc. to produce homogeneous, nanosized ZnO powders with high purity, controlled particle size and morphology. An important advantage of this method is that the purity of hydrothermally synthesized powders significantly exceeds the purity of the starting materials.

There are several studies on the effect of precursor and synthesis parameters on morphology of ZnO for different synthesis methods such as co-precipitation, solvothermal and hydrothermal method. However, the effect of precursors which have acidic or basic nature on the particle morphology of ZnO crystals and growth mechanism in the different solution characteristics has not well understood yet for hydrothermal synthesis. Therefore, in the present study, the research objectives were to investigate role of starting materials, (i.e., zinc chloride ($ZnCl_2$) and zinc nitrate hexahydrate ($Zn(NO_3)_2.6H_2O$)) on the particle morphology by using hydrothermal synthesis and understand formation and growth mechanisms of ZnO particles with various morphologies.

MATERIALS AND METHODS

In this study, zinc chloride ($ZnCl_2$; Merck) and zinc nitrate hexahydrate ($Zn(NO_3)_2.6H_2O$; Sigma aldrich) were used as zinc sources to produce zinc oxide by hydrothermal method. All of the chemicals were of analytical grade (>99.99 % purity) and were used without further purification. Zinc chloride or zinc nitrate hexahydrate were dissolved into distilled water to form transparent solution (0.25-1 M), and then, 4 M ammonium hydroxide (NH_4OH) solution, used as a mineralizer (pH=8.4), was added dropwise into the salt solution during magnetic stirring. To prevent the effect of anions on the formation mechanisms of ZnO powder, the precipitates were centrifuged at 5000 rpm for 5 min and washed in several times with deionized water to remove residual anions.

The precipitated product with pH 8.9 was charged into an autoclave (600 ml capacity) up to 60 % fill. The hydrothermal reaction was conducted at 100 °C for 1-24 h under autogenous pressure. After the autoclave reached 100°C, 5 minutes soaking time was given to all samples in order to achieve temperature stability. After the hydrothermal reaction was completed, the autoclave was cooled down to room temperature. The product was washed with distilled water and dried in an oven at 90 °C over a period of 24-48 h. The phase development of the ZnO powder was analysed by the x-ray diffraction (XRD) method (Rigaku Co. Ltd., Tokyo, Japan) with a monochromatic CuKα radiation source (λ = 1.542 Å) between 10 ° and 80 ° with 2 °C/min scan rate. The effects of processing parameters such as the precursor type, initial concentrations of materials and reaction time on the morphology and particle size of the ZnO powders were investigated by a scanning electron microscope (SEM; Zeiss Supra 50 V, Carl-Zeiss, Germany) and scanning transmission electron microscopy (STEM; JEOL 2100F, FEI, 200 kV HRTEM, Japan). The transmission electron microscopy (TEM) sample was prepared by sonicating the ZnO crystals in ethanol and drop casting them on carbon coated TEM grids. The average particle size of synthesised powder was measured by using SEM images corresponding Image J programme. Particle size and distribution of each samples was calculated by monitoring of approximately 30 individual particles in the SEM images.

RESULTS AND DISCUSSION

Phase development

To examine the phase formation of ZnO depending on the precursor type, ZnO powders were synthesised under hydrothermal synthesis conditions at 100 °C for 0-3 hours using different precursors ($ZnCl_2$ and $Zn(NO_3)_2.6H_2O$). The XRD patterns of these powders synthesised at different time (0-3h) are given in Figures 1 and 2. Starting with $ZnCl_2$ salt solution, simonkolleite ($Zn_5(OH)_8Cl_2.H_2O$)

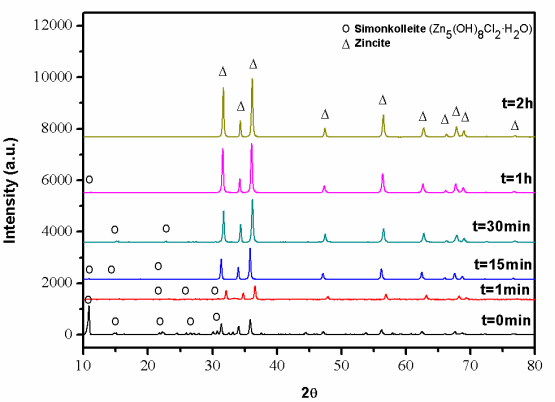

Figure 1. XRD patterns of ZnO powders synthesised using $ZnCl_2$ precursor at different time (0-2h).

was observed as a major phase with a small amount of zincite (zinc oxide) at t=0 min (Fig. 1). After 1h, all of the peaks can be well indexed by the zincite (ZnO; JCPDS No. 89-1397). Starting with $Zn(NO_3)_2.6H_2O$ precursor, zincite phase and unidentified peaks probably belong to zinc hydroxide complexes as reported earlier in the literature [6] were detected at t=0 min. After 3 h, pure zincite was formed as shown in Figure 2.

Effect of the treatment time on particle size and morphology

To investigate the effect of the treatment time on the phase formation and particle characteristics, ZnO powders were hydrothermally synthesized at 100 °C for different times from different precursors ($ZnCl_2$ and $Zn(NO_3)_2.6H_2O$). Figure 3 shows the SEM images of the ZnO powders prepared by using $ZnCl_2$ precursor for different times. At t=0 min, the zinc containing gel was occurred and a small amount of ZnO precipitated on this zinc containing gel (Fig. 3a). Small amount of ZnO and incomplete phase of $Zn_5(OH)_8Cl_2.2H_2O$ dissolved and ZnO particles with ellipsoidal morphology occurred during hydrothermal synthesis for 15 min (Fig.3b). When treatment time reaches the 2 h (Fig.3f), all intermediate phase of $Zn_5(OH)_8Cl_2.2H_2O$ dissolve and single phase ZnO particles was formed as evidenced by the XRD results given in Fig.2 and Fig.3. As shown in Figure 3f, ZnO particles exhibit high uniformity with respect to size and morphology after 2 h of hydrothermal treatments. The length of individual ellipsoidal rod like ZnO crystals with a taped tip was about 0.5-1 µm with high aspect ratio.

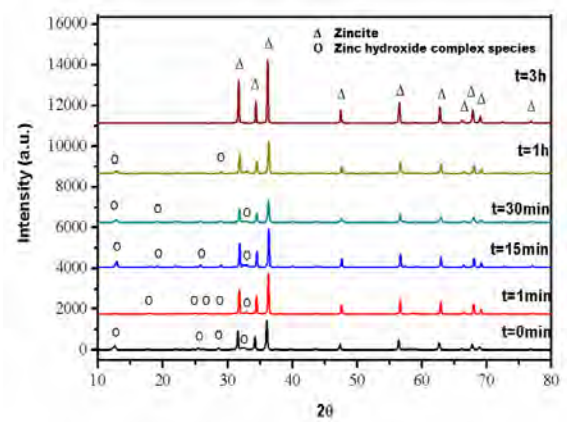

Figure 2. XRD patterns of ZnO powders synthesised using $Zn(NO_3)_2.6H_2O$ precursor at different time (0-3h)

Figure 4 shows the SEM images of the ZnO powders prepared using $Zn(NO_3)_2.6H_2O$ precursor. Even at t=0 min (Fig. 4a), as confirmed by XRD data, large amount of ZnO particle precipitation was observed. Precipitated ZnO does not dissolve completely and dissolved gel begins to grow on the existing ZnO particles with branch rod like morphology during hydrothermal synthesis. After 3h (Fig. 4f), all gel phase completely disappeared and branch rod like ZnO particles which looks like flower with an average length of 5-7 µm.

SEM images of ZnO crystals given in Figure 3 and Figure 4 clearly show that crystal morphology of ZnO particles was strongly affected from precursor type. ZnO crystals grew as an individual ellipsoidal rod like with a taped tip when used $ZnCl_2$ precursor, but branch rod like ZnO particle with flower shape were formed when used $Zn(NO_3)_2.6H_2O$ precursor.

In the light of the literature, these differences observed in the crystal morphologies can be explained with nature of ZnO and suspension pH and characteristics. Each crystallographic plane of ZnO exhibits different growth kinetics due to different attachment ratio of the growth unit [$Zn(OH)_4^{2-}$] to crystallographic planes [8]. The order of the crystallographic planes according to their growth rate in ZnO is follows; V(0001)>V(Ï0IÏ)>V(Ï010)>V(Ï011)>V(000Ï). Since the plane with greater growth rate disappears earlier [7], the (0001) plane, the most rapid growing plane, disappears during the hydrothermal process while other planes grow, which leads to the pointed (taped) shape in and of the c axis as observed in Figure 3f.

Different crystal growth rate along certain crystal faces are also affected from various solution basicities. The acidic strength of the zinc oxide precursors affects the crystal growth rate is in the following manner: chloride>nitrate>acetate [2]. Since $ZnCl_2$ is acidic salt, it induced chemical etching of the polar surface of ZnO and as a result rods with tapered ends were obtained [4]. However $Zn(NO_3)_2.6H_2O$ precursor which has a basic characteristic yields the branches rod like morphology.

Morphology of the ZnO crystals is controlled by altering pH of solution. At lower pH, smaller petal like or rod like ZnO crystals are formed where the nucleation is less intense and the final crystals obtained an energetically more favourable, elongated morphology. At higher pH, there are larger numbers of strongly nucleophilic OH- groups, which absorb to the Zn-terminated surfaces and hinder in plane crystallization, while the prismatic planes grow without constrain. Consequently at higher pH values the crystals growth in the [0001] direction is hindered and the resulting crystals are plate-like [6].

Effect of the cation concentration on particle size and morphology

Figure 5 shows the SEM images of ZnO particles synthesised from $ZnCl_2$ precursor at 100°C for 24 h with diffe-

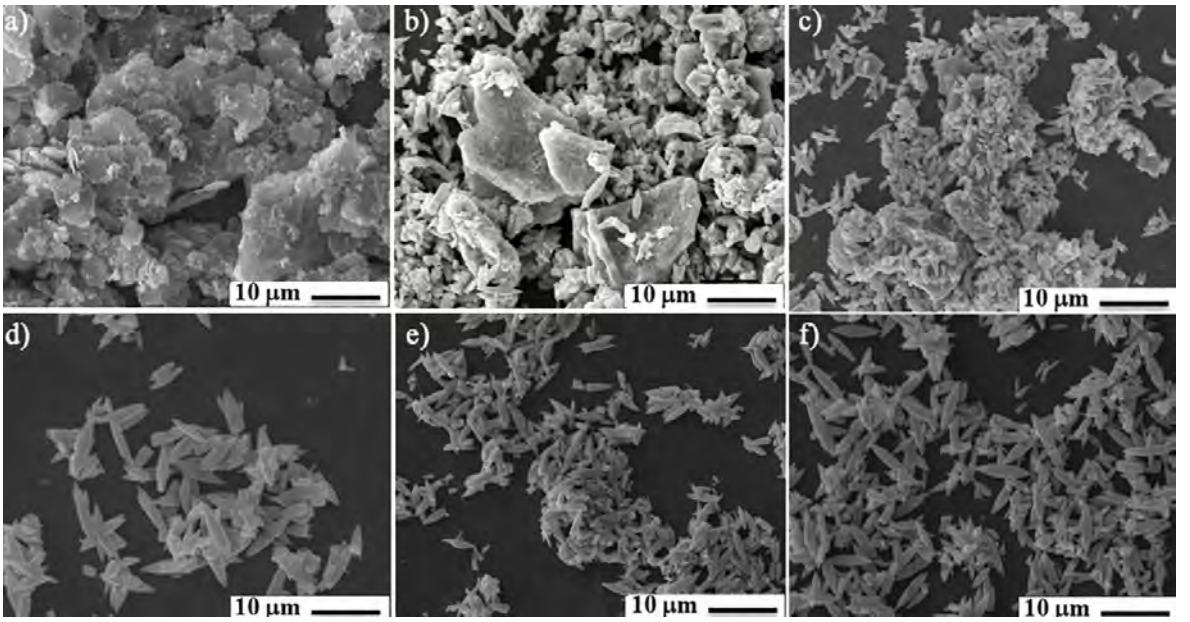

Figure 3. SEM images (10 µm) of ZnO powders synthesised using $ZnCl_2$ precursor at (a) 0 min (b) 1 min (c) 15 min (d) 30 min (e) 1 h and (f) 2 h treatment times.

rent initial concentration ratios (0.25, 0.50, 0.75 and 1 M).

Individual ellipsoidal rod like ZnO particles with tapered tip were formed at 0.25 and 0.5 M concentration values given in Fig.5a and Fig.5b. With increasing initial concentration to 0.75 and 1 M, ellipsoidal rod like ZnO particles were had a tendency to agglomerate (Fig. 5c and Fig. 5d). Average particle size of crystals determined from SEM images decreased sharply from 12 µm to 3µm by length as shown in Figure 6.

Figure 7 shows the SEM images of ZnO particles synthesised from $Zn(NO_3)_2.6H_2O$ precursor at 100°C for 24 h with different initial concentration ratios (0.25, 0.50, 0.75 and 1 M). As shown in Fig. 7a, ZnO particles with branch rod like morphology formed at low cation concentration value (at 0.25 M). With increasing molarity of zinc nitrate solution, flower like morphology was observed (Fig. 7b-d) and average particle size of flower like particles increased from 5 µm to 12µm by length as shown in Figure 8.

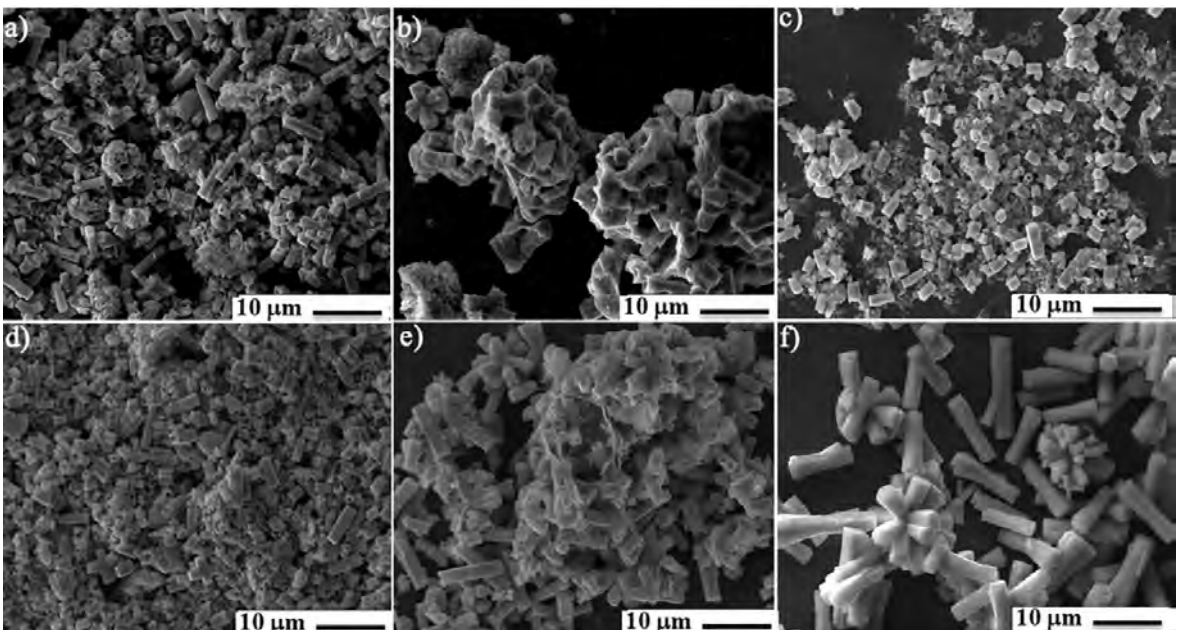

Figure 4. SEM images (10 µm) of ZnO powders synthesised using $Zn(NO_3)_2.6H_2O$ precursor at (a) 0 min (b) 1 min (c) 15 min (d) 30 min (e) 1 h, and (f) 3 h treatment times.

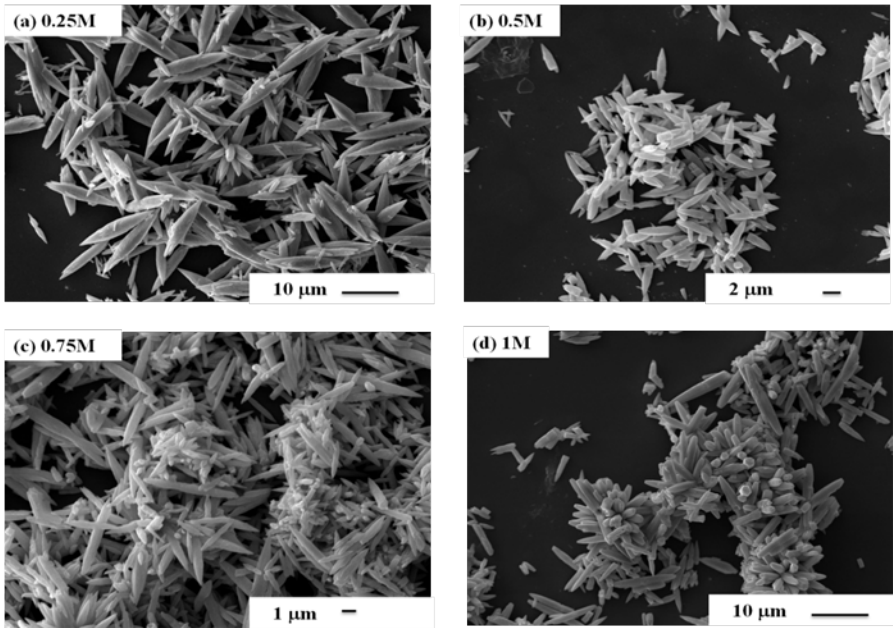

Figure 5. SEM images of ZnO powders synthesised using $ZnCl_2$ precursor with initial concentration of (a) 0.25 M (b) 0.5 M (c) 0.75 M and (d) 1 M.

Flower like branched ZnO particles produced from 0.5 M $Zn(NO_3)_2.6H_2O$ precursor were also analyzed by using scanning transmission electron microscope (STEM). STEM image of such a particle is presented in Figure 9. As shown in Figure 9, rods on the flower like particle were grown in different directions from center of the particle and all of the rods were single crystals. Average particle size of a flowerlike particle was determined as 4-6 µm and average rod length and width in this flower like particle were 5.843 µm and 0.549 µm, respectively.

Proposed growth model

The growth habit of ZnO crystal particles and the effect of reaction medium on the growth habit were successfully explained by Li and co-workers [8]. In solution, the growth unit of a crystal is the complex that is formed by the connection of cation with OH^- ions. In the supersaturation solution, zinc hydroxide gel dissolved in the solution complex with OH^- ions forms growth units ($Zn(OH)^{2-}_4$) by the attraction of ions as follows:

$$Zn(OH)_2\,(jel) + 2H_2O = Zn^{2+} + 2OH^- + 2H_2O = Zn(OH)^{2-}_4 + 2H^+ \quad (1)$$

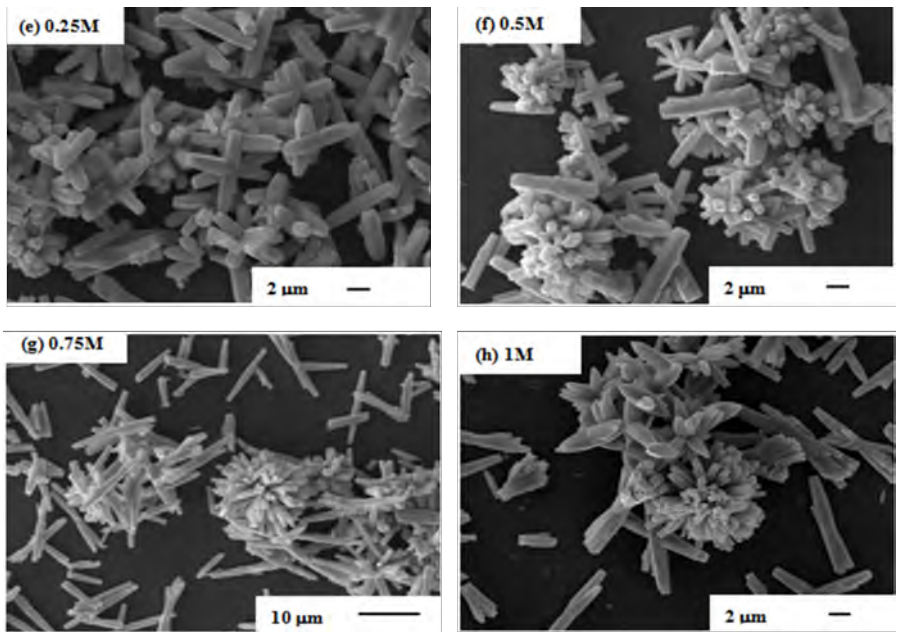

Figure 7. SEM images of powders synthesised using $Zn(NO_3)_2.6H_2O$ precursor with initial concentration of (a) 0.25 M (b) 0.5 M (c) 0.75 M and (d) 1 M.

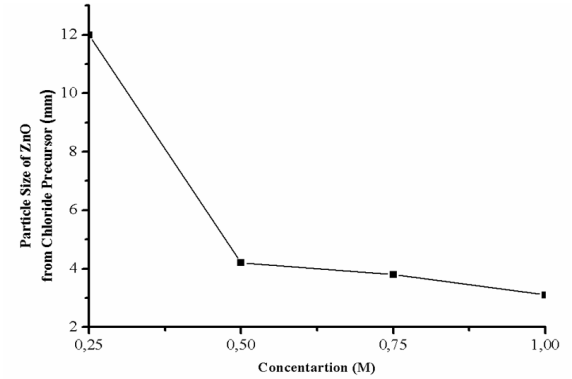

Figure 6. Average particle size of ZnO synthesised using $ZnCl_2$ precursor depending on cation concentration.

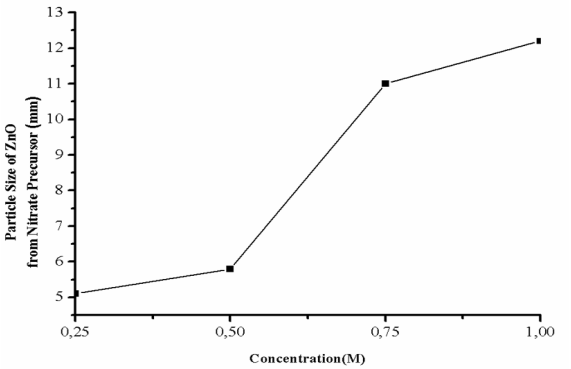

Figure 8. Average particle size of ZnO synthesised using $Zn(NO_3)_2.6H_2O$ precursor depending on cation concentration.

Since the growth unit ($Zn(OH)^{2-}_4$) incorporating into the crystal lattice take place by the dehydration reaction between OH^- ligands, the growth habit of the ZnO crystal is related to OH^- ligands at the interface or the reaction medium [8,9].

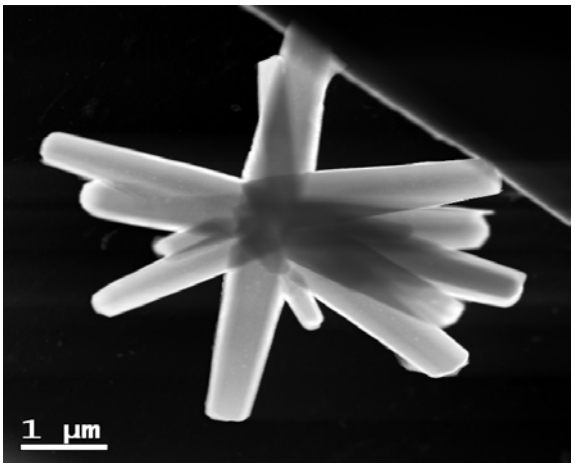

Figure 9. STEM image of flower like ZnO particle produced from 0.5M $Zn(NO_3)_2.6H_2O$ precursor.

In our study, different particle size and morphology of ZnO particles were obtained when different $ZnCl_2$ and $Zn(NO_3).6H_2O$ precursor were used and this is consistent with the previously reported studies.

It is clear that concentration of OH^- ions and existence of Cl^- and NO_3^- ions in the medium affect the growth mechanism of ZnO particle. However, more works is needed to be done for further understanding.

According to the obtained results in this study and the literature, growth process of ZnO particles synthesized by using different precursor can be simply illustrated as shown in Figure 10. Starting with $ZnCl_2$ precursor, small amount of ZnO phases (Figure 1, at t=0) precipitate on the unstable simonkolloite phase in the initial stage of the synthesis and new ZnO nuclei were formed from simonkolloite phase during the chemical reaction. With increasing the reaction time of the hydrothermal synthesis to 30 min, ZnO crystals grow and large ellipsoidal rod like crystals of ZnO start to appear (as shown in Figure 3). With increasing concentration of $ZnCl_2$ precursor, particle size of individual ellipsoidal rod like ZnO crystals reduced as shown in Figure 5 and Figure 6. Therefore, it can be concluded that zinc oxide powders synthesized from $ZnCl_2$ precursor are grown via classical nucleation and growth theory mechanism. In the classical crystallisation mechanism, the crystal grows from a stable nucleus in a supersaturated solution. Raising the concentrations of reactants makes the reaction happen at a faster rate. Following a very fast nucleation period the material crystallizes with a very narrow size distribution. Since the reaction take place rapidly, particles (kinetically favoured) need no more time to growth as a result smaller particle is formed [8].

In the case of starting with $Zn(NO_3).6H_2O$ precursor, the small rod like ZnO crystals and zinc hydroxide complex were coexist in the initial stage (Figure 4a). With increasing the reaction time to 30 min, these phases dissolved and then recrystallized as a branched rod like ZnO crystal. With increasing initial concentration of precursor, average particle size of branched rod like particles increases and the flower like particles are formed as shown in Figure 7b-d. According to these results, it can be concluded that zinc oxide particles grow via Ostwald ripening mechanism under such conditions.

Ostwald ripening process is a spontaneous process that occurs because larger crystals are more energetically favored than smaller crystals. In this case, kinetically favored tiny crystallites nucleate first in supersaturated medium and are followed by the growth of larger particles (thermodynamically favored) due to the energy difference between large and smaller particles of higher solubility based on the Gibbs-Thomson law [10]. The aqueous solution of zinc nitrate can produce $Zn(OH)_2$ in the presence of OH^- ions. During the hydrothermal process, part of the $Zn(OH)_2$ dissolves into Zn^{2+} and OH^-. When the concentration of Zn^{2+} and OH^- re-

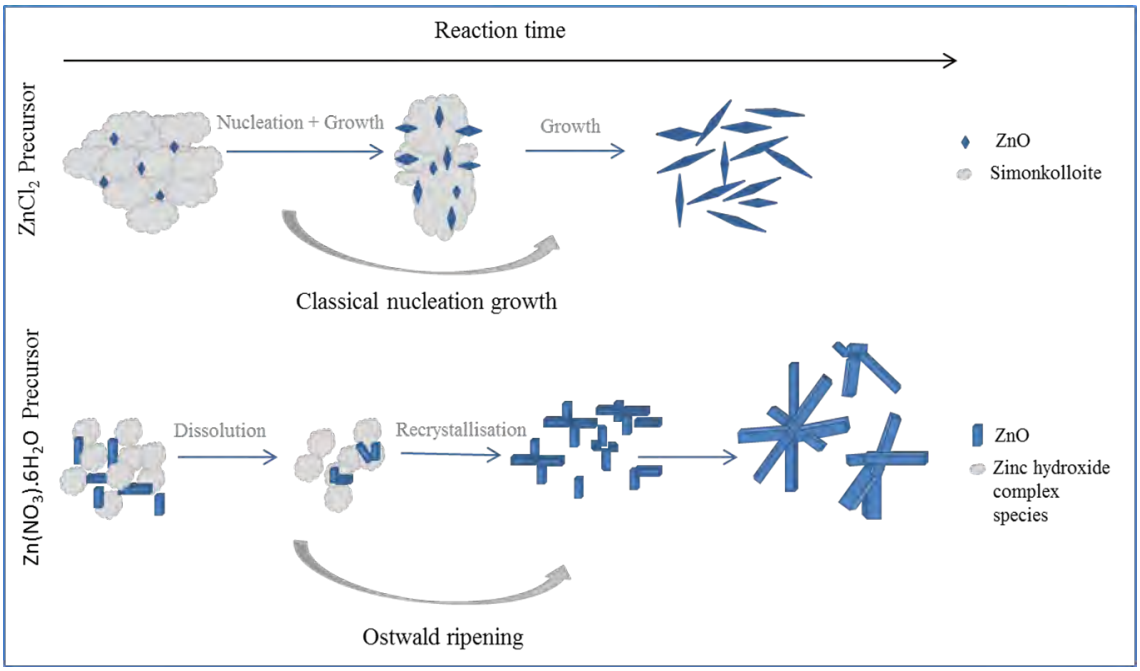

Figure 10. Proposed growth mechanisms of ZnO particles synthesized from different precursor.

aches the supersaturation degree of ZnO, ZnO nuclei will form spontaneously in the aqueous complex solution[7].

CONCLUSIONS

In this study, the dependence of the phase development and particle characteristics of the resulting ZnO powders on the precursors with initial concentration and synthesis time was evaluated during hydrothermal process. Results reveal that morphology and particle size of ZnO powder can be controlled by different precursors. With using $ZnCl_2$ precursor, agglomerated ellipsoidal rod like morphology was formed whereas flower like morphology was obtained with using $Zn(NO_3).6H_2O$ precursor. Particle size of ZnO crystals were also affected from precursor type and initial concentration. With increasing concentration of precursors, average particle size of ZnO crystals was decreased from 12 µm to 3 µm using $ZnCl_2$ precursor in contrast, it was increased from 5 µm to 12 µm using $Zn(NO_3).6H_2O$. Accordingly, zinc oxide particles grow via classical nucleation theory by using $ZnCl_2$ and Ostwald ripening mechanism by using $Zn(NO_3).6H_2O$. The proposed growth mechanism was depicted as shown in Figure 10.

These results are particularly important to demonstrate that ZnO powder can be synthesized in different size and morphology by the hydrothermal method changing precursor type and concentration. These results can be successfully used in different application areas where designing of the specific particle morphology is needed to enhance the particle performance.

ACKNOWLEDGEMENTS

This study was sponsored by a bilateral research project between Turkey & Russia under the contact number 111M670 by the Scientific and Technological Research Council of Turkey (TUBITAK). The work was also supported by Anadolu University under the contract numbers 1303F056.

REFERENCES

1. Polsongkram D, Chamninok P, Pukird S, Chow L, Lupan O, Chai G, Khallaf H, Park S, Schulte A. Effect of synthesis conditions on the growth of ZnO nanorods via hydrothermal method. Physica B 403 (2008) 3713–3717.
2. Zhang J, Sun L, Yin J, Su H, Liao C, Yan C. Control of ZnO morphology via a simple solution route. Chem. Mater. 14 (2002) 4172–4177.
3. Rai P, Kwack W, Yu Y. Solvothermal synthesis of ZnO nanostructures and their morphology–dependent gas–sensing properties. Applied Materials Interfaces 5 (2013) 3026–3032.
4. Singh O, Kohli N, Singh RC. Precursor controlled morphology of zinc oxide and its sensing behaviour. Sensors and Actuators B, 178 (2013) 149–154.
5. Korotcenkov G, The role of morphology and crystallographic structure of metal oxides in response of conductometric–type gas sensing. Materials Science and Engineering Reports 61(2008) 1–39.
6. Podlogar M, Recnik A, Yılmazo lu G, Ozer O, Mazaj M, Suvaci E, Bernik S. The role of hydrothermal pathways in the evolution of the morphology of ZnO crystals. Ceramic Internationals, 42, 14 (2016) 15358–15366.
7. Zhang H, Yang D, Yi YJ, Ma XY, Xu J, Que DL. Low temperature synthesis of flowerlike ZnO nanostructures by cetyltrimethylammonium bromide–assisted hydrothermal

process. Journal of Physical Chemistry B, 108, 13 (2004) 3955-3958.
8. Li WJ, Shi EW, Zhong WZ, Yin ZW. Growth mechanism and growth habit of oxide crystals. J. Cryst. Growth, 203 (1999) 186–196.
9. Ozer IO, Texture development in ZnO–based varistors, effects of inversion boundaries on texture development and relationships between texture and electrical characteristics, Anadolu University, Doctorate thesis, May 2010.
10. Mullin JW. Crystallisation, third ed. Butterworth/Heinemann, Oxford, 1997.

Hittite Journal of Science and Engineering, 2016, 3 (2) 81-85
ISSN NUMBER: 2149-2123
DOI: 10.17350/HJSE19030035

Influence of Mechanical Surface Treatments on Sandelin Phenomenon in Silicon Containing Steels

Oktay Elkoca[1] and Cevat Serdar Küçükkaragöz[2]

[1] ArcelorMittal Global R&D Center, East Chicago, IN, USA

[2] University of the Witwatersrand, School of Chemical and Metallurgical Engineering, Wits 2050, Johannesburg, SOUTH AFRICA

ABSTRACT

In this study, the influence of mechanical surface treatments on the Sandelin Phenomenon in silicon containing steels was investigated. For this purpose, various surface topographies with/without deformed zones were produced on the steel samples with different silicon contents by applying mechanical surface treatments such as grinding, and polishing in addition to conventional pickling. Hot-dip galvanized coatings formed on the conditioned surfaces were examined through cross-sections with optical microscope and scanning electron microscope. The results indicate that surface topography is the main factor controlling the stability of a hot-dip galvanizing coating and a surface topography with intermediate roughness and sharp asperities formed with abrasive particles in the range of 100 - 270 µm can produce suitable coatings on the silicon containing steels.

Article History:
Received: 2016/09/07
Accepted: 2016/10/22
Online: 2016/12/31

***Correspondence to**: Oktay Elkoca, ArcelorMittal Global R&D Center, 3001 East Columbus Drive, East Chicago, IN 46312-2939, USA*
Tel: +1 (312)7720874
E-Mail: oelkoca@gmail.com

Keywords: Hot-dip galvanizing; Sandelin Phenomenon; Silicon containing steels; Fe-Zn alloy layers

INTRODUCTION

Hot-dip galvanizing is a widely used process for the protection of iron-based materials from corrosion. Coating characteristics such as corrosion resistance, thickness, appearance, and mechanical properties are primary parameters in this process. All of these parameters are influenced by the shape and thickness of the Fe-Zn alloy layers formed during galvanizing process. Chemical composition, geometrical shape, surface condition and dipping time of the parts to be galvanized and temperature of the zinc bath affect the formation of Fe-Zn alloy layers [1-15]. Silicon content higher than 0.03% in a steel is regarded critical since it leads to a reactive behavior that deteriorates the properties of hot-dip galvanized coating. This behavior is known as Sandelin Phenomenon [1], which changes the structure of the stable diffusion layers in the coating into another form composed of fine and discrete ζ crystals surrounded by η phase. The phenomenon causes an uncontrollable growth in hot-dip coating galvanizing coatings, which reach to a peak value at 0.08% Si as shown in the Sandelin Curve [1]. The fast growing ζ crystals leads to extremely thick coating layers, which cause over consumption of zinc and form brittle coatings with irregular thickness and poor surface characteristics.

In addition to the composition, surface properties of the steel also play an important role on the coating properties [5-8]. A prior forming process modifying surface topography subsequently may also alter the coating properties. Effect of the surface topography on the coating behavior can be explained by concave and convex surfaces produced on the steel in where the convex surfaces produce scattered alloy layers whereas the concave surfaces favor the growth of iron rich regions producing more compact and continuous layers [6].

To explain reactive behavior in hot-dip galvanizing coatings, a different theory has been proposed by Vazquez, which is called Reactive Zone Theory [15]. According to Vazquez, formation of subsurface oxide phases and heterogeneous presence of Si rich regions in hot rolled steel sheet affect the development of alloy layers

during galvanizing. Presence of Si rich zones is considered to be effective on over growing of ζ phase. However, parameters controlling the formation of Si rich regions have not been clearly defined and the distribution of Si enriched regions requires further detailed analytical work to be carried out through extended surfaces.

Researchers have proposed various theories on the parameters affecting the coating characteristics [5-8, 15]. The complexity of the parameters which comprise surface roughness, deformed layers and silicon content in subsurface regions introduces difficulty in finding out a solution to the problem. In this study, these parameters were isolated from each other and the effect of each parameter on coating behavior was elucidated.

EXPERIMENTAL

Samples in size of 3 x 30 x 70 mm were cut off from hot rolled steel sheets with silicon contents associated with the Sandelin Curve, in where normal and reactive coatings can be encountered (Table 1).

Galvanizing experiments were carried out in a zinc bath at 450°C ±2°C. The zinc bath contained 0.03% Fe, which is the saturation level of iron at 450°C, 1.0% Pb to increase fluidity, and 0.010% Al to improve oxidation resistance.

The samples were first cleaned with NaOH of 100 g/l at 70°C for 10 minutes and then pickled with HCl of 25 vol. % containing inhibitor Rodine 50 at room temperature for 10 minutes. Afterwards, a group of samples was ground with 60 grit SiC paper in order to generate a specific roughness. Other group was first ground with 240 grit SiC paper, and after a series of grinding process finally polished with 1μm diamond paste to obtain smooth polished surfaces with negligible deformation.

Surface topography of the conditioned samples was examined with Jeol 5600 JSM Scanning Electron Microscope (SEM) and surface roughness (Ra) of the surfaces was measured using Mitutoyo Surftest 301 Profilometer. For cross-sectional examinations, the surfaces were electrolytically plated with nickel to avoid edge rounding during metallographic sample preparation. The plated samples were metallographically prepared according to the method explained by Jordan et al [16], which employs a series of grinding and polishing steps and a final etching with 3% Nital solution (3 ml nitric acid and 97 ml ethanol).

Prior to galvanizing, the pickled, ground and polished samples were treated with flux containing 300gr/l $ZnCl_2.3NH_4Cl$ solution for 2 minutes at 60°C and dried in hot air flow at 125°C.

For galvanizing, the conditioned samples were immersed in the zinc bath for 10 minutes. Following galvanizing, the samples were quenched in water so for sure to examine only the Fe-Zn phases evolved in galvanizing process.

Thickness of the Fe-Zn phases was measured as a distance from η-ξ interface to the steel substrate, excluding the thickness of the outermost (η) phase, which included dross particles from the zinc bath.

Table 1. Chemical composition of the samples.

Sample	C	Si	Mn	P	S	Al
1	0.050	0.010	0.28	0.018	0.013	0.049
2	0.055	0.115	0.34	0.018	0.035	0.054
3	0.050	0.210	0.37	0.017	0.017	0.041
4	0.160	0.320	1.31	0.014	0.013	0.034

RESULTS and DISCUSSION

The conditioned surfaces, and the cross-sections of the subsurface regions are as shown in Figure 1. The surface of the ground samples consist of valleys and ridges shaped by the SiC particles on the grinding papers. Additio-

nally, slightly distorted layers were revealed on the cross-sections of the ground samples, in where the plastically deformed grains extended to the depth of 6 μm from the surface. Neither the pickled nor the polished surfaces obviously revealed any plastically deformed grains on the cross-sections. The pickled surfaces exhibited cavities on the surface, while the polished surfaces gave smooth planes with tiny abrasive traces. The roughness values of the mechanically formed surfaces were found considerably lower than that of pickled surface (Table 2)

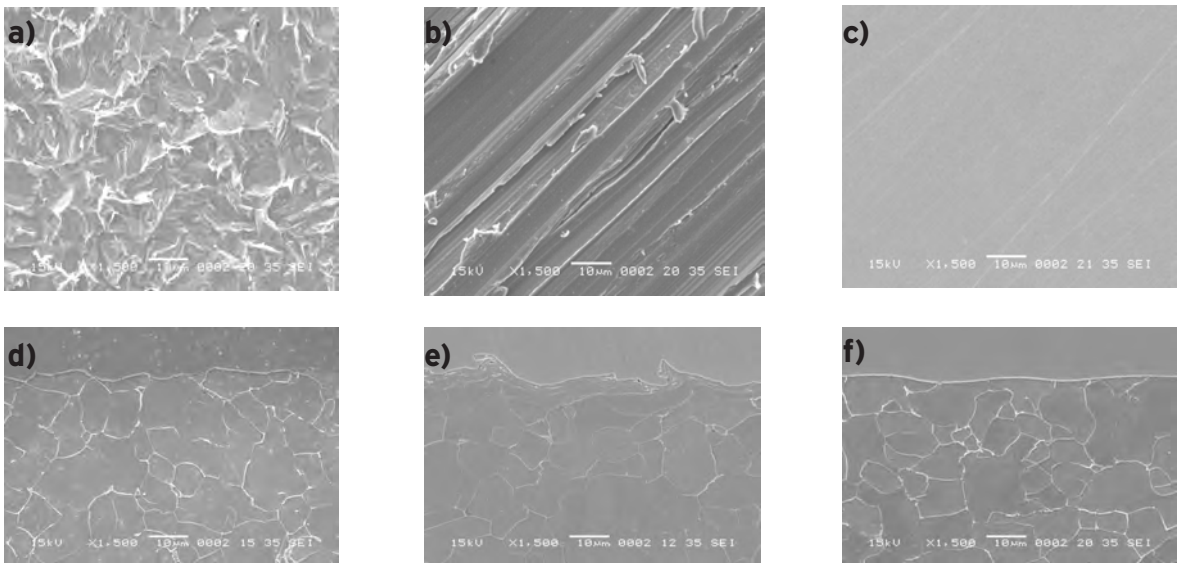

Figure 1. Surface topographies and cross-sections of the conditioned samples through SEM: pickled (a, d), ground (b, e), polished (c, f)

Table 2. Surface roughness of the conditioned samples.

Surface	Surface roughness, Ra (μm)
Pickled	2,21
Ground	0,80
Polished	0,02

Variation of the Fe-Zn alloy layer thickness of the pickled and the polished samples with respect to silicon content brings out the general shape of the Sandelin Curve with a peak at approximately 0.115%Si (Figure 2). Although this behavior agrees with the results of the previous studies [6-8], the ground samples without a peak in the Sandelin range exhibited a different curve than expected.

The pickled low Si containing steels produce a diffusion controlled homogeneous coating structure consisting of the phases of ζ, δ and Γ as expected (Figure 3).

The coating structures on the other pickled samples of higher silicon contents display similar characteristics of the Sandelin Curve.

The polished samples exhibit a significant reactive behavior even on the steel containing 0.010% Si, which has produced stable coatings with other treatments. In the polished sample, δ phase layers become thinner where ζ phase over grows due to the reactive behavior (Figure 4a). It is proposed

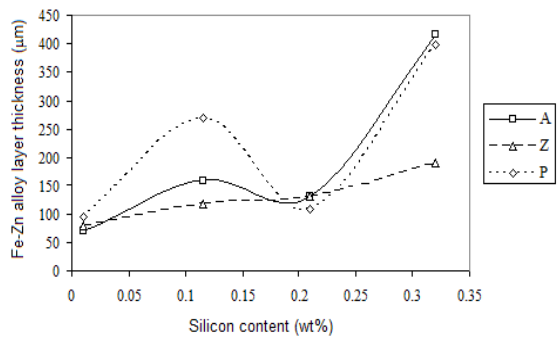

Figure 2. Variation of the Fe-Zn alloy layer thickness with silicon content as a function of the surface treatments: Pickling = A, Grinding = Z, Polishing = P

that this enhanced reactive behavior is due to the exposure of silicon rich substrate layers after removing oxidized top surface layers by grinding and later on polishing. The steel containing 0.115% Si shows a distinguished reactive behavior producing a very thick coating which is mainly composed of large crystals of a well defined ζ and surrounding η phases (Figure 4b).

The grinding produces a thin and compact coating structure on the 0.010% Si containing steel, which is similar to the pickled one (Figure 4c). Compared to the others, the ground sample containing 0.320% Si yields a much thinner coating in this silicon concentration (Figure 4d).

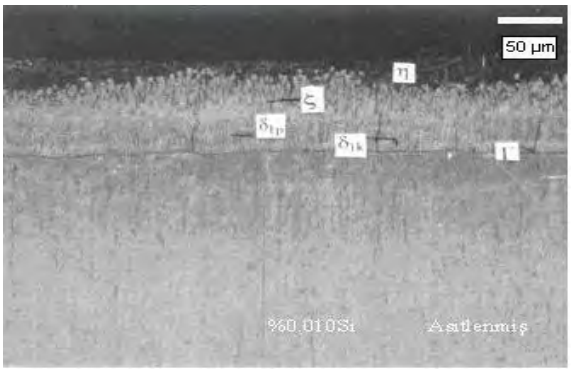

Figure 3. Effect of pickling on the coating structure of the steel containing 0.010 % Si.

It is seen that the surface characteristics developed by 60 grit SiC paper prevent an increase in the thicknesses of the coatings on account of Si content (Figure 5). The coatings generated on the ground samples with the 60 grit SiC paper having 270 µm SiC particles are consistent with those generated with shot blasting which has corundum particles in size of 100-200 µm [7], and grinding which has particles in size of 125-250 µm [8].

The effect of surface topography on the reactivity can be explained by the model proposed by Bablik et al [6] on development of alloy layers on the concave and convex surfaces of silicon free steels. According to this model, the convex surfaces produce scattered alloy layers whereas the concave surfaces favor the growth of iron rich regions producing more compact and continuous layers. Thus, ζ phase crystals on the convex surfaces allow the liquid zinc to penetrate to the ζ-δ interface regions that cause the rapid growth of ζ crystals according to the following reaction:

$$\delta_{solid} + Zn_{liquid} \rightarrow \zeta_{solid} \quad (1)$$

However, in the inward inclined surfaces, the Fe rich compact and continuous layers cause the reactions to be diffusion controlled. This explains the formation of stable coatings in the inward inclined surfaces of the galvanized pipes due to the blocking of zinc transfer and causing the reactions to be more of the diffusion controlled type [14].

In the present study, the pickled and polished samples with different surface topographies cannot produce Fe rich compact and continuous δ phase layers to inhibit the transfer of the liquid zinc in the more reactive regions. However, the samples ground with 60 grit SiC paper yield a characteristic surface topography to form stable Fe rich alloy layers with a dense Fe transfer from the concave surface of the valleys produced by the SiC particles.

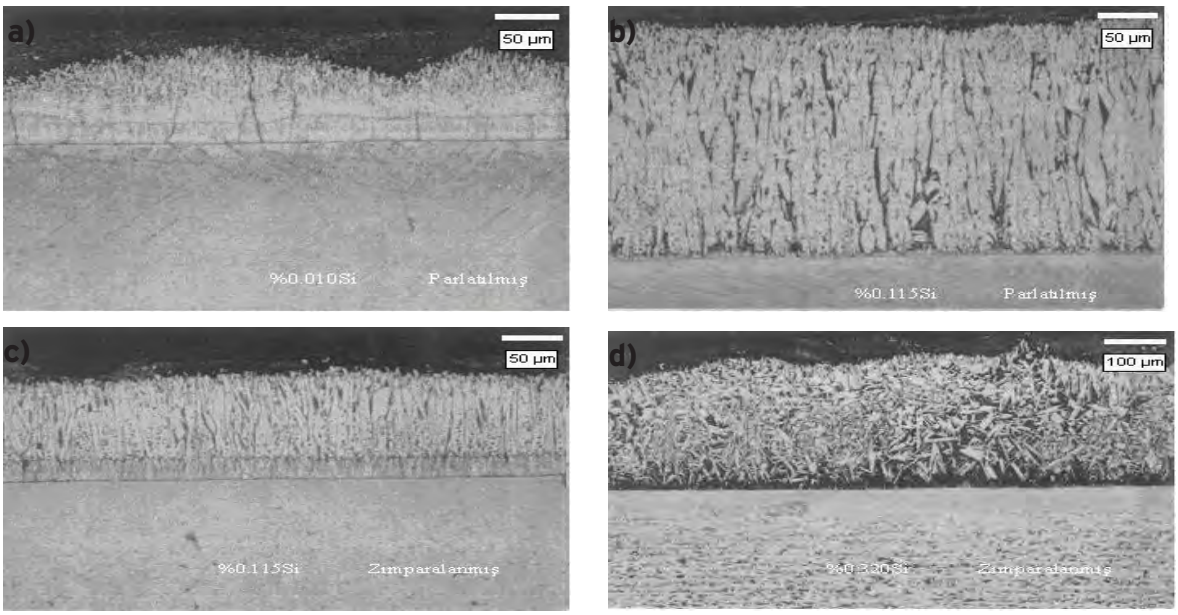

Figure 4. a) Effect of polishing on the coating structure of the steel containing 0.010 % Si. b) Effect of polishing on the coating structure of the steel containing 0.115 % Si. c) Effect of grinding on the coating structure of the steel containing 0.115 % Si. d) Effect of grinding on the coating structure of the steel containing 0.320 % Si.

CONCLUSIONS

Surface topography, i.e. the degree of surface roughness and the surface shape is the main factor controlling the stability of the hot-dip galvanizing coatings.

Therefore, a suitable surface topography for the steel products to be galvanized should be generated and measured with a reliable analytical method prior to galvanizing process. Compared with the previously obtained results, it can be suggested that intermediate roughness and sharp

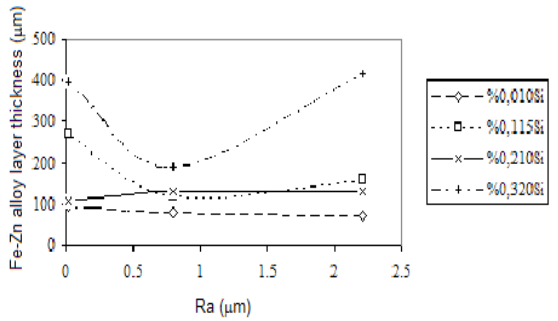

Figure 5. Variation of the Fe-Zn alloy layer thickness with surface roughness (Ra) as a function of silicon content in the ground samples.

asperities generated with abrasive particles having sizes in the range of 100-270µm can produce suitable galvanizing coatings on the steels having silicon contents in the Sandelin range.

REFERENCES

1. Sandelin, R. W. Galvanizing Characteristics of Different Types of Steels, Wire and Wire Products, 15 (1940), 655–676.
2. Horstmann, D. Hot Dip Galvanizing, Proc. 6th Int. Galvanizing Conf., Interlaken, Switzerland, 1961, pp. 319–328.
3. Pelerin, J., Hoffmann H., Leroy, V. The influence of silicon and phosphorous on the commercial galvanization of mild steels, Metall, 35 (9) (1981), 870–873.
4. Guttman, H., Niessen, P. Galvanizing of silicon steels in aluminum containing baths, Proc. Sem. On Galvanizing Silicon-containing Steels, Liege, Belgium, 1975, pp. 198–216.
5. Leroy, V., Emond, C., Cosse, P., Habraken, L. Study of the surface of silicon–killed steels in relation to hot–dip galvanizing, Proc. Sem. on Galvanizing Silicon-containing Steels, Liege, Belgium, 1975, pp. 97–119.
6. Bablik, H., Gotzl, F., Neu, E. Die Rauhigkeit verschiedener vorbehandelter Oberflächen und ihre Bedeutung für das Feuerverzinken. Z. Metalloberfläche, 9 (5) (1955), 69-71 (A).
7. Petter, F. Der Einfluß einer mechanischen OberflächenVorbehandlung durch Strahlen auf das Verzinkungsverhalten siliziumhaltiger Stähle, Z. Metall, 30 (4) (1976), 339-342.
8. Hansel, G. Zum Einflu der Topographie der Stahloberfläche auf die Ausbildung der Legierungsschichten bei der Feuerverzinkung, Z. Metalloberfläche, 38 (8) (1984), 347-351.
9. Heubner, U; Nilmen, F Hot Dip Galvanizing of Silicon Containing Steels: The Problem and Some Attempts at Its Solution, Werkst. Korros., 30 (3) (1979), 169–179.
10. Radtke, S. F. A New Method for Batch Galvanising of Silicon–Containing Steels, Metall, 34 (9) (1980), 865–867.
11. Dreulle, N. Galvanizing with Polygalva zinc alloy, Proc. 12th Int. Conf. on Hot–dip Galvanizing, Paris, France, 1979, pp. 186–191.
12. Allen, C. J., Battiston, L., Mills, R. J. Galvanizing plant trial using nickel–zinc process, CIM Bull., pp. 109–114.
13. Vazquez, A. J. Heat treatment and stabilization of the structure of galvanized coatings, Proc. 12th Int. Conf. on Hot–dip Galvanizing, Paris, France, 1979, pp. 147–155.
14. Vazquez, A. J., Damborenea, J. J. The Sandelin effect and continuously cast steels, Int. J. of Materials and Product Technology, 6 (1991), 175–216.
15. Vazquez, A. J. Galvanizing of silicon steels, reactive zone theory, Metall, 38 (1984), 952–955.
16. Jordan, C. E., Goggins, K. M., Benscoter, A. O., Marder, A. R. Metallographic preparation technique for hot–dip galvanized and galvannealed coatings on steel, Material Characterization, 31 (1993), 107–114.

Hittite Journal of Science and Engineering, 2016, 3 (2)87-90
ISSN NUMBER: 2149-2123
DOI: 10.17350/HJSE19030000036

Classification and Rating of Inclusions in Steel Using an Image Analysis Software

Oktay Elkoca
ArcelorMittal Global R&D Center, East Chicago, IN, USA

ABSTRACT

Inclusions play an important role in the performance of steel products. In this respect, they should be accurately characterized in steels. Developing computer technology and softwares have been allowed to evaluate the inclusion content of a steel products by classifying and rating numerous inclusions in a large number of fields through optical microscope. However, due to the difficulties encountered in classification, it still needs experienced operators' intervention, and advanced tools like SEM-EDS for accurate results.

Keywords: Steel; Inclusion; Inclusion rating; Image analysis; Metallography

Article History:
Received: 2016/09/29
Accepted: 2016/10/26
Online: 2016/12/31

***Correspondence to**: Oktay Elkoca, ArcelorMittal Global R&D Center, 3001 East Columbus Drive, East Chicago, IN 46312-2939, USA*
Tel: +1 (312)7720874
E-Mail: oelkoca@gmail.com

INTRODUCTION

Inclusions are non-metallic particles embedded in steel matrix. The particles usually are compounds such as oxides, sulphides, and silicates, but may be any substance insoluble in the matrix [1]. Sims [2] classified nonmetallic inclusions based on their origin as endogenous and exogenous. The endogenous inclusions are formed by the reactions in liquid metal in steelmaking process and their formation is dictated either by additions to the liquid metal or by changes in solubility during the solidification process. Oxides and sulphides are examples of endogenous non-metallic inclusions in steels. The exogenous inclusions in steels, on the other hand, occur as a result of trapping of slag, refractories, and oxidized metal that the liquid metal comes in contact with during the melting and casting process [2,3].

While inclusions are advantageous for certain applications such as machining and oxide dispersion strengthened steel alloys, under uncontrolled conditions they can be deleterious to the performance of a steel product [4]. Their origin, type, size, shape, number, and distribution may influence almost all properties of a steel such as formability, machinability, weldability, fatigue, fracture, creep, corrosion, and toughness [4,5]. Therefore, inclusions should be identified, classified, and rated prior to manufacturing processes of a steel product. Various techniques are available to monitor and characterize the inclusion content of a steel. Microscopic technique based on viewing a metallographically prepared sample through an optical microscope is still very valuable and prevailing one among all known methods. In this method, the inclusions in a polished sample are observed through an optical microscope and classified and rated according to a standard method. Standard reference charts depicting a series of typical inclusion configurations (size, type, and number) in those standards have been created for direct comparison with the microscopic field of view [6]. Therefore, rating practically can be done in comparison with the standard charts such as ASTM E45 [7]. In these charts inclusions are assigned to a category based on similarities in morphology, i.e. by shape, size, concentration, and distribution.

Inclusions are classified into four categories called as type based on their morphology. Each of them is classified into two subcategories based on their width or diameter. Although the categories contain chemical names that imply knowledge of their chemical content, the ratings are strictly based on morphology. In ASTM E45, the four categories, or types, are partitioned into severity levels based on the number or the length of the particles present in a 0.50 mm^2 field of view (Figure 1).

A-type and C-type inclusions are very similar in size and shape. Therefore, they are distinguished based on their color when viewed under the brightfield illumination of an optical microscope, A-type as light gray and C-type C as black. B-type inclusions consist of at least three of round or angular oxide particles with

aspect ratios less than 2 that are aligned nearly parallel to the deformation axis. D-type inclusions are globular in shape.

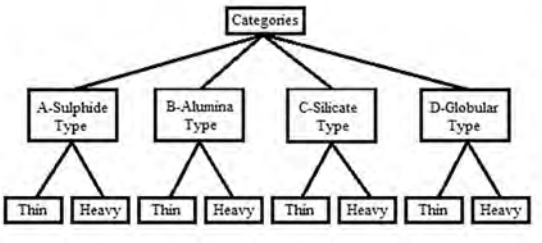

Figure 1. Classification of inclusions according to ASTM E45 [7].

As mentioned above, a common method for the analysis of inclusions is the comparison of the microscopic fields with reference charts. Manual method is rather time consuming, thus restricted with limited fields, thanks to the image analysis softwares a large number of inclusions in numerous fields can be rapidly classified and rated according to their morphological differences through optical microscope [8]. However, due to the difficulties in distinguishing sulphide, silicate, and oxide inclusions it still needs experienced operators' intervention, and advanced tools like scanning electron microscope (SEM) equipped with energy dispersive spectrometry (EDS) analysis for accurate results.

MATERIAL AND METHODS

A sample was taken from a hot rolled S275 JRC steel sheet in 3.5 mm thickness, which is suitable for wheel manufacturing. In wheel steels, elongated inclusions have a deleterious effect on the performance of rim forming and electrical resistance welding, therefore, the sulphide and alumina type inclusions are principally modified by a Ca-Si treatment in steelmaking process. During the Ca-Si treatment, alumina/silicate type inclusions are converted to molten calcium aluminates/silicates, which are globular in shape because of the surface tension effect at liquid stage, and thus become harmless. The change in inclusion composition and shape is known as the inclusion morphology control. Following steelmaking process, cast and solidified metal is hot rolled into final sheet thickness.

The sample was mounted in bakalite so as to expose the cross-sections parallel to rolling direction, ground with 180, 240, 320, 400, 600, and 1000 grit SiC papers, and polished with 9, 6, 3, and 1 µm diamond pastes on napless polishing cloths. Subsequently it was washed, rinsed with ethyl alcohol, and dried with blown air.

Inclusion content of the sample was viewed by Nikon Epiphot 200 optical microscope (OM) at 100x magnification, and the detected inclusions were analyzed by Jeol 5600 JSM scanning electron microscope (SEM) equipped with Oxford energy dispersive spectroscope (EDS). Clemex Inclusion Rating (CIR) software integrated with the optical microscope was used to discriminate, categorize, measure and rate the inclusions found in the sample.

The total analysis area was 376.48 mm^2. Inclusions were classified into four types and categorized into thin and heavy series as shown in Figure 1. The results were expressed according to ASTM E45 Method A [7].

RESULTS AND DISCUSSION

The first step for the automated inclusion rating system is to adjust the light of optical microscope and to verify the threshold. According to the gray level, the threshold defines whether it is a sulfide or an oxide (Figure 2).

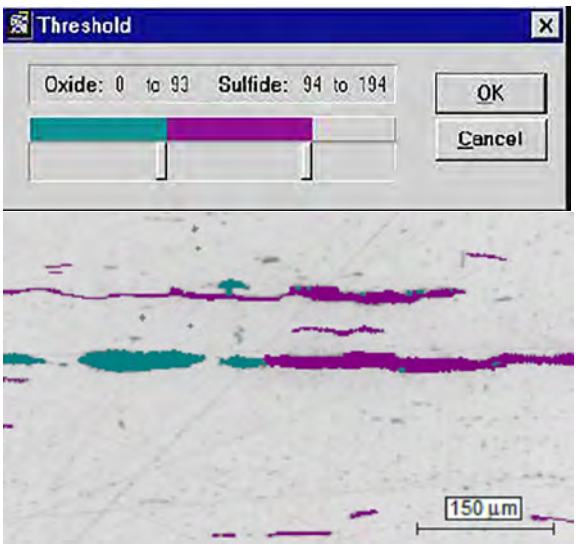

Figure 2. According to defined gray level, inclusions are detected as a sulfide or an oxide.

During thresholding, difficulties were encountered in discriminating the thin sulphide, silicate, and oxide type inclusions since thin B and D-type inclusions were often confused with thin A-type inclusions (Figure 3a-c).

SEM-EDS analysis was performed on the selected inclusions to prevent any confusion. In this way, many thin inclusions previously identified as B-type based on the morphological appearance through optical microscope were corrected as A-type with the aid of Mn and S peaks (constituents of MnS) in the SEM-EDS spectrum (Figure 3b).

Additionally, the inclusions previously identified as globular oxides were revealed as modified Ca-Al-O spinel inclusions based on their SEM-EDS analysis (Figure 3d).

Following the results of SEM-EDS analysis, threshold levels in Clemex CIR software were redefined and the incorrectly identified inclusions were converted to true ones. As shown in Figure 4, the squares of a specific color indicate the worst fields (thin and heavy) for each category.

microscopic fields, whereby large amount of steel products could be analyzed in terms of inclusion content. However, due to the difficulties encountered in classification it still needs experienced operators' intervention, and advanced tools like SEM-EDS for accurate results.

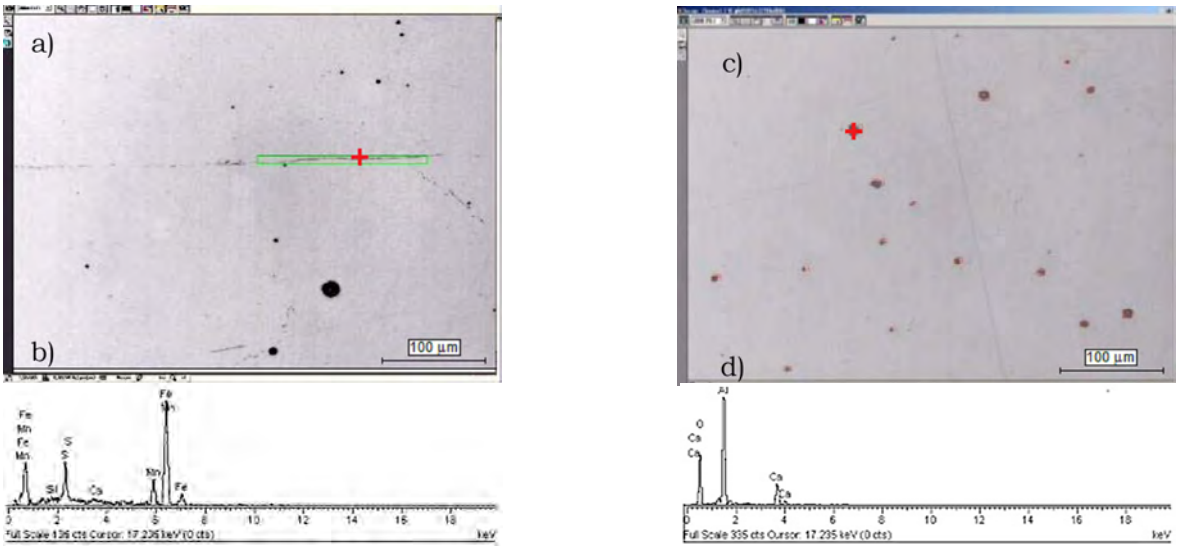

Figure 3 (a) elongated and (c) globular inclusions through optical microscope, and (b) and (d) their SEM-EDS analysis at red crosses "+" in micrographs respectively.

To validate the results, the detected inclusions in the worst fields were reviewed. If a dust residue or polishing scratch remaining from the sample preparation process was detected as an inclusion, it was removed from the results. The results were expressed according to ASTM E45 Method A (Table 1).

Table 1. Clemex CIR report

Sample ID	Width (mm)	Height (mm)	Area (mm^2)	Calibration	Magnification
Sample 1	14.71	3.02	67.76	0.383	200x

Heat 1 – ASTM E45-97A

Sample ID	Thin	Heavy	Thin	Heavy	Thin	Heavy	Thin	Heavy
Sample 1	2.00	0.50	0.75	0.00	0.00	0.00	2.25	0.75

CONCLUSION

It is well established that inclusions play an important role in the performance of steel products, depending on their type, size, shape, and distribution. In this respect, they should be accurately characterized in steels. Thanks to rapidly developing computer software technology, it allows inclusions to be evaluated according to their type, size, shape, and distribution in a steel by classifying and rating of numerous inclusions in a large number of

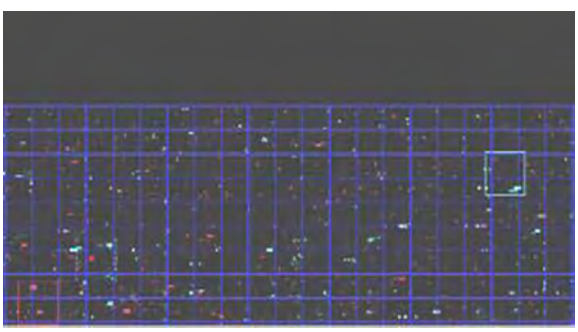

Figure 4. Total analysis area.

REFERENCES

1. Metallography and Microstructure, Metals Handbook, Vol. 9, Ninth Ed., ASM (1985) p. 9.
2. Sims, C. E. Transactions of the Metallurgical Society of AIME, 215 (1959) 367–393.
3. Kissling, R. Non–Metallic Inclusions in Steels, The Institute of Metals, London, (1978).
4. Rungta, R., Skidmore,A. J. and Buchheit, R. D. Inclusions: Advantages, Disadvantages, and The Technological Trends, Ed. by R. Rungta, World Materials Congress, Chicago, Illinois, USA, Sept. 1988, ASM International, pp. 1–19.
5. Gladman, T., Holmes, B. and McIvor, I. D. The Effect of Second Phase Particles on the Mechanical Properties of Steel, Iron and Steel Institute Special Report 145, London, (1971), pp. 68-78.
6. SS 111116, Steel–Method for Estimation of the Content of Non–metallic Inclusions–Microscopic Methods–Jernkontoret's Inclusion Chart II for the Assesment of

Non–metallic Inclusion, Swedish Institute for Standards, Stockholm, Sweden (1987).
7. ASTM E45–13, Standard Test Methods for Determining the Inclusion Content of Steel, ASTM, Philadelphia, PA, USA, (2013).
8. Gladman, T. Quantitative Metallography: Recent Experience with Automatic Image analysis, Clean steels 3, Balatonfured, Hungary, (1986) 50.

Hittite Journal of Science and Engineering, 2016, 3 (2) 91-97
ISSN NUMBER: 2149-2123
DOI: 10.17350/HJSE19030000037

Validation of HPLC Method for the Determination of 5-hydroxymethylfurfural in Pestil, Köme, Jam, Marmalade And Pekmez

Cemalettin Baltacı and Zeynep Akşit
Gumushane University, Department of Food Engineering, Gumushane, TURKEY

ABSTRACT

This study represents a high performance liquid chromatography (HPLC) method for the detection of 5-hydroxymethylfurfural in pestil, köme, jam and pekmez samples. The linearity, selectivity, decision limit, detection capability, detection limit, quantification limit, precision, recovery, ruggedness and measurement uncertainty of the method were determined. The developed method, simple and accurate, showed good recovery values (97-108%). The accuracy of the method expressed with the relative standard deviation was below 6%. The detection limit and quantification limit were 0.03 mg/kg and 0.10 mg/kg, respectively. HMF levels in pestil, köme, jam, marmalade and pekmez samples were determined using the validated method.

Article History:
Received: 2016/10/15
Accepted: 2016/12/21
Online: 2016/12/31

***Correspondence to**: Cemalettin. Baltacı,*
Department of Food Engineering,
Gumushane University, 29100
Gumushane, TURKEY
Tel: +90 (456) 2331291/3223
Fax: +90 (456) 2331292
E-Mail: cbaltaci11@gmail.com

Keywords:
HMF; Method validation; Pestil; Köme; Jam; Marmalade and Pekmez.

INTRODUCTION

5-Hydroxymethylfurfurol (HMF) is a furanic compound formed under acidic conditions by the Maillard reaction or sugar dehydration [1]. Maillard reaction is a non-enzymatic browning reaction, occurs when foods including reducing sugars and amino acids are heated. HMF is an intermediate product of this reaction. Moreover, HMF formation takes place during hexoses dehydration at lower pH (< 5) via enolisation, for which the presence of amino acid groups is not needed [2].

HMF and its derivatives have been reported to show toxic properties such as cytotoxic, genotoxic, nephrotoxic, mutagenic and cancerogenic. The presence of HMF in foods has gained interest due to the toxicological concerns about HMF. Although further studies have revealed that HMF does not exhibit a crucial health risk, it has been a matter of debate [3].

Although HMF is nearly absent in untreated foods, it occurs in processed foods containing carbohydrates such as bread, biscuits, jam, marmalade, honey and fruit juice [4, 5, 6]. HMF amount tends to increase during heat treatment and storage. Therefore, the determination of HMF content can be used to evaluate the effects of food processing industry and storage conditions on the quality of food products [7, 2]. HMF has been used to evaluate the sensorial properties of food products. The changes in the color, flavor and taste of food products during processing and storage are related to the HMF content. Hence it is recognized as an indicator of improper processing and storage conditions [8, 9]. The Turkish Standards [10, 11] state a maximum HMF level of 50 mg/kg in pestil and köme and jam [12]. The established maximum HMF levels are 75 mg/kg, and 100 mg/kg for liquid pekmez, and solid pekmez in accordance with [13].

In the past, a great number of the methods developed for the detection of HMF in foodstuffs were based on spectrophotometric techniques [14, 15]. Although spectrophotometric methods are fast, their sensitivity and specificity are low. Chromatographic methods have been used and developed to detect HMF compounds in food products. UV detection of High performance liquid chromatography (HPLC) is mostly used method used for the determination of HMF in foodstuffs. Accuracy and sensitivity of the

HPLC method are better than that of spectrophotometric methods. Gas chromatography (GC)-mass spectrometry (MS) analysis has been proposed for HMF determination as well [5].

The methods for the determination of HMF have been developed for primarily honey samples. Reliable, sensitive and rapid methods are required to determine HMF in different matrices because of the potential toxic effects of HMF and quality control of food products. The goal of this investigation was to develop and validate a sensitive, reliable and rapid method for the detection of HMF in pestil, köme, jam and pekmez. The proposed method was validated with respect to decision limit, detection limit, quantification limit, selectivity, linearity, precision, recovery and ruggedness. Practising of the developed procedure to real samples was carried out as well.

METHODS

Samples

Pestil, köme, jam and pekmez samples were collected from a local market in Trabzon and Gümüşhane. All samples were stored at 4°C until analysis.

Chemicals

Analytical chemicals and HPLC grade solvents were obtained from Merck (Darmstadt, Germany). HMF standard (99%) was bought from Sigma-Aldrich (St. Lois, MO, USA). Membrane filters (45 µm) were supplied by Millipore (Bedford, MA, USA).

Sample preparation

Specimens were homogenized by an Ultra Turrax mixer (IKA, Germany). 5 g of the sample was dissolved with 25 mL water in a 100 mL flask, 0.5 mL of Carrez I solution and 0.5 mL of Carrez II solution were added, later water was added to the mark. The sample solutions were filtered through 45 µm membrane filters. 100 µL of the sample solution was injected to the HPLC-UV system.

Equipment

Quantitative analysis was carried out using an HLPC-UV system (Agilent 1100 series, USA). The separation of HMF was carried on a C_{18} column, 250 mm×4.6 mm, 5 µm (Nucleosil, USA). The mobile phase, water-methanol (90:10 v/v), was at a flow rate of 1 mL/min, wavelength at 285 nm.

Method validation

The HPLC method based the method for HMF detection in honey samples was validated and applied to pestil, köme, jam, marmalade and pekmez samples of the International Honey Commission [16]. The sensitivity, linearity, decision limit, detection capability, detection limit, quantification limit, precision, recovery, ruggedness and measurement obscure of the method were ascertained to validate the method for HMF analysis in the studied samples.

Statistical analysis

Microsoft Excel 2007 (Microsoft Corp.,Redmond, WA, USA) was used for data processing. Outliers were checked and removed based on the Cochran test and Grubbs test. Linear regression model was performed using the least squares approach.

RESULTS AND DISCUSSION

Validation

Single laboratory validation was performed according to Regulation 2004/882/EC. Performance characteristics of validated method determined were selectivity, linearity, detection and quantification limits, decision limit, precision, recovery, ruggedness and measurement obscure.

Selectivity

The selectivity of a method describes the ability to detect. Before beginning the validation process, the selectivity of method should be checked against naturally occurring substances. Representative blank samples (*n=20*) were analyzed and their chromatograms were compared with the chromatogram of the spiked samples. As can be seen from Fig. 1, no interference observed at the retention time of HMF indicated that the proposed method was selective for HMF analysis.

Linearity

A calibration curve was obtained by plotting the peak areas of standard solutions which were the three series of five different concentrations. The calibration curve equation described as y = a (x) + b, where y is the peak area of standard solution in terms of absorbance, x is the concentration of standard solution in mg/kg. Good linearity was obtained in the studied range, with R^2 value higher than 0.999 (Table 1). Preparation and mass concentration of calibration used for HPLC-UV and some analytical parameters from the developed method.

Limit of detection and limit of quantification

The Limit of quantification (LOQ), lowest content of the analyte which can be measured with reasonable statistical certainty. If both accuracy and precision are

Table 1. Preparation and mass concentration of calibration used for HPLC-UV and some analytical parameters

Main stock solution (mg L⁻¹)	*Volumes Vi (µL) of main stock solution diluted [b] to 25 mL to be used as calibrator*					*Calibration concentration i (mg L⁻¹)*				
1000 [a]	*1 st*	*2 nd*	*3 nd*	*4 th*	*5 th*	*1 st*	*2 nd*	*3 nd*	*4 th*	*5 th*
	25	*50*	*100*	*200*	*300*	*1.0*	*2.0*	*4.0*	*8.0*	*12.0*
Calibration range (mg/kg)								*1.0-12.0*		
Calibration equation								*y[c] = 7036x – 0.3*		
Regression coefficient								*0.999*		

[a] HMF standard was used 99% purified

[b] Dilution of V *i* of the stock solution to 25 mL with purified water, to produce calibrations *i*

[c] *y* is the peak area of standard solution expressed in absorbance, *x* is the concentration of standard solution expressed in mg/kg.

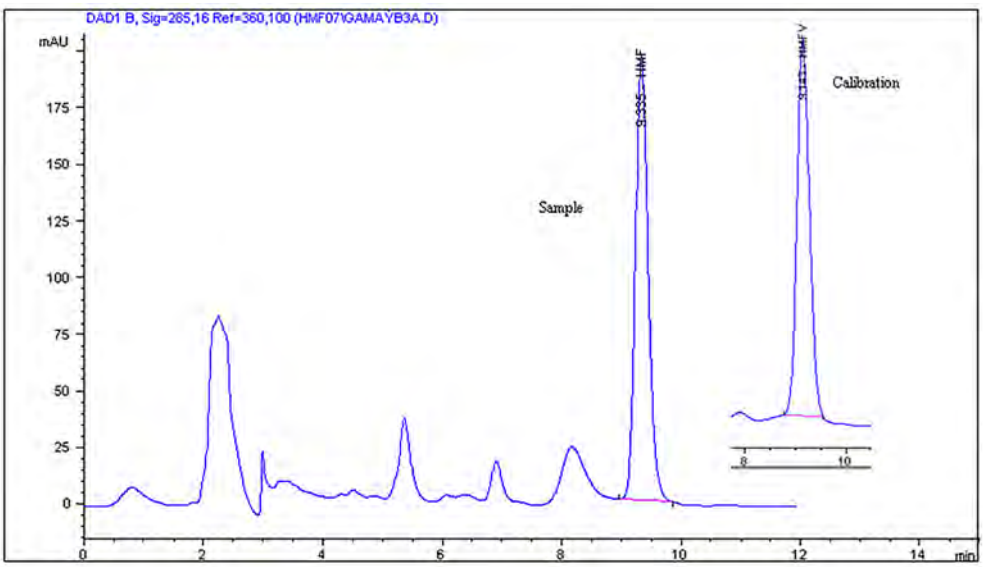

Figure 1. A) representative blank sample B) spiked specimen

constant over a concentration rangearound the limit of detection, then the limit of quantification is numerically equal to 10 times the standard deviation of the mean of 0.2 mg/kg. The limit of detection (LOD), expressed as the concentration, or the quantity, is derived from the smallest measure, that can be detected with reasonable certainty for a given analytical procedure. the limit of quantification is numerically equal to 3 times the standard deviation of the mean of 0.2 mg/kg. LOD and LOQ were determined by analyzing ten samples spiked with HMF (0.2 mg/kg) in accordance with Analytical Detection Limit Guidance [17]. In order to estimation of LOD, the standard deviation of the response (*s*) was multiplied by the Student's *t*-test value for ten replicates and nine degrees of freedom. The forecasted LOD values were confirmed according to the guidance [17] as well.

Table 2. The decision limit (CCα) and detection capability (CCβ) values of the method calculated at the MRL (n=20) for the HMF

Matrix	*Added (mg/kg)*	*Measured ± S.D. (mg/kg)*	*Error α (1.64 x S.D.)*	*CC_α (mg/kg)*	*Added (mg/kg)*	*Measured ± S.D. (mg/kg)*	*Error β (1.64 x S.D.)*	*CC_β (mg/kg)*
Jam	*0.03[a]*	*0.04 ± 0.02*	*0.03*	*0.06*	*0.06*	*0.05 ± 0.01*	*0.02*	*0.08*
	50.00[b]	*50.50 ± 0.88*	*1.44*	*51.44*	*51.44*	*50.65 ± 0.62*	*1.02*	*52.46*
Liquid pekmez	*0.03[a]*	*0.03 ±0.01*	*0.02*	*0.05*	*0.05*	*0.04 ±0.01*	*0.02*	*0.08*
	75.00[b]	*74.50 ± 0.66*	*1.08*	*76.08*	*76.08*	*75.50 ± 0.79*	*1.30*	*77.38*
Solid pekmez	*0.03[a]*	*0.04 ± 0.02*	*0.03*	*0.06*	*0.06*	*0.04 ± 0.02*	*0.03*	*0.09*
	100.00[b]	*99.50 ± 1.06*	*1.74*	*101.74*	*101.74*	*100.50 ± 0.98*	*1.61*	*103.35*
Kome	*0.03[a]*	*0.028 ± 0.01*	*0.02*	*0.05*	*0.05*	*0.048 ± 0.01*	*0.02*	*0.07*
	50.00[b]	*49.80 ± 0.74*	*1.21*	*51.21*	*51.21*	*50.80 ± 0.67*	*1.10*	*52.31*
Pestil	*0.03[a]*	*0.028 ± 0.01*	*0.02*	*0.05*	*0.05*	*0.045 ± 0.02*	*0.10*	*0.07*
	50.00[b]	*49.1 ± 0.91*	*1.49*	*51.49*	*51.49*	*51.20 ± 0.72*	*1.18*	*52.67*

[a] limit of quantification, [b] maximum permitted limit

Table 3. The repeatability and within-laboratory reproducibility of the method, expressed with the standard deviation and the relative standard deviation.

	Intra-day (n=6)					Inter-day (n=6)			
Analyte	Fortification level mg/kg	Determined level mg/kg	S_r mg/kg	Precision RSD_r (%)	0.66 X Horwitz value (%)	Determined level mg/kg	S_R mg/kg	Precision RSD_R (%)	Horwitz value (%)
Jam	25.00[a]	25.42	1.05	4.11	6.51	24.54	1.56	6.36	9.86
	50.00[b]	48.93	1.69	3.45	5.86	49.73	1.17	2.35	8.88
	75.00[c]	74.35	1.24	1.67	5.51	74.32	1.15	1.55	8.35
Liquid pekmez	37,50[a]	36.94	1.19	3.22	6.12	37.91	1.22	3.22	9.27
	75.00[b]	74.80	0.88	1.18	5.51	74.97	1.13	1.51	8.35
	112.50[c]	111.97	1.08	0.97	5.19	112.24	1.69	1.50	7.86
Solid Pekmez	50.00[a]	49.63	1.39	2.80	5.86	49.86	1.17	2.35	8.88
	100.00[b]	99.24	1.26	1.27	5.28	99.84	1.18	1.31	8.00
	150.00[c]	148.30	0.97	0.65	4.97	149.85	1.72	1.15	7.53
Kome	25.00[a]	24.02	0.93	3.87	6.51	24.56	1.21	4.93	9.86
	50.00[b]	48.96	1.07	2.18	5.86	48.87	1.25	2.57	8.88
	75.00[c]	74.82	1.58	2.11	5.51	74.94	1.89	2.52	8.35
Pestil	25.00[a]	25.96	0.93	3.58	6.51	23.59	1.21	5.13	9.86
	50.00[b]	51.23	1.07	2.08	5.86	50.80	1.25	2.46	8.88
	75.00[c]	74.15	1.58	2.13	5.51	73.90	1.89	2.56	8.35

[a]0.5x MRL, [b]MRL, [c]1.5xMRL

LOQ values were evaluated as ten times of the standard deviation. The determined LOD and LOQ values for HMF substances were 0.01 mg/kg and 0.03 mg/kg, respectively.

Decision limit and detection capability

Two new performance characteristic of decision limit (CC_α) and detection capability (CC_β), are submitted by Regulation 2002/657/EC. CC_α refers to the above the limit of samples concluded as non-compliant($\alpha = 5\ \%$) and CC_β refers the lowest content of the substances that may detected, identified and/or quantified in a sample ($\beta = 5\ \%$). The CC_α and CC_β values were determined to analyze 20 blank samples fortified with HMF at the maximum permitted limit (MRL) regulated by Turkish Food Codex and Turkish Standards. Estimated CCα and CC_β values according to the following equations of the method were calculated in Table 2.

CC_α = the concentration at MRL+ 1.64 *x* the standard deviation of the fortified samples [1] $CC_\beta = CC_\alpha + 1.64$ *x* the standard deviation of the fortified samples [2]

Precision

Precision was determined by analyzing twelve empty specimen spiked with HMF standard solution at the concentrations of 0.5, 1 and 1.5 times MRL. For the precision test, specimens were conducted in ten replicates and analyses were fulfilled by the same operator in one day. To determine the intermediate precision, samples (ten replicates) were analyzed by two different operators in three days over a month. The results for the repeatability expressed with the standard deviation (S_r) and the relative standard deviation (RSD_r) and the results for the within-laboratory reproducibility expressed with the standard deviation (S_R) and the relative standard deviation (RSD_R) are presented in Table 3. Both RSD values at the three concentration levels were found to be lower than the reference values (Table 3) calculated from the Horwitz equation.

Recovery

Recovery is a measure of the accuracy. The reclamation of the method was determined instead of trueness since reference material cannot be available. Three different concentrations of the HMF standard were added to samples, 0.5, 1 and 1.5 times MRL. (25, 50, and 75mg/kg for köme, jam and pestil; 37.5, 75, and 112.5 mg/kg for jam; 50, 100, and 150 mg/kg for solid pekmez; 37.5, 75, and 112.5 mg/kg for liquid pekmez) were analyzed to determine the recovery values. The recovery values obtained ranged from 97.18% to 107.68% (Table 4),

Table 4. The recovery values of spiked samples at three different concentrations (n=6).

Sample	Spiked level (mg/kg)	Mean Determined Level (mg/kg)	Mean Recovery (%)	S (mg/kg)	RSD (%)
Jam	25.00[a]	24.60	98.40	0.44	1.79
	50.00[b]	49.11	98.22	0.58	1.18
	75.00[c]	73.62	98.16	1.05	1.43
Liquid Pekmez	37.50[a]	37.14	98.80	0.46	1.24
	75.00[b]	76.33	99.04	0.53	0.69
	112.50[c]	110.65	98.36	1.47	1.33
Solid Pekmez	50.00[a]	49.57	99.14	0.68	1.37
	100.00[b]	99.69	99.69	0.96	0.96
	150.00[c]	148.44	98.96	0.85	0.86
Kome	25.00[a]	26.92	107.68	0.64	2.38
	50.00[b]	49.53	99.06	1.52	3.06
	75.00[c]	74.12	100.2	0.93	1.25
Pestil	25.00[a]	23.92	98.83	0.64	2.68
	50.00[b]	48.59	97.18	1.52	3.13
	75.00[c]	74.54	99.39	0.93	1.25

[a]0.5x MRL, [b]MRL, [c]1.5xMRL

showing good recovery values for the proposed method.

Ruggedness

Ruggedness of the method was evaluated by Youden test. Eight experiments were performed to evaluate the seven selected factors: extraction solution, specimen matrix, specimen preparation, analyst, column temperature, HPLC column and mobile phase. The standard deviation of impacts was evaluated according the following equation.

$$SD = 2\sum\left(\frac{E_i^2}{n}\right) \quad [3]$$

Where E_i is each of the calculated effect, and n is the number of parameters.

The influence of the factors on method performance has to be checked applying the *t*-test [18]. The experimental *t*-values for the factors were calculated according to the formula given below:

$$t = \frac{E_i.\sqrt{n}}{SD.\sqrt{2}} \quad [4]$$

The experimental *t*-values (Table 5) were found to be lower than the critical value (t_{crit} = 2.45 at 95% confidence level), indicating that the method is sufficiently rugged against the changes in the procedure. As a result, the proposed useful way was validated for the determination of HMF in pestil, köme, jam and pekmez.

Measurement uncertainty

The validation data was used to calculate the measurement uncertainty [19]. Volume, mass, calibration curve, reproducibility and repeatability of the method, preparation of standard, accuracy and reproducibility of the equipment were selected as sources of uncertainty budget. The relative expanded uncertainty of measurement was reckoned using a coverage factor k=2, corresponding approximately 95% confidence level. Expanded uncertainty value was 9.1% for HMF in foodstuffs.

Application of the method to real samples

Pestil, köme, jam, and pekmez samples were analyzed using the validated method. Pekmez, a traditional food product in Turkey, is concentrated grape or mulberry juice formed by boiling without the addition of sugar and another ingredients [20]. Pestil and köme in Turkey are made from both fruit juice and concentrated fruit juice [21]. The HMF content of pekmez samples (solid *n:25 and liquid*) was found to be ranged from 1.44 to 66.30 mg/kg, complying with the values set by the Turkish Codex [13]. Available data on the HMF content of pekmez is limited. Our results seemed to be higher

Table 5. Experimental design for the ruggedness study (50.0 mg/kg)

Factor	Original parameters (A-G)	Changed parameter (a-g)
A. Extraction solvent	Water	a. Water / Methanol (90/10 v/v)
B. Sample matrix	Pestil, köme, jam, marmalade and pekmez	b. Blank sample
C. Sample preparation	Addition of carrez I and II	c. No addition of carrez I and II
D. Analyst	Analysts 1	d. Analysts 2
E. Column temperature	22 oC (Room temperature)	e. 27 oC
F. LC column	250 mm´4.6 mm, 5 mm C18	f. 250x4.6 mm, 5µm, ODS 2
G. Mobile phase	Water/ methanol (90/10 v/v)	g. Water/methanol (80/20 v/v)

+a	-b	1	2	3	4	5	6	7	8	Ei	Ei*Ei	t
A	a	49.3	48.6	49.2	47.9	-48.1	-48.2	-48.9	-51.2	-0.350	0.12250	0.21
B	b	49.3	48.6	-49.2	-47.9	48.1	48.2	-48.9	-51.2	-0.750	0.56250	0.98
C	c	49.3	-48.6	49.2	-47.9	48.1	-48.2	48.9	-51.2	-0.100	0.01000	0.02
D	d	49.3	48.6	-49.2	-47.9	-48.1	-48.2	48.9	51.2	1.150	1.32250	2.32
E	e	49.3	-48.6	49.2	-47.9	-48.1	48.2	-48.9	51.2	1.100	1.21000	2.12
F	f	49.3	-48.6	-49.2	47.9	48.1	-48.2	-48.9	51.2	0.400	0.02286	0.04
G	g	49.3	-48.6	-49.2	47.9	-48.1	48.2	48.9	-51.2	-0.700	0.49000	0.86
										SD	1.06867	

[a] Original parameters, [b] Changed parameters, E_i is each of the calculated effects.

compared to the literature[22]. The HMF content of jam samples (*n:25*) varied from 12 to 22 mg/kg. These values were in agreement with data found in the literature [2, 8]. The HMF content of Pestil and köme (solid *n:25 and liquid*) was found to be ranged from 1.3 to 45.3 mg/kg. These values were in agreement with data found in the literature [23].

CONCLUSIONS

An method for the extraction of 5-HMF from food samples and its subsequent determination using HPLC with UV detection was validated according to Regulation 2004/882/EC. The validated method provides accurate results and offers quick and economic procedure. The conclusion can be derived that recommended method is suitable for the detection of HMF in the food matrices such as köme, pestil, jam, and pekmez.

REFERENCES

1. Capuano,E. And Fogliano,V. Acrylamide and 5–hydroxymethyl–furfural (HMF), A revieew of metobolosim, toxity, occurrence in food and mitiagtion strategies. LWT–Food Sci. Technol., Vol. 44 Pages 793–810. 2011.
2. Teixido, E., Nunez, O., Santos, FJ., Galceren, MT. 5–Hydroxymethylfurfural content in foodstuffs determined by micellar electrokinetic chromatography. Food Chem Vol. 126, Pages 1192, 2011.
3. Spano, N., Casula, L., Panzanelli, A., Pilo, MI., Piu, PC, Scanu, R., Tapparo, A., Sanna, G. A RP–HPLC determination of 5–hydroxymethylfurfural in honey – The case of strawberry tree honey. Talanta Vol: 68 Issue: 4 Pages: 1390–1395, 2006.
4. Ameur LA, Rega B, Giampaoli P, Trystram G, Birlouez–Aragon I. The fate of furfurals and other volatile markers during the baking process of a model cookie. Food Chem Vol.:111, Issue 3, Pages 758–763758, 2008.
5. Gaspar, EMSM., Lopes, JF. Simple gas chromatographic method for furfural analysis. J Chromatogr A, Vol. 1216, Issue 14, Pages 2762–2767, 2009.
6. Rada–Mendoza, M., Sanz, ML., Olano, A., Villamiel, M. Formation of hydroxymethylfurfural and furosine during the storage of jams and fruit–based infant foods. Food Chem Vol.85, Issue , Pages 605–609, 2004.
7. Kus, S., Gogus, F., Eren S., Hydroxymethyl furfural content of concentrated food products. Int J Food Properties Vol.8, Issue 2, Pages 367–375, 2005.
8. Rada–Mendoza, M., Olano, A., Villamiel, M. Determination of hydroxymethylfurfural in commercial jams and in fruit–based infant foods. Food Chemistry Vol.79, Issue 4, Pages 513–516, 2002.
9. Teixido, E., Moyano, E., Santos, FJ., Galceran, MT. Liquid chromatography multi–stage mass spectrometry for the analysis of 5–hydroxymethylfurfural in foods. J Chromatographia A Vol.1185, Issue 1, Pages 102–108, 2008.
10. TS 12677, Spreaded dried mullberry, Turkısh Standard, 24.10.2000.
11. TS 12477, Pekmez mass with decorticated fruits, Turkısh Standard, 17.11.2015

12. TS 3958, Sour Cherry Jam, Turkısh Standard, 09.03.2010.
13. Regulation on Turkish Food Codex, 29 December 2011 – 28157
14. Winkler, O.: Beitrag zum Nachweis und zur Bestimmung von Oxymethylfurfural in Honigund Kunsthonig. Z. Lebensm. Forsch. 102, 160–167, 1955.
15. White, J., Spectrophotometric Method for Hydroxymethylfurfural in Honey. J. AOAC, 509, 1979.
16. Harmonısed Methods Of The Internatıonal Honey Commıssıon http://www.bee-hexagon.net/en/network.htm.
17. Analytical Detection Limit Guidance & Laboratory Guide for Determining Method Detection Limits, Wisconsin Department of Natural Resources Laboratory Certification Program, April 1996.
18. Bratinova S., Raffael B., Simoneau C. Guidelines for performance criteria and validation procedures of Analytical methods used in controls of food contact Materials. EUR 24105 EN – 1st edition 2009
19. EURACHEM / CITAC Guide CG 4 Quantifying Uncertainty in Analytical Measurement Third Edition. www.eurachem.org.
20. Kaya, A., Belibaglı, KB. Rheology of solid Gaziantep Pekmez. J Food Eng vol.54, Issue 3, Pages 221–226, 2002.
21. Ercişli, S., Orhan, E. Chemical composition of white (***Morusalba***), red (***Morusrubra***) and black (***Morusnigra***) mulberry fruits. Food Chem 103: 1380–1384, 2007.
22. Sengul, M., Ertugay, MF., Sengul, M. Rheological, physical and chemical characteristics of mulberry pekmez. Food Control, Vol. 16, Issue 1, Pages 73–76, 2005.
23. Yildiz, O. Physicochemical and sensory properties of mulberry products: Gümüşhane pestil and köme. Turkish Journal of Agriculture and Forestry, 37: 762–771, 2013.

Hittite Journal of Science and Engineering, 2016, 3 (2) 99-104
ISSN NUMBER: 2149-2123
DOI: 10.17350/HJSE19030000038

The Representation, Generalized Binet Formula and Sums of The Generalized Jacobsthal *p*-Sequence

Ahmet Daşdemir
Kastamonu University, Department of Mathematics, Kastamonu, TURKEY

ABSTRACT

In this study, a new generalization of the usual Jacobsthal sequence is presented, which is called the generalized Jacobsthal ***p***-sequence. The generating matrix, the generalized Binet formula, the generating functions and the combinatorial representations of the generalized Jacobsthal ***p***-sequence are investigated. Moreover, certain sum formula consisting of the terms of the generalized Jacobsthal ***p***-sequence are given.

Article History:
Received: 2016/08/09
Accepted: 2016/12/08
Online: 2016/12/31

***Correspondence to**: Ahmet Daşdemir, Kastamonu University, Faculty of Arts and Sciences, Department of Mathematics, Kastamonu, Turkey*
Tel: +90 (366) 280 1960
Fax: +90 (366) 215 4469
E-Mail: ahmetdasdemir37@gmail.com

Keywords:
Jacobsthal sequence; Generating Matrix; Binet Formula; Combinatorial representation.

INTRODUCTION

Over the years, several articles have been appeared in many journals relating the integer sequences to growth patterns in plants. Among these integer sequences, Fibonacci sequence has achieved a kind of celebrity status. It is famous for possessing wonderful and amazing properties. For example, it is defined by a recurrence relation, and the ratios of its consecutive terms converge to the golden mean. Since this sequence has very wide applications, ones can find many interesting generalizations, i.e., one of them is given by Stakhov [1]. Under the special assumptions, the Fibonacci *p*-sequence reduces to the classical Fibonacci sequence. In addition, Stakhov and Rozin have presented number of properties and many applications of the Fibonacci *p*-sequence [2]. Kilic has studied the combinatorial representations, Binet formula and sums of Fibonacci *p*-sequence [3].

With the development of computer science and the onset of the digital age, the usual Jacobsthal sequence has extensively been investigated. It is defined by a recurrence relation, as the Fibonacci sequence. Horadam has given the important results for the Jacobsthal sequence [4]. Cerin has studied the sums of the terms of the Jacobsthal sequence [5]. In an investigation of the integer sequence defined by a recurrence relation, matrix theory has played an important and effective role. Quite apart from pursuing the discovery of the additional formulas by the matrix technics, the different matrices for obtaining new results can be introduced. Chen and Louck have investigated an *nxn* companion matrix and shown the combinatorial representation of the sequence generated by the *n*th power of the matrix [6]. Considering the matrix theory, Koken and Bozkurt have presented the Jacobsthal *F*-matrix and some results [7]. In the literature, there exist many other references on the subject which are not given here.

The object of this article is to give a new definition for the generalization of the usual Jacobsthal sequence. The generating matrix, the Binet formula, characteristic equations, generating functions, combinatorial representations and sums of the terms of the generalized Jacobsthal sequence are respectively studied.

Generalized Jacobsthal *p*-sequence

Generalization of Jacobsthal Sequence

First of all, the generalization of the usual Jacobsthal sequence is denoted by $J_p(n)$ and defined as follows: for $\forall p \in Z^+$ and $n > p+1$,

$$J_p(n) = J_p(n-1) + 2J_p(n-p-1) \tag{1}$$

with initial conditions

$$J_p(1) = J_p(2) = \cdots = J_p(p+1) = 1 \quad . \tag{2}$$

Obviously, when p=1, the generalized Jacobtshal p-sequence reduces to the usual Jacobtshal sequence. If the generalized Jacobthsal p-sequence is extended to backwards by using Eqs. (1)-(2), the following statements are obtained:

$$\begin{gathered} J_p(0) = J_p(-1) = \cdots = J_p(-p+1) = 0 \\ 2J_p(-p) = 1 \\ J_p(-p-1) = J_p(-p-2) = \cdots = J_p(-2p+1) = 0 \end{gathered} \tag{3}$$

Depending the choice of the value of p, both the recurrence relation and the initial conditions of considered sequence change. Hence, it is difficult and troublesome to compute the terms of the generalized Jacobsthal p -sequence for all the values of p. To facilitate this process, the generating matrix of the generalized Jacobsthal p-sequences is now presented as in the form

$$\mathbf{G_p} = \left[g_{ij} \right]_{(p+1)\times(p+1)} = \begin{bmatrix} 1 & 0 & \cdots & \cdots & \cdots & 0 & 2 \\ 1 & 0 & \cdots & \cdots & \cdots & \cdots & 0 \\ 0 & 1 & 0 & \cdots & \cdots & \cdots & 0 \\ \vdots & 0 & \ddots & \ddots & \vdots & \vdots & \vdots \\ \vdots & \vdots & \ddots & \ddots & \ddots & \vdots & \vdots \\ \vdots & \vdots & \vdots & 0 & 1 & 0 & 0 \\ 0 & \cdots & \cdots & \cdots & 0 & 1 & 0 \end{bmatrix}. \tag{4}$$

Additionally, a new matrix is defined as follows:

$$\mathbf{F_p} = \left[\left\{ v_{n+1}^{p} \right\} \quad \left\{ v_{n-p+1}^{2p} \right\} \quad \left\{ v_{n-p}^{2p} \right\} \quad \cdots \quad \left\{ v_{n}^{2p} \right\} \right]_{(p+1)\times(p+1)} \tag{5}$$

where

$$v_n^{tp} = t.\left[J_p(n) \quad J_p(n-1) \quad \cdots \quad J_p(n-p) \right]^T . \tag{6}$$

The matrix $\mathbf{F_n}$ will be called the generalized Jacobsthal p-matrix later. It should be noted that, for p=1, the generalized Jacobsthal p-matrix reduces to the usual form given by Koken and Bozkurt [7].

From Eq. (1), the following matrix can immediately be written

$$\mathbf{F_{n+1}} = \mathbf{G_p F_n} \quad . \tag{7}$$

Then, the following theorem can be given.

Theorem 1 For any $n;p$>0,

$$\mathbf{F_n} = \mathbf{G_p}^{\mathbf{n}} . \tag{8}$$

Proof. To prove the theorem, the induction method on n is used. Taking n=1 and considering Eqs. (1)-(3), $\mathbf{F_1}=\mathbf{G_p}$ is obtained. It is thus to be true for n=1. Now suppose that Eq. (8) holds for any n-1, namely $\mathbf{F_{n-1}} = \mathbf{G_p}^{\mathbf{n-1}}$. From Eqs. (1) and (7) and the assumption, $\mathbf{G_p}^{\mathbf{n}} = \mathbf{G_p G_p}^{\mathbf{n-1}} = \mathbf{G_p F_{n-1}} = \mathbf{F_n}$ is found, which is the desired result.

Theorem 2 Let $\mathbf{F_n}$ be defined as in (5). Then,

$$\det \mathbf{F_n} = 2^n (-1)^{np} \quad . \tag{9}$$

Proof. Taking Theorem 1 into account, computing the determinant of the matrix $\mathbf{G_p}$ by the Laplace expansion with respect to (p+1)th column and considering the matrix identities, the proof can easily be obtained.

The following corollary can be written from the fundamental matrix identities such that $\mathbf{F_{n+m}}=\mathbf{F_n F_m}$ or $\mathbf{F_{n-m}}=\mathbf{F_n F_{-m}}$. It therefore is given without the proof.

Corollary 3 Let $Jp(n)$ be the nth generalized Jacobsthal p-number. Then

$$J_p(n+m) = J_p(n) J_p(m+1) + 2\sum_{i=1}^{p} J_p(n-p-1+i) J_p(m+1-i) \quad . \tag{10}$$

Actually, for p-1, Eq. (10) becomes the well-known following formula given by Koken and Bozkurt [7]:

$$J(n+m) = J(n) J(m+1) + 2J(n-1) J(m).$$

Binet Formula and Generating Functions

In this section, the Binet formula and the generating functions of the generalized Jacobsthal p-sequence will be studied. To do this, the limit of the ratio of the adjacent generalized Jacobsthal p-sequence for the case where $n \to \infty$ is considered. First of all, the following definition is introduced:

$$\lim_{n\to\infty} \frac{J_p(n)}{J_p(n-1)} = x \tag{11}$$

The ratio of the adjacent generalized Jacobsthal p -sequence is rearranged in the form

$$\frac{J_p(n)}{J_p(n-1)} = 1 + \frac{2}{\dfrac{J_p(n-1)J_p(n-2)\cdots J_p(n-p)}{J_p(n-2)J_p(n-3)\cdots J_p(n-p-1)}} \tag{12}$$

Substituting the last equation into Eq. (11), the following algebraic equation for the generalized Jacobsthal p -sequence is obtained:

$$x^{p+1} - x^p - 2 = 0\,. \tag{13}$$

It should be noted that Eq. (13) possesses the $(p+1)$th degree and $(p+1)$ roots such as $x_1, x_2,\ldots,x_{p+1}$ according to the famous "Fundamental Theorem of Algebra". Also, when $p=1$ Eq. (13) reduces to well-known form for the usual Jacobsthal sequence.

The Binet formula for the generalized Jacobsthal p-sequence will be investigated. But the following lemma is first recalled [3].

Lemma 4 Let $a_p = \frac{1}{p}\left(\frac{p-1}{p}\right)^{p-1}$ Then $a_p > a_{p+1}$ for any $p>1$.

Then, the following lemma can be written.

Lemma 5 The characteristic equation of the generalized Jacobsthal p -sequence $x^{p+1}-x^p-2=0$ does not have multiple roots for $p>1$

Proof. Let $f(x) = x^{p+1}-x^p-2$. Suppose that α is a multiple root of $f(x) = 0$. Note that $\alpha \neq 0$ and $\alpha \neq 1$. Since α is a multiple root, $f(\alpha) = \alpha^{p+1}-\alpha^p-2=0$ and $f'(\alpha) = \alpha^{p-1}((p+1)\alpha-p)=0$. Then, $\alpha = p/(p+1)$ Consequently,

$$0 = -f(\alpha) = -\alpha^{p+1} + \alpha^p + 2 = \frac{1}{p+1}\left(\frac{p}{p+1}\right)^p + 2 = a_{p+1} + 2$$

Considering Lemma 4, $\alpha_2=1/4<1$, and $\alpha_p > \alpha_{p+1}$ for $p > 1$, $\alpha_{p+1} \neq -2$, which is a contradiction. The equation $f(z) = 0$ does therefore not have multiple roots.

Suppose that $f(\lambda)$ is the characteristic polynomial of the generalized Jacobsthal p-matrix $\mathbf{F_n}$. Considering the identities of the companion matrix, then $f(\lambda)= \lambda^{p+1}-\lambda^p-2$. Also $\lambda_1, \lambda_2, \ldots, \lambda_{p+1}$ represent the eigenvalues of the matrix $\mathbf{G_p}$. By Lemma 5, it is known that each of $\lambda_1, \lambda_2, \ldots, \lambda_{p+1}$ are distinct from the other. Let $\wedge$ be a Van*d*ermonde matrix of order $(p + 1)$ x $(p + 1)$ as follows:

$$\mathbf{\Lambda} = \begin{bmatrix} \lambda_1^{\,p} & \lambda_1^{\,p-1} & \cdots & \lambda_1 & 1 \\ \lambda_2^{\,p} & \lambda_2^{\,p-1} & \cdots & \lambda_2 & 1 \\ \lambda_3^{\,p} & \lambda_3^{\,p-1} & \cdots & \lambda_3 & 1 \\ \vdots & \vdots & & \vdots & \vdots \\ \lambda_{p+1}^{\,p} & \lambda_{p+1}^{\,p-1} & \cdots & \lambda_{p+1} & 1 \end{bmatrix} \tag{14}$$

In addition, the following column vector is defined:

$$\mathbf{d_i^k} = \begin{bmatrix} \lambda_1^{\,n+p+1-i} & \lambda_2^{\,n+p+1-i} & \cdots & \lambda_{p+1}^{\,n+p+1-i} \end{bmatrix}^T$$

The transpose of the matrix $\wedge$ is denoted by $\mathbf{V}$, and $\mathbf{V_j^{(i)}}$ represents a $(p+1)$x $(p+1)$ matrix constructed by replacing the jth column of $\mathbf{V}$ by $\mathbf{d_i^k}$. Then, the generalized Binet formula for the generalized Jacobtshal p -sequence can be given by the following theorem.

Theorem 6 Let $J_p(n)$ be the nth generalized Jacobsthal p-sequence. Then

$$f_{ij} = \frac{\det\left(\mathbf{V_j^{(i)}}\right)}{\det\left(\mathbf{V}\right)}\,,$$

where $\mathbf{F_n} = [f_{ij}]$.

Proof. To prove the theorem, a well-known method is applied. Since the eigenvalue of the matrix $\mathbf{G_p}$ are distinct, this matrix is diagonalizable. It is easy to show that

$$\mathbf{G_pV = VD},$$

where $\mathbf{D} = diag\,(\lambda_1, \lambda_2, \ldots, \lambda_{p+1})$. Considering the fact that Vandermonde matrix $\mathbf{V}$ is invertible, $\mathbf{V^{-1}G_pV = D.}$ Hence, the matrix $\mathbf{G_p}$ is similar to the diagonal matrix $\mathbf{D}$. So, $\mathbf{F_nV=VD^n}$. Since $\mathbf{F_p} = [f_{ij}]$, the following linear system of equations:

$$\begin{aligned} f_{i1}\lambda_1^{\,p} + f_{i2}\lambda_1^{\,p-1} + \cdots + f_{i,p+1} &= \lambda_1^{\,p+n+1-i} \\ f_{i1}\lambda_2^{\,p} + f_{i2}\lambda_2^{\,p-1} + \cdots + f_{i,p+1} &= \lambda_2^{\,p+n+1-i} \\ &\vdots \\ f_{i1}\lambda_{p+1}^{\,p} + f_{i2}\lambda_{p+1}^{\,p-1} + \cdots + f_{i,p+1} &= \lambda_{p+1}^{\,p+n+1-i} \end{aligned}$$

By the Cramer's rule, the desired result is obtained.

Consequently, the following corollary can be directly obtained from Theorem 6.

Corollary 7 For the nth term of the generalized Jacobsthal p-sequence,

$$J_p(n) = \frac{\det\left(\mathbf{V_1}^{(2)}\right)}{\det(\mathbf{V})} = \frac{1}{2}\frac{\det\left(\mathbf{V_{p+1}}^{(1)}\right)}{\det(\mathbf{V})}.$$

Now the generating functions of the generalized Jacobsthal p-sequence is presented by the following theorem.

Theorem 8 Let $J_p(n)$ be the nth term of the generalized Jacobsthal p-sequence. Then for $n > 1$,

$$x^n = J_p(n-p+1)x^p + 2\sum_{j=1}^{p} J_p(n-p+1-j)x^{j-1}.$$

Proof. (Induction method on n) It is clear that the equation holds for $n = p+1$. Suppose that the equation holds for any $n > p+1$. Hence, by the assumption and the definition of the generalized Jacobsthal p-sequence,

$$\begin{aligned} x^{n+1} = x^n x &= J_p(n-p+1)x^{p+1} + 2\sum_{j=1}^{p} J_p(n-p+1-j)x^j \\ &= \left(J_p(n-p+1) + 2J_p(n-2p+1)\right)x^p + 2J_p(n-2p+2)x^{p-1} + \cdots + 2J_p(n-p)x + 2J_p(n-p+1) \\ &= J_p(n-p+2)x^p + 2\sum_{j=1}^{p} J_p(n-p+2-j)x^{j-1} \end{aligned}$$

is obtained. So, the proof is completed.

Combinatorial Representations

Now the combinatorial representations of the generalized Jacobsthal p-sequence are investigated. First of all, introduce the following companion matrix:

$$C(c_1, c_2, \ldots, c_k) = \begin{bmatrix} c_1 & c_2 & c_3 & \cdots & c_k \\ 1 & 0 & 0 & \cdots & 0 \\ 0 & 1 & 0 & \cdots & 0 \\ \vdots & \ddots & \ddots & \ddots & \vdots \\ 0 & \cdots & 0 & 1 & 0 \end{bmatrix}_{k\times k} \tag{15}$$

Also, recall that the following theorem which give the opportunity to derive the elements in the nth power of the matrix C [6].

Theorem 9 Let the matrix $C = (c_{ij})_{kxk}$ be as in (15). The element $c_{ij}^{(n)}$ in the matrix C^n is given by the formula

$$c_{ij}^{(n)}(c_1, c_2, \ldots, c_k) = \sum_{(t_1,\ldots,t_k)} \frac{t_j + t_{j+1} + \cdots + t_k}{t_1 + t_2 + \cdots + t_k} \times \binom{t_1 + t_2 + \cdots + t_k}{t_1, t_2, \cdots, t_k} c_1^{t_1} \ldots c_k^{t_k}, \tag{16}$$

where the summation is over non-negative integers satisfying $t_1 + 2t_2 + \ldots + kt_k = n - i + j$, and the coefficients are defined as 1 for $n = i-j$.

Thus the following lemma can immediately be obtained from the above theorem without the proof.

Lemma 10 Let the matrix $\mathbf{G_p^n} = [g_{ij}^{(n)}]$ be as in (6). Then,

$$g_{ij}^{(n)} = \sum_{(m_1,\ldots,m_{p+1})} \frac{m_j + m_{j+1} + \cdots + m_{p+1}}{m_1 + m_2 + \cdots + m_{p+1}} \times \binom{m_1 + m_2 + \cdots + m_{p+1}}{m_1, m_2, \cdots, m_{p+1}} 2^{m_{p+1}},$$

here the summation is over non-negative integers satisfying $m_1 + 2m_2 + \cdots + (p+1)m_{p+1} = n - i + j$.

Finally, the following corollaries can directly be written from Lemma 10.

Corollary 11 Let $J_p(n)$ be the nth term of the generalized Jacobsthal p-sequence. Then

i. $$J_p(n) = \frac{1}{2} \sum_{(m_1,\ldots,m_{p+1})} \frac{m_{p+1}}{m_1 + m_2 + \cdots + m_{p+1}} \times \binom{m_1 + m_2 + \cdots + m_{p+1}}{m_1, m_2, \cdots, m_{p+1}} 2^{m_{p+1}}$$

where the summation is over non-negative integers satisfying $m_1 + 2m_2 + \ldots + (p+1)m_{p+1} = n + p$.

ii. $$J_p(n) = \sum_{(m_1,\ldots,m_{p+1})} \binom{m_1 + m_2 + \cdots + m_{p+1}}{m_1, m_2, \cdots, m_{p+1}} 2^{m_{p+1}}$$

where the summation is over non-negative integers satisfying $m_1 + 2m_2 + \ldots + (p+1)m_{p+1} = n - 1$.

Sum Formula

To find the sum of terms of the generalized Jacobsthal p-sequence, certain methods are now used. To do this, some generating matrices by extending the matrix $\mathbf{G_p}$ will be used. Let S_n be the sums of the generalized Jacobsthal p-sequence as follows:

$$S_n = \sum_{i=1}^{n} J_p(i) \tag{17}$$

Also, the following matrices are defined:

$$\mathbf{T} = \begin{bmatrix} 1 & 0 & 0 & \cdots & 0 & 0 \\ 1 & & & & & \\ 0 & & & & & \\ \vdots & & & \mathbf{G_p} & & \\ 0 & & & & & \\ 0 & & & & & \end{bmatrix} \tag{18}$$

$$\mathbf{A_n} = \begin{bmatrix} 1 & 0 & 0 & \cdots & 0 & 0 \\ S_n & & & & & \\ S_{n-1} & & & & & \\ \vdots & & & \mathbf{F_n} & & \\ S_{n-p+1} & & & & & \\ S_{n-p} & & & & & \end{bmatrix} \tag{19}$$

Thus, the following theorem can be given.

Theorem 12 For the matrices $\mathbf{T}$ and $\mathbf{A_n}$,

$$\mathbf{A_n} = \mathbf{T}^n \tag{20}$$

Proof. (Induction method on n) When $n = 1$, it is clear that the equation holds. Suppose that Eq. (20) holds for n. On the other hand, by the assumption and $S_{n+}1 = J_p(n+1) + S_n$,

$$\mathbf{T}^{n+1} = \mathbf{T}^n\mathbf{T} = \mathbf{A_n}\mathbf{T} = \mathbf{A_{n+1}},$$

which completes the proof.

Before the main result, the following useful lemma is presented.

Lemma 13 Let $J_p(n)$ be the nth term of the generalized Jacobsthal p-sequence. Then, for all the integers $n, m \geq 0$,

$$J_p(n+m+p+1) = J_p(n+m+1) + 2\sum_{i=1}^{p} J_p(n+m-p+i)$$

Proof. The proof can easily be obtained by the definition of the generalized Jacobsthal p-sequence.

A new matrix is defined in the form

$$\mathbf{W}=\begin{bmatrix} 1 & 0 & 0 & \cdots & 0 & 0 \\ -\frac{1}{2} & \lambda_1^{\,p} & \lambda_2^{\,p} & \cdots & \lambda_p^{\,p} & \lambda_{p+1}^{\,p} \\ -\frac{1}{2} & \lambda_1^{\,p-1} & \lambda_2^{\,p-1} & \cdots & \lambda_p^{\,p-1} & \lambda_{p+1}^{\,p-1} \\ \vdots & \vdots & \vdots & \vdots & \vdots & \vdots \\ -\frac{1}{2} & \lambda_1 & \lambda_2 & \cdots & \lambda_p & \lambda_{p+1} \\ -\frac{1}{2} & 1 & 1 & \cdots & 1 & 1 \end{bmatrix}, \quad (21)$$

where λ_i (i = 1, 2 , ..., p + 1) have been defined before.

Then the following theorem is given to compute the sums of the generalized Jacobsthal p-sequence by using matrix method.

Theorem 14 Let S_n be as in (17). Then

$$S_n=\frac{1}{2}\left(J_p\left(n+p+1\right)-1\right)$$

Proof. Computing det**W** by the Laplace expansion of the determinant with respect to the first row, det**W**=det**V** is obtained, where **V** is defined as before. Hence the characteristic equation of the matrix **W** is $(x\text{-}1)\text{x}(x^p\text{-}x^{p-1}\text{-}1)$. It can be said from Lemma 5 that the eigenvalues of the matrix **W** are 1, λ_1 ,..., λ_{p+1} and different from each other. Therefore, $\mathbf{TW}=\mathbf{W}\bar{\mathbf{D}}$ can be written, where $\bar{\mathbf{D}}$ = *diag* (1, λ_1 ,..., λ_{p+1}). Consequently, $\mathbf{A_n W}=\mathbf{W}\bar{\mathbf{D}}^{\mathbf{n}}$. The element (2,1)th in the matrix $\mathbf{A_n}=[a_{ij}]_{(p\text{-}2)\text{x}(p+2)}$ is $a_{21}=S_n$, and by Lemma 13, the desired result is directly obtained.

CONCLUSION

In this study, the new generalization of the usual Jacobsthal sequence is presented, which is called as "the generalized Jacobsthal p-sequence". The generating matrix of this generalized sequence is given, and a few important results are obtained by employing the matrix. Also the generating matrix is extended to certain matrix representations, and it is shown that the sums of the generalized Jacobsthal p-sequence could be derived directly by using the representations. Moreover the generalized Binet formula, the generating functions and the combinatorial representations of the generalized Jacobsthal p-sequence are presented.

ACKNOWLEDGEMENTS

This study was supported by Kastamonu University Scientific Research and Development Office under the project number KÜ-BAP01/2016-4. The author also would like to thank the referees for their very helpful and detailed comments.

REFERENCES

1. Stakhov AP. A generalization of the Fibonacci Q−matrix. National Academy of Sciences of Ukraine 9 (1999) 46−49.
2. Stakhov AP, Rozin B. Theory of Binet formulas for Fibonacci and Lucas p−numbers. Chaos Solitions and Fractals 27 (2006) 1162−1177.
3. Kilic E. The Binet formula, sum and representations of generalized Fibonacci p−numbers. European Journal of Combinatorics 29 (2008) 701−711.
4. Horadam AF. Jacobsthal Representation Numbers. Fibonacci Quarterly 34 (1996) 40−54.
5. Cerin Z. Sums of Squares and Products of Jacobsthal Numbers. Journal of Integer Sequences 10 (2007) Article 07.2.5.
6. Chen WYC, Louck JD. The combinatorial power of the companion matrix. Linear Algebra and its Applications 232 (1996) 261−78.
7. Koken F, Dozkurt D. On the Jacobsthal Numbers by Matrix Methods. International Journal of Contemporary Mathematical Sciences 3(13) (2008) 605−614.

Hittite Journal of Science and Engineering, 2016, 3 (2) 105-109
ISSN NUMBER: 2149-2123
DOI: 10.17350/HJSE19030000039

Chemical Composition, Antimicrobial and Antioxidant Activities of Essential Oil from *Pedicularis condensata* BIEB.

Osman Üçüncü[1,2], Cemalettin Baltacı[1], Şeyda Merve İlter[1]
[1]Gumushane University, Department of Food Engineering, Gumushane, TURKEY
[2]Gumushane University, Medical Plants Traditional Medicine Practice & Research Centre, Gumushane, TURKEY

ABSTRACT

The chemical composition of the essential oil obtained from the dried aerial parts of Pedicularis condensata was analyzed by GC-FID and GC-MS. Thirty-eight components have been identified in the essential oil of P. condensata. The major compounds of the essential oil were pentacosane (21.28%), hexadecanoic acid (18.48%) and tricosane (13.70%). The antimicrobial activity of the essential oil was also investigated and it showed moderate antimicrobial and antifungal activites aganist twelve gram negative bacteria and five fungi. The amount of total phenolic and DPPH reducing activity quantified essential oil in P. condensata were found as 198.28 GGA/L and 10.90 % respectively.

Article History:
Received: 2016/10/01
Accepted: 2016/12/08
Online: 2016/12/31

***Correspondence to**: Osman Ucuncu, Gumushane University, Faculty of Engineering & Natural Sciences, Department of Food Engineering, Gumushane, Turkey*
Tel: +90 (456) 233 1000 / 1861
Fax: +90 (456) 233 1075
E-Mail: osmanucuncu@yahoo.com

Keywords:
Pedicularis condensata; Essential oil; GC-FID; GC-MS; Antimicrobial and antioxidant activity; Pentacosane.

INTRODUCTION

Pedicularis L. is a large hemi parasitic genus and, 12 taxa of *Pedicularis* are existing in Turkey [1]. Traditionally, *Pedicularis* was placed in Scrophulariaceae but, this genus has been transferred to Orobanchaceae based on molecular evidence [2,3]. Iridois and phenylpropanoid glycosides were isolated from *P. condensata* Bieb. [4]. Lignans glycosides, flavonoids and alkaloids were also obtained from some members of the *Pedicularis* as well as Iridois and phenylpropanoid glycosides [5]. Some species of the *Pedicularis* are used as traditional medicine by Chinese people [5]. Li et al. (2014) also determined that extracts of some species of *Pedicularis* from China have antitumor, hepatoprotective, anti-oxidative, antibacterial activity, antihaemolysis, fatigue relief of skeletal muscle and nootropic effects. The genus *Pedicularis* comprising about 500 medicinal herbs and mostly endemic to China, is one of those genera of this family [6]. Several species of this genus, e.g., *P. muscicola, P. oliveriana, P. kansuensis* and *P. rhinanthoides*, have been using in Tibetan medicine system [6,7].

The aim of this study was to investigate the major volatiles and biological activities of the essential oil from *P. condensata* by GC-MS/GC-FID. Furthermore, It was also tested the bioactive properties of essential oil of *P. condensata.*

MATERIALS AND METHODS

Plant Sample Collection

Pedicularis condensata Bieb. was collected from Özkürtün-Kürtün, Gümüşhane: (40°40'25"K, 39°10'20"D at 1740 m above see level) in the North-Eastern part of Turkey(A7) in Agust 2013. The plant was authenticated immediately and air-dried at room temperature for later analysis [8,9]. And a voucher specimen (No. M. Gultepe 513 KTUB) was deposited in the Herbarium of the Department of Biology, Faculty of Science, Karadeniz Technical University, Turkey.

Isolation of the essential oil: Crude essential oil of *P. condensata* was obtained from the air-dried crushed material (*ca.* 100g) by hydrodistillation in a clevenger-type apparatus with cooling bath (-15 °C) system (4 h) (yield: 0.016 % (w/w)) [10,11]. The obtained oil was

extracted with HPLC grade *n*-hexane (0.5 mL) and dried over anhydrous sodium sulphate and stored at 4-6 °C in a sealed brown vial. 1 mL of the extract was directly injected into the GC-MS instrument.

Gas chromatography (GC) and Gas chromatography-mass spectrometry (GC-MS) analyzes: The chromatographic column used for the analysis was a HP-5MS capillary column. The capillary GC-FID analysis was performed using an Agilent-5973 Network System, equipped with a FID and a split inlet. GC-MS and GC-FID analyses were as described previously [10].

Identification of components: The identity of the components was achieved from their retention indices, determined by Kovats method using *n*-alkanes (C_6-C_{40}) as standards. The constituent of oil was identified by comparison of their mass spectra with those of mass spectral libraries (NIST and Wiley 7NL) and data [12,13].

Antimicrobial activity assessment: All test micrrorganisms were obtained from Gumushane University Food Engineering Laboratories. The oil was dissolved in hexane to prepare chemical stock solution of 10000 ppm. The antimicrobial activity of the essential oil were determined against to *Aeromonas hydrophila* ATCC 7965, *Bacillus cereus* ATCC 33019, *Bacillus subtilis* ATCC 6633, *Enterobacter cloacea* ATCC 13047, *Escherichia coli* ATCC 11230, *Escherichia coli* O157:H7 ATCC 33150, *Klebsiella pneumoniae* ATCC 13883, *Listeria monocytogenes* ATCC 7644, *Proteus vulgaris* ATCC 13319, *Pseudomonas aeruginosa* ATCC 17853, *Salmonella typhimurium* ATCC 14028, *Staphylococcus aureus* ATCC 25923, *Saccharomyces cerevisiae* BC 5461, *Candida albicans* ATCC 1223 by using agar-well diffusion method [14,15].

Determination of free radical scavenging activity: Free radical scavenging activity of the samples was carried out by DPPH method according to the literature [16]. The measurements were performed in five times and the results were averaged. The results were given as % inhibition;

% Inhibition = (Control Absorbance-Absorbance of the Sample / Control Absorbance) x 10

The amount of total phenolic: Folin-Ciocalteu method used by Sagdic *et al.* was applied for the analysis of total phenolic substance t amount [17]. The measurements were performed in five times and the results were averaged. The total phenolic substance amount results were given as (GAE) / L sample being equivalent of mg gallic acid. Calculations were done according to the as described previously [18].

RESULTS AND DISCUSSION

The GC-FID and GC-MS analysis of *P. condensata* essential oil is presented in Table-1. Altogether, 38 essential compounds were identified with HP-5MS column, representing 86.84 % of the total oil and the major compounds were pentacosane (21.28%), hexadecanoic acid (18.48%), tricosane (13.70), tetrahydro-2,5-dimethyl furan (7.63%) and 6,10,14-trimethyl-2-pentadecanone (7.33%). Chemical contents were characterized on the basis of a typical library search and literature data [12, 19].

The compounds were seperated 6 classes, which were terpenes or terpene related, alcohols, acids, esters, hydrocarbones and others (Table 1).

In literature survey, 6,10,14-trimethyl-2-pentadecanone, and (*E*)-*β*-damascenone compounds were found in GC-MS analyzes of some *Pedicularis* species (*P. sibthorpii* and *P. wilhelmsiana*) [20]. But other compounds showed large differences. All chemical profile of the essential oils showed big differences as in our case, which can be explained by the environmentally, harvest time, locality and the subspecies of the plant used.

Essential oil extracts of *P. condensata* exhibited different inhibition levels against selected bacteria and fungi (in Table 2). In the antimicrobial activity study, the inhibition zone increased with increasing concentration of essential oil extract. At 1000 ppm and 500 ppm concentrations, samples exhibited remarkable inhibition activity against bacteria, and bacterial inhibition of essential oil extracts of *P. condensata* was stronger than those of fungi. However, the essential oil extracts of plant showed antibacterial activity aganist *B.cereus*, *E.coli* and *Sal. typhimurium* in the 1000 ppm concentration.

The essential oil exhibited weak antioxidant activity. As shown in Table 3, essential oil of *P. condensata* were reduce the radical activity DPPH to the yellow-colored diphenylpicrylhydrazine. The effect of radical activity DPPH was observed for the essential oil was %10.90. The high relative total phenolic content of essential oil of *P. condensata* were found as 198.28 GGA/L (Table 3).

In conclusion, It have been demonstrated that essential oil of *P. condensata* contains high levels of total phenolic compounds and shows reducing power and scavenging effects on free radicals. The results in the study indicate essential oil of *P. condensata* not only do not play a major role as dietary antioxidants, but also may use strong

Table 1. Identified Components in the Essentaial Oil of *Pedicularis condensata* BIEB.

	Compounds	*RT(min)*	*Area %*	*Exp. RI*
No	*Terpene or terpene related*			
1	*Limonene*	*13.086*	*0.75*	*1031*
2	*α-Terpinolene*	*16.138*	*0.46*	*1101*
3	*(E)- β-Damascenone*	*28.979*	*0.30*	*1389*
4	*Dehydro-β-ionone*	*30.219*	*0.16*	*1418*
5	*Geranyl acetone*	*31.745*	*0.40*	*1455*
6	*α-Ionone*	*33.206*	*0.49*	*1491*
7	*Aromadendrene*	*33.349*	*0.21*	*1494*
8	*6.10.14-Trimethyl-2-pentadecanone*	*46.433*	*7.33*	*1847*
		Total	*10.10*	
	Alcohols			
9	*2-methyl-1-butanol*	*4.502*	*0.88*	*727*
10	*3-Penten-2-ol*	*5.135*	*1.53*	*770*
11	*5-methyl-3-heptanol*	*9.683*	*1.40*	*943*
12	*6-methyl-2-heptanol*	*10.038*	*0.52*	*952*
13	*2-Methyl-1.3-pentanediol*	*11.647*	*0.23*	*997*
14	*1-Hexadecanol*	*47.591*	*0.17*	*1882*
15	*trans-9-Hexadecen-1-ol*	*47.925*	*0.28*	*1891*
		Total	*5.01*	
	Acids			
16	*Hexadecanoic acid*	*50.539*	*18.48*	*1971*
17	*Oleic acid*	*55.780*	*0.63*	*2140*
		Total	*19.11*	
	Esters			
18	*Methyl-2-hydroxydodecanoate*	*40.356*	*0.15*	*1676*
19	*1.2-Benzenedicarboxylic acid. butyl 2-methylpropyl ester*	*47.287*	*0.84*	*1872*
20	*Hexadecanoic acid ethyl ester*	*51.324*	*0.22*	*1995*
		Total	*1.21*	
	Hydrocarbones			
21	*3.4-dimethyl-1-hexene*	*4.533*	*0.83*	*730*
22	*1-Tetradecene*	*29.725*	*0.16*	*1406*
23	*4-methyl-tetradecane.*	*32.062*	*0.19*	*1463*
24	*5-Octadecene*	*42.198*	*0.10*	*1761*
25	*Nonadecane*	*48.233*	*0.27*	*1900*
26	*Heneicosane*	*54.584*	*2.33*	*2100*
27	*Docosane*	*57.553*	*0.70*	*2200*
28	*Tricosane*	*60.428*	*13.7*	*2301*
29	*Tetracosane*	*63.194*	*1.62*	*2400*
30	*Pentacosane*	*66.506*	*21.28*	*2502*
		Total	*41.18*	
	Others			
31	*Furan. tetrahydro-2.5-dimethyl-*	*4.284*	*7.63*	*714*
32	*4-(Prop-2-enoyloxy)octane*	*10.998*	*0.36*	*979*
33	*Furan. 2-pentyl-*	*11.495*	*0.36*	*993*
34	*Benzothiazole*	*21.744*	*0.15*	*1225*
35	*1H-Indene. 2.3-dihydro-1.1.4.7-tetramethyl-*	*29.101*	*0.44*	*1392*
36	*3.7-Benzofurandiol. 2.3-dihydro-2.2-dimethyl*	*34.763*	*0.44*	*1530*
37	*13-Tetradecenal*	*38.062*	*0.12*	*1614*
38	*Pentadecanal*	*41.838*	*0.73*	*1716*
		Total	*10.23*	
	Total percentages		*86.84*	

Table 2. Screening Results for Antimicrobial activity of the Essential Oil of *Pedicularis condensata* BIEB.

Bacteria	*1000 ppm*	*500 ppm*	*200 ppm*	*100 ppm*
A. hydrophila	-	-	-	-
B. cereus	*8.19±0.10*	*4.97±0.10*	-	-
B. subtilis	-	-	-	-
Ent. cloacae	-	-	-	-
E. coli	*5.05±0.10*	-	-	-
E.coli O157:H7	-	-	-	-
K. pneumoniae	-	-	-	-
L.monocytogenes	-	-	-	-
P. vulgaris	-	-	-	-
Pseu. aeruginosa				
Sal. typhimurium	*9.10±0.10*	*5.28±0.10*	-	-
S. aureus	-	-	-	-
Fungus				
Sac. cerevisiae	-	-	-	-
C. albicans	-	-	-	-
A.niger	-	-	-	-
A.flavus	-	-	-	-
Penicillum	-	-	-	-

Table 3. Total phenolic content and reducing activity of *P. condensata* essential oil.

Sample	*Total phenolic content*	*Reducing activity*
Essential oil of P. condensata	*198.28 GGA/L*	*% 10.90*

antibacterial agents. However, further investigations are required to assay the antioxidant and antimicrobial effects in vivo and to evaluate its relevance to human health.

ACKNOWLEDGMENTS

This work was supported by the Scientific Research Fund of Gumushane University under the project number 13.F5115.02.2. We are thankful to Dr. Mutlu Gültepe for the identification of plant sample.

REFERENCES

1. Hedge, I.C. Digitalis L. In: Davis, PH, editor. Flora of Turkey and the East Aegean Islands, Vol. 6. Edinburgh: Edinburgh University Press, pp. 768-777, 1978.
2. Olmstead RG, and Reeves, PA. Evidence for the polyphyly of the Scrophulariaceae based on chloroplast rbcL and ndhF sequences. Annals of the Missouri Botanical Garden 82 (1995) 176–193.
3. Olmstead RG, de Pamphilis CW, Wolfe AD, Young ND, Elisons WJ, & Reeves, PA. Disintegration of the Scrophulariaceae. The American Journal of Botany 88(2001) 348– 361.
4. Akdemir Z, Çali I, Junior, P. Iridoid and phenylpropanoid glycosides from Pedicularis condensata, Phytochemistry 30 (1991) 2401–2402.
5. Li MX, He XR, Tao R, Cao, X. Phytochemistry and pharmacology of the genus Pedicularis used in traditional Chinese Medicine. The American Journal of Chinese Medicine 42 (2014) 1071–1098.
6. Zhang BB, Shi K, Liao ZX, Dai Y, Zou, ZH. Phenylpropanoid glycosides and triterpenoid of Pedicularis kansuensis Maxim. Fitoterapia 82 (2011) 854– 860.
7. Jiang TF, Ou QY, Shi, YP. Separation and determination of phenylpropanoid glycosides from Pedicularis species by capillary electrophoresis. Journal of Chromatography A 986 (2003) 163–167.
8. Davis PH. Flora of Turkey and the East Aegean Islands, Volume 10. Edinburgh University Press, Edinburgh 1988.
9. Güner A, Özhatay N, Ekim T, Başer KHC. Flora of Turkey and the East Aegean Islands, Volume 11. Edinburgh University Press, Edinburgh 2000.
10. Üçüncü O, Yayli N, Yaşar A, Terzioğlu S, Yayli, N. Chemical Composition of the Essential Oils from Flower, Leaf, and Stem of Senecio trapezuntinus Boiss. Grown in Turkey. Natural Product Communications 3 (2008) 925–928.
11. Güleç C, Yaylı N, Yeşilgil P, Terzioğlu S, Yaylı, N. Chemical composition and antimicrobial activities of the essential oil from the flowers of Delphinium formosum. Asian Journal of Chemistry 19 (2007) 4069–4074.
12. Adams R.P., Identification of Essential Oil Components by Gas Chromatography– Mass Spectroscopy, Allured, Carol Stream, IL, USA, 2004.
13. Kahriman N, Şenyürek Z, Serdaroğlu V, Kahriman A, Yayli, N. Chemical Composition and Biological Activity of Essential Oils of Sempervivum brevipilum Muirhead. Records of Natural Products 9 (2016) 603–608.
14. Maksimovic ZA, Dordeviv S, Mraovic, M. Antimicrobial Activity of Chenopodium botrys Essential Oil. Fitoterapia 76 (2005) 112–114.
15. Sağdıç O, Özcan, M. Antibacterial Activity of Turkish Spice Hydrosols, Food Control, 14 (2003)141–143.

16. Sanchez–Moreno C, Larrauri JA, Saura–Calixto, FA. Procedure to Measure the Antiradical Efficiency of Polyphenols, Journal of the Science of Food and Agriculture, 76 (1998) 270–276.
17. 17. Gámez–Meza N, Noriega–Rodríguez JA, Medina–Juárez LA, Ortega–García J, Cázarez–Casanova R, Angulo–Guerrero, O. Antioxidant activity in soybean oil of extracts from thompson grape bagasse, Journal of the American Oil Chemists' Society, 76 (1999) 1445–1447.
18. Üçüncü O, Baltacı C, İlter SM. Gladiolus italicus Miller Bitkisinin Uçucu Yağının Kimyasal Bileşimi ve Biyoaktif Özellikleri, GÜFBED/GUSTIJ 6 (2016) 150–156.
19. İskender NY, Kahriman N, Tosun G, Terzioğlu S, Karaoğlu ŞA, Yaylı, N. Chemical Composition and Antimicrobial Activity of the Essential Oils from the Aerial Parts of Astragalus hamzaoglui Extracted by Hydrodistillation and Microwave Distillation. Records of Natural Products 7 (2013) 177–183.
20. Khodaei L, Delezar A, Nazemiyeh H, Asnaashari S, Nahar L, Sarker, SD. Composition of the Volatile Oils of the Aerial Parts of Pedicularis sibthorpii and P. wilhelmsiana Growing in Iran. Journal of Essential Oil Bearing Plants 15 (2012) 352–356

Hittite Journal of Science and Engineering, 2016, 3 (2) 111-116
ISSN NUMBER: 2149-2123
DOI: 10.17350/HJSE19030000040

An Edible Mushroom With Medicinal Significance; *Auricularia polytricha*

Emre Avcı[1], Gamze Çağatay[1], Gülçin Alp Avcı[1], Menderes Suiçmez[1] and Şule Coşkun Cevher[2]
[1] Hitit University, Faculty of Science and Arts, Department of Molecular Biology and Genetics, Çorum, TURKEY
[2] Gazi University, Faculty of Science and Arts, Department of Biology, Ankara, TURKEY

ABSTRACT

Auricularia polytricha, also known as wood ear mushroom, is a macrofungus. The aim of study was to determine the antioxidant and antimicrobial activities of A. polytricha extracts with two different solutions. We used ethanol and distilled water as a solvent in order to prepare mushroom extracts. The water and ethanol extracts were evaluated for the total antioxidant status according to the procedures described in TAS Assay Kit (Rel Assay Diagnostics®, Turkey). Antimicrobial activity was investigated with disc diffusion method against two gram positive bacteria, two gram negative bacteria and one yeast. TAS values of ethanol extracts were determined higher than that of in distilled water extracts. In addition, it was observed that ethanol extracts have antimicrobial activity whereas water extracts have no antimicrobial activity. Ethanol extracts were more effective against Candida albicans (15.6 ± 1.5 mm) than other microorganisms. Significantly, ethanol extracts of mushroom showed antifungal activity. Among other four test microorganisms, Pseudomonas aeroginosa (13.1 ± 1.9 mm) had higher antimicrobial activity. In conclusion, the investigation of antioxidant and antimicrobial activities of edible mushrooms have become important for the discovery of new antimicrobial agents. A. polytricha has both antioxidant and antimicrobial properties against to C. albicans, E. coli, E. faecalis, P. aeroginosa, and S. aureus. And also, other positive contributions to health of this mushroom will be determined by means of the other studies planned.

Keywords:
Auricularia polytricha; Total Antioxidant Status; Antimicrobial Activity; extraction.

Article History:
Received: 2016/12/01
Accepted: 2016/12/20
Online: 2016/12/31

***Correspondence to**: Gamze Çağatay, Hitit University, Faculty of Science and Arts, Department of Molecular Biology and Genetics, Çorum, Turkey*
Tel: +90 (364) 226 7000-1716
Fax: +90 (364)227 7005
E-Mail: gamzecagatay@hitit.edu.tr

INTRODUCTION

Mushrooms play an important role in the carbon-nitrogen cycle by breaking down organic substance in nature [1]. In addition to its existence for centuries, fungi have been used as nutritious food in daily meal and therapeutic agent in medicine because they are rich in protein, vitamins, and minerals [2].

Auricularia polytricha is a macrofungus that is a member of Basidiomycota class and belongs to Auriculariaceae family [3]. They grow in Asia, tropical America, and other regions of the world [4]. The spread of fungal spores of *A. polytricha* are present in high amount during late July [5]. Culturing of this fungus is not difficult but slow like some other fungi [6]. *A. polytricha* is edible mushroom.

When the mushroom is fresh, the structure becomes rubbery, gelatinous, and ear-like. In contrast, it becomes shapeless and brittle if it is dried [7, 8]. As a consequence of its nutrient and medical value, the consumption and cultivation of *A. polytricha* have increased rapidly [9-12].

Up to now, some studies showed that lots of different mushroom species have antioxidant, cytotoxic, anti-proliferative, anti-diabetic, antimicrobial, and anti-inflammatory effects [13-18] In addition, since cell wall glucans of fungi indicates immunomodulatory properties, their secondary metabolites are active against bacteria and viruses [19, 20].The aim of the present study is to evaluate the total antioxidant status and antimicrobial effects of *A. polytricha*.

MATERIALS AND METHODS

Preparation of Mushroom Extract

Auricularia polytricha was obtained commercially (Agroma Food, Turkey). Dried mushroom samples were grounded in a grinder using a 2 mm diameter mesh. Then, they (10 g) were extracted in a Soxhlet extractor sequentially with 250 ml of distilled water and ethanol for 12 h. All the solvent extracted fractions were subjected in a rotary vacuum evaporator (Stuart Rotary Evaporator, RE300P). The residues were incubated a bit more of dryness for a while in an oven at 40^0C. The test residues were prepared as stocks using ultra-pure water and ethanol (1.5 mg/ml). After that, the extracts were filtered with 0.45 micrometer pore diameter to sterilize and tested for antimicrobial and the total antioxidant works. Extracts were kept in dark at 4^0C until executing the experiments.

Determination of Total Antioxidant Status (TAS)

The water and ethanol extracts were evaluated for the total antioxidant status according to the procedures described in TAS Assay Kit (Rel Assay Diagnostics®, Turkey). The data were calculated as a novel automated measurement method developed by Erel in 2004 [28]. In this method, the Fenton reaction forms a hydroxyl radical which was reacted with colorless substrate o-dianisidine. As a result of this reaction, a bright yellowish-brown dianisyl radical was obtained. The results were expressed as micromolar Trolox equivalents per liter (μmol Trolox Eq/L).

Determination of Antimicrobial Activity

Microorganisms and Growth Conditions

Enterococcus faecalis (ATCC-29212), *Staphylococcus aureus* (ATCC-25923) as gram-positive bacteria, *Pseudomonas aeroginosa (*ATCC-27853) and *Escherichia coli (*ATCC-25922) as gram-negative bacteria, and *Candida albicans (*ATCC-10231) as fungus were grown in order to investigate the antibacterial and antifungal effects of *A. polytricha*. Nutrient broth and agar (Diffco) were used for all microorganism culture. All strains were obtained from culture collection at -20°C in an appropriate medium containing 10% glycerol at Hitit University, Faculty of Science and Arts, Department of Molecular Biology and Genetic, Microbiology Research Laboratory Culture Collection.

Disc Diffusion Method

The antimicrobial activity of mushrooms extracts was evaluated through disc diffusion method. Microorganisms were activated two times in nutrient broth and incubated at 37^0C for 16-24 hours. After the activation for two times, optical density (OD) was adjusted to approximately 0.600 ($OD_{600} \approx 600$) for all microorganisms. 100 μl of culture suspensions were inoculated on Mueller Hinton Agar (MHA). Sterile prepared discs from Whatman Filter paper were placed into petri dishes. 10 μL of extracts dissolved previously within respective solvents (ultra-pure water and ethanol) were poured and incubated at 37°C for 24 hours. All inhibition zones were measured.

Statistical Analysis

Statistical analysis was performed on the data by SPSS 20.0 Bivariate Correlation Analysis (SPSS Inc., Chicago) with statistical significance determined at $P < 0.05$. All experiments were done in duplicate, and mean values are presented. The results were expressed as means ± standard deviations (SD).

RESULTS AND DISCUSSION

Determination of Total Antioxidant Status (TAS) of Extracts

In recent years, the antioxidant properties of mushrooms have been widely reported by many authors [22-25]. Researchers reported that *Auricularia polytricha* has lowering blood-fat, antioxidant, antitumor, and immunomodulatory activities [26-28]. In the present study, antioxidant activity of *A. polytricha* mushroom extracts with ethanol and distilled water investigated by TAS method is presented in Table 1. The antioxidant activity of distilled water extract was found to be 0.91 μmol Trolox Eqv./L. In contrast, ethanol extract was found as 0.73 μmol Trolox Eqv./L. When the antioxidant capacities of the extracts were compared, the distilled water extract of *A. polytricha* displayed higher capacity than ethanol extract.

In the literature, several studies related to the antioxidant activities of *A. polytricha* are present. In these studies, both ethanol and water extracts of *A. polytricha* have significant antioxidant activities determined using different methods such as in vitro free radical scavenging assays, DPPH assay and TAS assay [29-30]. In a previously reported work, *A. polytricha* had high DPPH scavenging activity [31]. Another study showed that *A. polytricha,* which is among the edible mushrooms, had the strongest radical scavenging and metal chelating activities in addition to the highest polyphenolic and flavonoid contents [32].

Table 1. Antioxidant activities of *A. polytricha* extracts in water and ethanol solvents.

	Ethanol extract	*Water extract*
*Total Antioxidant Status**	*0.73*	*0.91*

*Total Antioxidant Status were calculated as μmol Trolox Eqv./L.

Determination of Antimicrobial Activity of *A. polytricha* Extracts

Until now, antimicrobial activities of A. polytricha have been studied in different solvents such as ethanol and methanol. In a study, it was reported that A. polytricha has moderate inhibition against gram-positive S. aureus and gram-negative P. aeroginosa [32]. When using methanol as solvent for extraction process, antifungal activities of mushroom extract were inactive against C. albicans whereas A. polytricha inhibited the growth of E. coli and S. aureus [33]. In our study, antimicrobial activity of distilled water and ethanol extracts of A. polytricha was investigated against the test organisms. Antimicrobial activity results of mushroom extracts are summarized at Table 2. Ethanol extracts of A. polytricha had antimicrobial activity while no antimicrobial activity of distilled water extracts was observed against any of the organisms. The diameters of inhibition growth zones were measured as mm. As tested organisms, two species of gram positive bacteria (S. aureus and E. faecalis), two species of gram negative bacteria (P. aeroginosa and E. coli) and one species of fungi (C. albicans) were used. In ethanol mushroom extracts, the maximum inhibitory zone was determined against C. albicans (15.6 ± 1.5 mm) followed by P. aeroginosa (13.1 ± 1.9 mm), E. coli (10.6 ± 1.9 mm), and E. faecalis (10.3 ± 0.5 mm). In contrast, the minimum zone of inhibition was obtained against S. aureus (9.6 ± 0.8 mm). All microorganisms used in this study were found to have various degrees of zone. Additionally, the inhibition zones of tested microorganisms are shown in Figure 1 and 2. It could be concluded that A. polytricha had a significant antifungal activity and also was very active especially against Gram-negative bacteria in contrast to Gram-positive bacteria. All these results indicated that different extracts prepared in various solvents including ethanol, water, and methanol can have various degree of antimicrobial activity of A. polytricha. This situation could stem from different antimicrobial activity on the microorganisms of each solvent.

CONCLUSIONS

Currently, the investigation of antioxidant and antimicrobial activities of edible mushrooms has become significant. We studied the antioxidant and antimicrobial properties of ethanol and water extracts of *A. polytricha*. Results showed that both water and ethanol extracts have antioxidant activity. In addition, ethanol extracts had antimicrobial activity on tested organisms; but, antimicrobial properties were not determined in the distilled water extracts. In conclusion, the investigation of antioxidant and antimicrobial activities of edible mushrooms have become important for the discovery of new antimicrobial agents. A. polytricha has both antioxidant and antimicrobial properties against to C. albicans, E. coli, E. faecalis, P. aeroginosa, and S. aureus. And also, other positive contributions to health of this mushroom will be determined by means of the other studies planned.

Table 2. Antimicrobial effects of ethanol extract obtained from *A. polytricha*

Mushrooms Extracts		*S. aureus ATCC 25923*	*E. faecalis ATCC 29212*	*P. aeroginosa ATCC 27853*	*E. coli ATCC 25922*	*C. albicans ATCC 10231*
Ethanol extract	*IZ*	*9.6 ± 0.8*	*10.3 ± 0.5*	*13.1 ± 1.9*	*10.6 ± 1.9*	*15.6 ± 1.5*
	AI	*1.0*	*1.01*	*1.13*	*1.08*	*1.15*
Water extract		*ND*	*ND*	*ND*	*ND*	*ND*
Antibiotic		*7.0 ± 1.0*	*9.5 ± 2.0*	*8.7 ± 2.2*	*10.5 ± 2.5*	*ND*
Antifungal		*ND*	*ND*	*ND*	*ND*	*10.5 ± 1.5*

Values are mean of duplicate readings (mean ± S.D).

Antibiotic: Gentamycin; Antifungal: Flucanozole; ND: Not Determinate

IZ= Inhibition zone (in mm) includes the diameter of disc (6 mm); AI (activity index) = IZ of test sample / IZ of standard. Standards: Distilled Water (10µl/disc), Sodium hypochloride 3% (10µl/disc), Hydrogen peroxide 1% (10µl/disc)

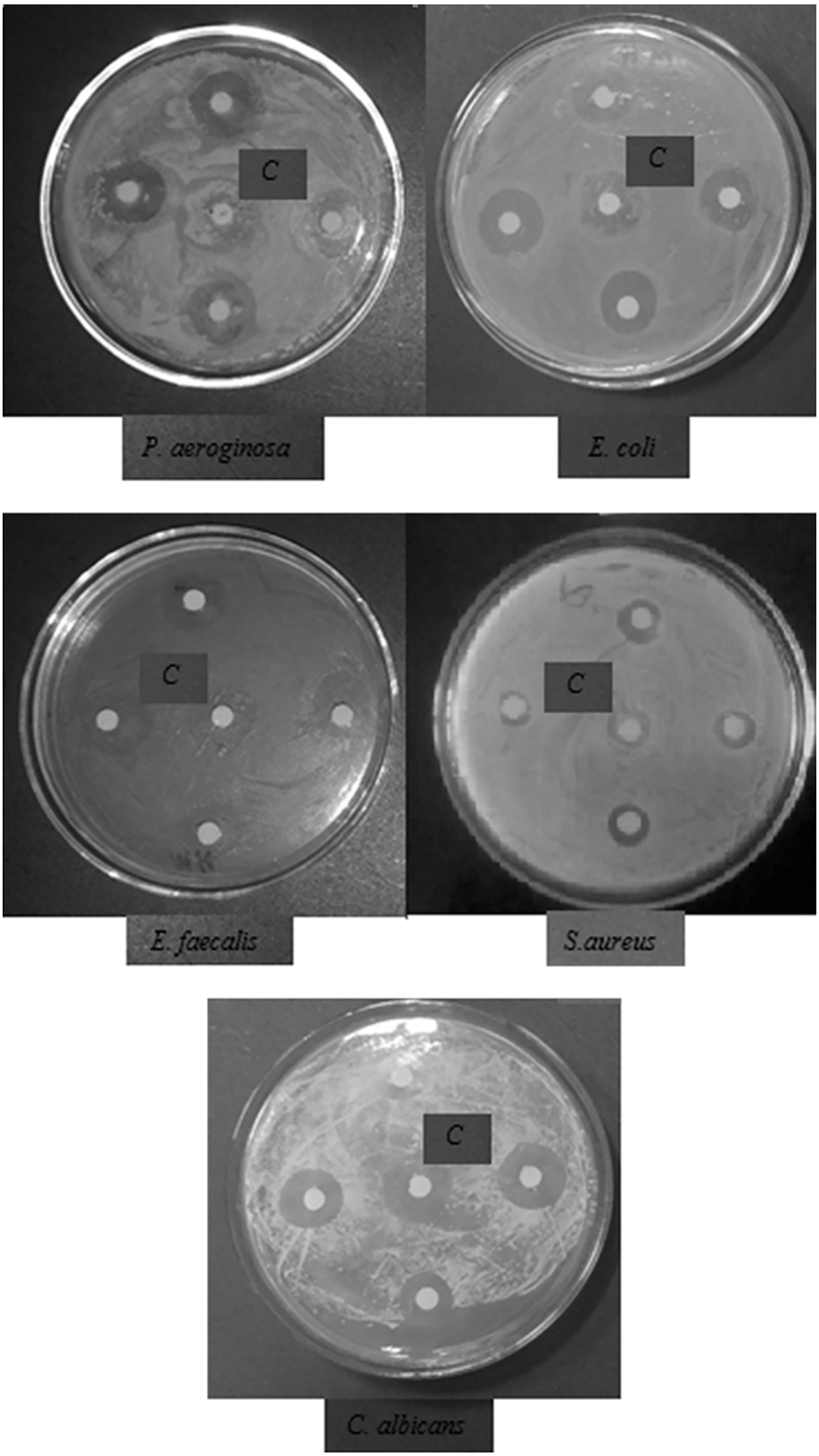

Figure 1. Zones of inhibition of ethanol extract (10 µl) which is obtained from A. polytricha. C; Control- ethanol without extract.

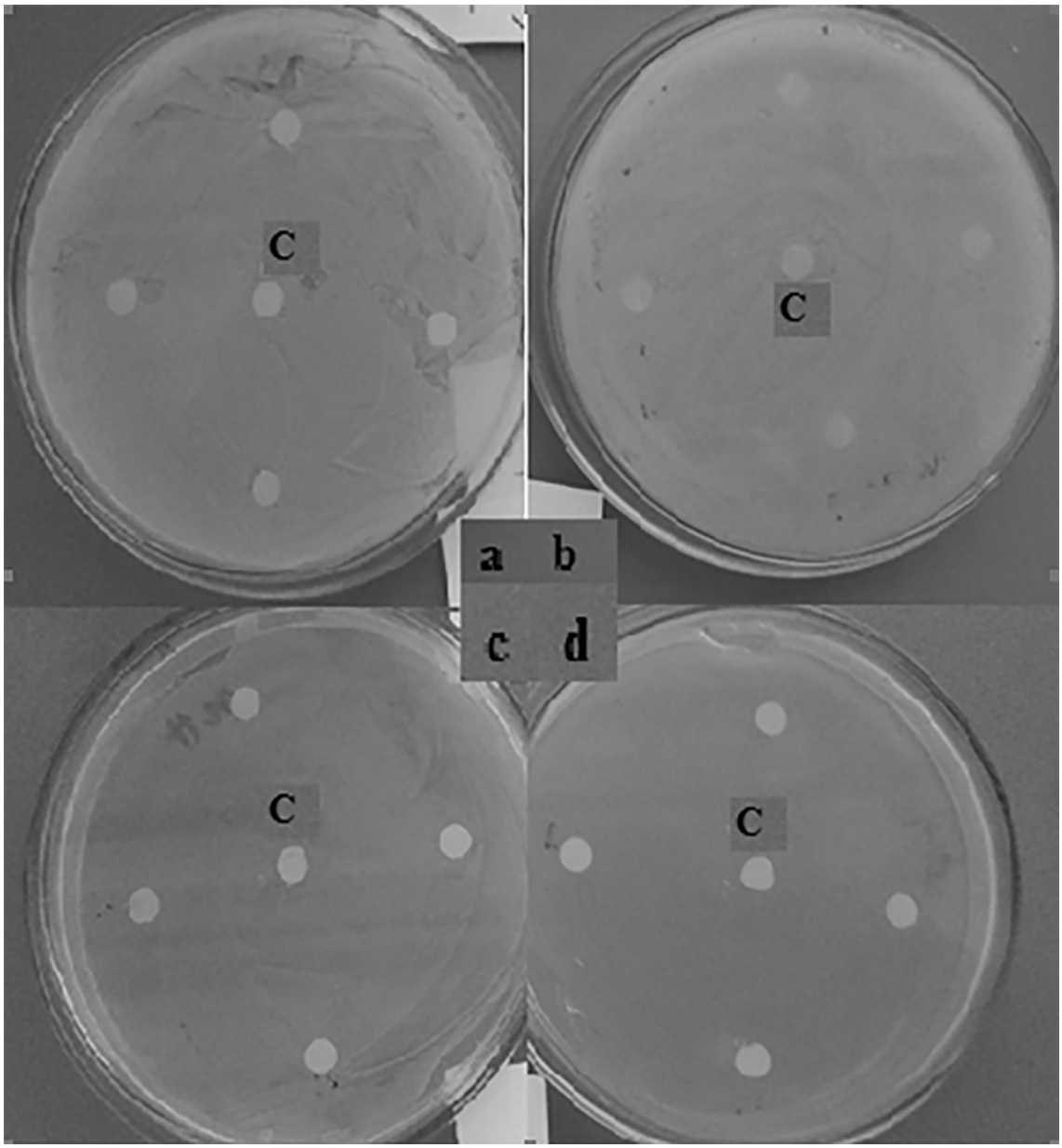

Figure 2. Zones of inhibition of water extract (10 µl) which is obtained from *A. polytricha*. a; *S. aureus* (ATCC-65389), b; *E. faecalis* (ATCC-29212), c; *P. aeroginosa* (ATCC-27853) and d; *E. coli* (ATCC-25922), C; Control- ethanol without extract.

REFERENCES

1. Stern KR, Bidlack JE, Jansky SH. Kingdom Fungi. In: Stern KR, ed. Introductory plant biology. 11th ed. 2008.
2. Hung PV, Nhi NNY. Nutritional composition and antioxidant capacity of several edible mushrooms grown in the Southern Vietnam. International Food Research Journal (2012) 19(2): 611–615.
3. Lowy B. A Morphological Basis for Classifying the Species of Auricularia. Mycologia (1951) 43: 351–358.
4. Yu M, Bo M, Luo X, Zheng L, Xu X. Molecular Diversity of Auricularia polytricha Revealed by Inter–Simple Sequence Repeat and Sequence–Related Amplified Polymorphism Markers. Current Microbiology (2008) 56:240-245.
5. Jonathan S.G. Vegetative growth requirements and antimicrobial activities of some higher fungi in Nigeria. Ph.D Thesis. University of Ibadan (2002).
6. Irawati D, Hayashi C, Takashima Y, Wedatama S, Ishiguri F, Lizuka K, Yoshizawa N, Yokota S. Cultivation of the edible mushroom Auricularia polytricha using saw dust based substrate made of three Indonesian commercial plantation species, Falcataria moluccana, Shorea sp., and Tectona grandis. Micologia Aplicada International (2012) 24 (2): 33–41.
7. Zoberi M.H. Tropical Macrofungi. Macmillan. Press London (1972) pp: 158.

8. Jonathan SG, Bawo DD, Adejoye DO, Briyai OF. Studies on Biomass Production in Auricularia polytricha Collected from Wilberforce Island, Bayelsa State, Nigeria. American Journal of Applied Science (2009) 6: 182–186.
9. Wu CM, Chen QH. Anticoagulation and antihyperlipidemia action of the polysaccharide from Auricularia polytricha. J China Pharm Univ (1991) 22:164-166.
10. Sheu F, Chien PJ, Chien AL. Isolation and characterization of an immunomodulatory protein (APP) from the Jew's Ear mushroom Auricularia polytricha. Food Chem (2004) 87:593-600.
11. Koyama K, Akiba M, Imaizumi T. Antinociceptive constituents of Auricularia polytricha. Planta Med (2002) 68:284-285.
12. Mau JL, Chao GR, Wu KT. Antioxidant properties of ethanolic extracts from several ear mushrooms. J Agric Food Chem (2001) 49:5461-5467.
13. Thohinung S, Kanokmedhakul S, Kanokmedhakul K, Kukongviriyapan V, Tusskorn O, Soytong K. Cytotoxic 10-(indol-3-yl)-[13]cytochalasans from the fungus Chaetomium elatum ChE01. Archives of Pharm Research (2010) 33: 1135-1141.
14. Jiang J, Sliva D. Novel medicinal mushroom blend suppresses growth and invasiveness of human breast cancer cells. International Journal of Oncology (2010) 37: 1529 – 1536.
15. Fortes RC, Novaes MRCG. Effects of dietary supplementation with Agaricales mushrooms and other fungi in medicinal therapy against cancer. Revista Brasileira de Cancerologia. (2006) 52: 363 – 371.
16. Barros L, Baptista P, Estevinho LM, Ferreira ICFR. Bioactive properties of the medicinal mushroom Leucopaxillus giganteus mycelium obtained in the presence of different nitrogen sources. Food Chemistry (2007) 105: 179 – 186.
17. Luo KW, Yu ZM, Co NN, Wu SH, Wu P, Fung KP, Kwok TT. Suillin from the mushroom Suillus placidus as potent apoptosis inducer in human hepatoma HepG2 cells. Chemico-Biological Interactions (2009) 181: 168 – 174.
18. Kim SH, Song YS, Kim SK, Kim BC, Lim CJ, Park EH. Anti-inactivities of the n – BuOH subfraction of mushroom Phellinuslinteus. Journal of Ethnopharmacology (2004) 93: 141 – 146.
19. Kupra J, Anke T, Oberwinkler G, Schramn G, Steglich W. Antibiotics from basidiomycetes VII. Crinipellis stripitaria (Fr.) Pat. Journal of Antibiotics (1979) 32: 130–135.
20. Brandt CR, Piriano F. Mushroom antivirals. Recent Research Developments for Antimicrobial Agents and Chemotherapy (2000) 4: 11–26.
21. Erel O. A novel automated method to measure total antioxidant response against potent free radical reactions. Clin Biochem (2004) 37:112–119.
22. Alves MJ, Ferreira I, Dias J, Teixeira V, Martins A, Pintado M. A Review on Antimicrobial Activity of Mushroom (Basidiomycetes) Extracts and Isolated Compounds. Planta Med (2012) 78: 1707-1718.
23. Parrilla AE, Aguilar GAG, de la Rosa la, Martínez NR, Aguilar G. Total phenols and antioxidant activity of commercial and wild mushrooms from Chihuahua, Mexico. Cienc Tecnol Aliment (2007) 5: 329–334.
24. Kosanić M, Ranković B, Dašić M. Mushrooms as possible antioxidant and antimicrobial agents. Iranian Journal of Pharmaceutical Research (2012) 11: 1095–1102.
25. Yıldırım NC, Turkoglu S,Yıldırım N, Ince OK. Antioxidant properties of wild edible mushroom Pleurotus Eryngıı collected from Tunceli. Journal of Nanomaterials and Biostructures (2012) 74: 647–1654.
26. Luo X, Yu M.Y, Jiang N, Xu XY, Zeng, J, Zheng LY. Effects of Auricularia polytricha polysaccharide on mouse macrophage cytokine and iNOS gene expression. Jun Wu Xi Tong (2009) 28: 435-439.
27. Mau JL, Chao GR, Wu KT. Antioxidant properties of methanolic extracts from several ear mushrooms. Journal of Agricultural and Food Chemistry (2001) 49: 5461-5467.
28. Yang BK, Ha JY, Jeong SC, Jeon YJ, Ra KS, Das S. Hypolipidemic effect of an exo–biopolymer produced from submerged mycelial culture of Auricularia polytricha in rats. Biotechnology Letters (2002) 24: 1319-1325.
29. Packialakshmi B, Sudha G, Charumathy. Bioactive constituents and antioxidant efficacy of Auricularia polytricha. Asian J Pharm Clin Res (2016) 91: 125–129.
30. Sun YX, Liu JC, Kennedy JF. Purification, composition analysis and antioxidant activity of different polysaccharide conjugates (APPs) from the fruiting bodies of Auricularia polytricha. Carbohydrate Polymers (2010) 82: 299-304.
31. Park KM, Kwon KM, Lee SH. Evaluation of the antioxidant activities and tyrosinase inhibitory property from mycelium culture extracts. Evidence–Based Complementary and Alternative Medicine (2015) 19:111–118.
32. Wong FC, Chai TT, Tan SL, Yong AL. Evaluation of bioactivities and phenolic content of selected edible mushrooms in Malaysia. Trop J Pharm Res (2013) 12 (6): 1011–1016.
33. Gbolagade SJ, Fasidi IO. Antimicrobial activities of some selected Nigerian mushrooms. African Journal of Biomedical Research (2005) 8; 83– 87.

NATIONAL & INTERNATIONAL SCIENTIFIC EVENTS

2017 International Conference on Sustainable Energy Engineering (ICSEE 2017)

Venue: The University of Western Australia
Location: Perth, Australia

BEGINS: Jun 12, 2017
Ends: Jun 14, 2017

Ecology and Safety 2017, 26th International Conference

Venue: Hotel Royal Castle
Location: Elenite, Burgas, Bulgaria

BEGINS: Jun 23, 2017
Ends: Jun 27, 2017

2017 2nd International Conference on Nanotechnology and Nanomaterials in Energy (ICNNE2017) - Ei Compendex, Scopus

Venue: INSA Lyon, France
Location: Lyon, France

BEGINS: July 07, 2017
Ends: July 09, 2017

2017 International Conference on Pure and Applied Mathematics (ICPAM2017)

Venue: TBA
Location: Prague, Czech Republic

BEGINS: July 22, 2017
Ends: July 25, 2017

ACM--2017 the First International Conference on Biometrics Science and Engineering (ICBSE 2017)--Ei Compendex, ISI and Scopus

Venue: Nanyang Executive Centre
Location: Singapore

BEGINS: Aug 04, 2017
Ends: Aug 06, 2017

2017 The 2nd International Conference on Advanced Functional Materials (ICAFM 2017)

Venue: TBA
Location: Los Angeles, United States of America

BEGINS: Aug 04, 2017
Ends: Aug 06, 2017

2017 International Conference on Robotics and Automation Sciences (ICRAS 2017)--IEEE, Ei Compendex and Scopus

Venue: TBA
Location: Hong Kong, China

BEGINS: Aug 26, 2017
Ends: Aug 29, 2017

22nd International Conference on Researches in Science & Technology (ICRST)

Venue: I. College London, S. Kensington Campus
Location: London, UK

BEGINS: Sept 13, 2017
Ends: Sept 14, 2017

8th International Conference on Legume Genetics and Genomics (ICLGG)

Venue: Hotel Azúr
Location: Siófok, Lake Balaton, Hungary

BEGINS: Sept 18, 2017
Ends: Sept 22, 2017

AVTECH '17 / V. International Automotive and Vehicle Technologies Conference

Venue: Nippon Hotel, Taksim
Location: İstanbul, Turkey

BEGINS: Oct 06, 2017
Ends: Oct 07, 2017

CHEMTECH '17 / V. International Chemical Engineering and Technologies Conference

Venue: Nippon Hotel, Taksim
Location: İstanbul, Turkey

BEGINS: Oct 06, 2017
Ends: Oct 07, 2017

2017 the 7th International Conference on Power and Energy Systems (ICPES 2017)

Venue: TBA
Location: Toronto, Canada

BEGINS: Nov 01, 2017
Ends: Nov 03, 2017

Abstracted & Indexed in:

TR Dizin Mühendislik ve Temel Bilimler Veri Tabanı | CrossRef | Google Scholar | MIP Database | StuartxChange | ResearchBib | Scientific Indexing Services (SIS)

HITTITE